Upconversion of infrared to visible light in rare-earths doped phosphate phosphors for photodynamic therapy application

By

Puseletso Pricilla Mokoena
(MSc)

A thesis submitted in fulfillment of the requirements for the degree

PHILOSOPHIAE DOCTOR

in the

Faculty of Natural and Agricultural Sciences

Department of Physics

at the

University of the Free State

South Africa

Promoter: Prof. O.M. Ntwaeaborwa

Co-Promoter: Prof. H.C. Swart

June 2017

Declaration by candidate

(i) "I, **Mokoena Puseletso Pricilla**, declare that the Doctoral Degree research thesis that I herewith submit for the Doctoral Degree qualification at the University of the Free State is my independent work, and that I have not previously submitted it for a qualification at another institution of higher education."

(ii) "I, **Mokoena Puseletso Pricilla**, hereby declare that I am aware that the copyright is vested in the University of the Free State."

(iii) "I, **Mokoena Puseletso Pricilla**, hereby declare that all royalties as regards intellectual property that was developed during the course of and/or in connection with the study at the University of the Free State, will accrue to the University."

Signature:…… Date.....

ACKNOWLEDGEMENTS

- Δ Firstly, I would like to thank God for granting me the opportunity to pursue this research even in difficult times. To have given me knowledge, power, and wisdom to conduct the research till the end.
- Δ My Supervisor: *Prof. O.M. Ntwaeaborwa*, Thank you very much for the role you played throughout this study. Thank you for your patience, for believing in me, and always encouraging me. Thank you a lot.
- Δ I would like to express my heartfelt gratitude to my co-supervisor *Prof. H.C. Swart*, for the support and valuable inputs towards this study, in the meeting and as well as in the paper write-ups. I am grateful.
- Δ Many thanks to *Distinguished Prof T. Nyokong* and her students *Dr. David Oluwole*, *Mr Gauta Au* and *S22* at Rhodes University, for their warm welcome in their lab and introducing me to PDT activity.
- Δ I would like to thank technical staff at the Centre For Microscopy (*Prof. P.W.J. Van Wyk* and *Ms H. Grobler*) for allowing me to use JEOL-JSM7800 Field Emission Scanning Electron Microscope during my studies.
- Δ My deepest appreciation to a group of fellow post graduate students and the entire staff in Physics Department for a good social environment and fruitful academic discussions.
- Δ Special thanks from South African National Research Foundation (NRF) for funding.
- Δ To all my friends: Thank you very much for your valuable support and your words of encouragement in difficulties and a special thanks to *Mr. L.E. Nkoe* for the outmost support, encouragement and understanding all the times, you are the best.
- Δ My loving Family: My father (*Mohloki Samuel Mokoena*), my mother (*Mohanuoa Maria Mokoena*), my younger brother (*Muso Joshua Mokoena*) and the love of heart, the light of my life (*Nyakallo Mokoena*). You have shown me a true definition of unconditional love, you stood by me through thick and thin, you have never lost hope on me, and you kept on believing in me. Your prayers, support and patience made me the person I am today. Thank you for walking this journey with me, I could not have made it without your presence. To the entire family, thank you all.

The thesis is dedicated to my family, thank you for the unconditional love and support throughout my studies.

"Love is a condition in which the happiness of another person is essential to your own".

-Robert Heinlein

Abstract

Phosphate phosphors have emerged as an important family of luminescent material due to their low sintering temperature, broad band gaps, high thermal and chemical stability, and moderate phonon energies. Their structure can provide a wide range of possible cationic substitutions since there are different inequivalent sites of metal ions presenting a large-scale of size and coordination spheres. Rare earth ions doped phosphate compounds as luminescence materials have been widely investigated in different host lattices including phosphates. In this study, the luminescent properties of different phosphate phosphors doped with Er^{3+}, Eu^{3+}, and Yb^{3+} were investigated.

Er^{3+} and Yb^{3+} singly doped, and Er^{3+}/Yb^{3+} co-doped $Ba_5(PO_4)_3OH$ phosphor powders were successfully synthesized by the urea combustion method. The X-ray Diffraction (XRD) patterns exhibited hexagonal structure for $Ba_5(PO_4)_3OH$ referenced in the ICDD (International Center for Diffraction Data) Card Number 00-024-0028. There were no peak shifts nor secondary peaks observed suggesting that pure phases were crystallized. The Scanning Electron Microscope (SEM) image showed that the particles were agglomerated together forming ellipsoidal shapes. The Energy Dispersive x-ray Spectroscopy (EDS) spectra with intense peaks of Ba, P, and O were observed confirming the formation of $Ba_5(PO_4)_3OH$. The particle size distribution of the $Ba_5(PO_4)_3OH$ powder was estimated from a statistical analysis by measuring approximately 10 particles. The average particles length and width were 867 and 169 nm, respectively. Upon excitation using a 980 nm laser, multiple emission peaks in the green region and red region were observed corresponding to the transition of the Er^{3+} ion. By further co-doping with Yb^{3+} the red emission was enhanced due to energy transfer from Yb^{3+} to Er^{3+}.

$Ba_5(PO_4)_3OH$ co-doped with Eu^{3+} and Yb^{3+} phosphors were prepared by the urea combustion method. The diffraction peaks of $Ba_5(PO_4)_3OH$ were indexed to the pure hexagonal phase, referenced in ICDD Card Number 00-024-0028. The SEM images showed a change (ranging from rods, spherical, needle-like to non-uniform particles) in surface morphology which was due to annealing and addition of dopants. The size of the particles appeared to be larger/bigger when comparing as-prepared and annealed phosphor powders. This could be due to the annealing-induced expansion. The broad intense excitation peak at 240 nm and other excitation peaks located at ~319, 360, 382, 395 and 465-537 nm were assigned to

transitions of Eu^{3+} ion. The emission peaks were observed at ~589, 614, 651 and 699 nm. Upon co-doping with Yb^{3+}, the strong emission peak was observed at 657 nm assigned to the Eu^{3+} transitions. This was due to the cooperative energy transfer process.

Er^{3+} and Yb^{3+} co-doped $Ca_5(PO_4)_3OH$ samples were synthesized by urea the combustion method. The XRD patterns of $Ca_5(PO_4)_3OH$ powders for both as-prepared and those annealed at 800 ^{0}C were attributed to the hexagonal phase of $Ca_5(PO_4)_3OH$ referenced in ICDD Card No. 00-073-0293. The SEM micrographs exhibited rod or plate-like morphology forming flowers, plate-like structures and small agglomerated particles on top of the plates. For Er^{3+} singly doped phosphors emission peaks were observed in the green region ranging from 517 -573 nm and red region in the range of 653- 679 nm. $Ca_5(PO_4)_3OH:Er^{3+}$ phosphors were prepared using different concentrations of Er^{3+} ranging from 1-7 mol.%. The photoluminescence intensity increased with increasing concentrations from 1 to 3 mol%, and decreased at high concentrations of 5 and 7 mol.% due to concentration quenching effects. Adding different concentrations (5-15 mol.%) of Yb^{3+}. The emission intensities on both the green and red region increased with increasing concentrations of Yb^{3+} ions. The enhancement of green emission can be due to increasing of the three-photon energy transfer process probability between the Yb^{3+} and Er^{3+} ions.

$Ca_5(PO_4)_3OH:Eu^{3+}$, Yb^{3+} phosphor powders were synthesized by the combustion method using urea as a fuel. The XRD patterns of $Ca_5(PO_4)_3OH$ powders for both as-prepared and those annealed at 800 ^{0}C were assigned to the hexagonal phase of $Ca_5(PO_4)_3OH$ referenced in ICDD Card No. 00-073-0293. The crystal sizes calculated for as-prepared and annealed powders were found to be 27 and 44 nm, respectively. UC emission spectrum of $Ca_5(PO_4)_3OH:Eu^{3+},Yb^{3+}$ phosphor powder was observed under 980 nm excitation. Prominent red emission from Eu^{3+} ion was clearly observed at 613 nm together with minor emission peaks at 547, 591, 654 and 697 nm. The prominent red emission from Eu^{3+} was due to energy transfer from Yb^{3+} ion. A cooperative energy transfer from Yb^{3+} ion pair to a single Eu^{3+} ion occurred by fast non-radiative relaxation to the metastable $^5D_0$ state, and the red Eu^{3+} emission was observed.

$Sr_5(PO_4)_3OH$ co-doped Er^{3+}/Yb^{3+} phosphor powders were synthesized by combustion method. The XRD pattern diffraction peaks were consistent with the standard data referenced in ICDD Card No. 00-033-1348. The average crystallite size calculated was 43 ± 2 nm. The SEM micrographs showed that the powder was composed of agglomerated

particles with edges forming hexagonal shapes. The agglomeration showed a porous structure resulting from the nature of the combustion reaction associated with the evolution of large volume of gases. Upon 980 nm excitation, $Sr_5(PO_4)_3OH:Er^{3+}$ exhibited multiple emission bands in the green region and a less intense peak in the red region. The strong red emission peak with two minor splits were observed at 661 nm, and (651 and 679 nm), by co-doping with Yb^{3+} ion.

$Sr_5(PO_4)_3OH$ co-doped Eu^{3+}/Yb^{3+} phosphor powders were synthesized by the combustion method. All the diffraction patterns matched with the standard data referenced by ICDD Card No. 00-033-1348. The SEM image showed that the powder composed of a network of particles with irregular shapes and small bright particles encrusted on the surface of the bigger particles. The particles containing heavy atoms in backscattered electron detector were stronger than light particles and they appear brighter. UC emission spectrum of $Sr_5(PO_4)_3OH:Eu^{3+},Yb^{3+}$ phosphor powder was observed under 980 nm excitation. Prominent red emission from Eu^{3+} ion was clearly observed at 658 nm due to cooperative energy transfer process.

Photodynamic therapy uses special drugs, called photosensitizers, along with light to kill cancer cells. The drugs only works after been activated by certain kinds of light. Most drugs are activated by red light. The enhanced red luminescence from the above mentioned phosphors suitable to activate different photosensitizers for treatment of cancer or photodynamic therapy. Photodynamic therapy activity was performed using red emitting phosphors prepared in this study together with phthalocyanine as a photosensitizer. Phthalocyanine is activated by the wavelength ~670 nm. The activity results are discussed in chapter 10.

Keywords

Phosphates powders, Rare earth ions, Upconversion luminescence, Energy transfer, Photodynamic therapy.

List of Acronyms

XRD	X-ray Diffraction
ICDD	International Center for Diffraction Data
ICSD	Inorganic Crystal Structure Database
FTIR	Fourier Transform Infrared
FESEM	Field Emission Scanning Electron Microscope
EDS	Energy Dispersive x-ray Spectroscopy
UV-Vis	Ultra Violet-Visible
NIR	Near Infrared
RE	Rare Earth
PL	Photoluminescence
UCL	Upconversion Luminescence
ETU	Energy Transfer Upconversion
CET	Cooperative Energy Transfer
GSA	Ground State Absorption
PDT	Photodynamic Therapy
PS	Photosensitizers
MCF	Human breast adenocarcinoma
DMEM	Dulbecco's modified Eagle's medium

Table of Contents

List of Tables

List of Figures

Chapter 1

Introduction

1.1 Overview

1.1.1 Phosphate Phosphors

Phosphate materials have a wide range of applications and they have been extensively studied. They have been used in various applications such as ceramic materials, catalysts, adsorbent, fluorescent materials, biomaterial, food additives, pigments and detergents [1-3]. Most of phosphate materials are biocompatible, meaning that they form bonds with human tissues. With their high biocompatibility and good surface properties, synthetic phosphate materials have promising potential in biomedicine [4]. They can be prepared by different methods such as co-precipitation, hydrothermal, sol-gel and combustion [5-6]. The preparation methods play an important factor in controlling the particle shape and size of the materials. There are several treatments that can be used to control the particle shape and size namely, ultrasonic treatment, regulating pH, controlling the pre- and post-annealing treatment. Inorganic phosphates based compounds with the general formula $M_5(PO_4)_3X$ (M = Ca, Sr, Ba and X = Cl, F, OH) are now considered as excellent host for preparation of phosphors materials due to high chemical and thermal stability. $M_5(PO_4)_3X$ have two cationic structure sites (M1 and M2) which are 6-fold coordinated 4f sites and 7-fold coordinated 4h sites, respectively [7]. These sites can accommodate a great variety of foreign cations such as transition metal and rare earth ions with different ionic radii [8]. Addition of rare earth elements to these phosphates gives higher luminescent properties to the material. This in turn, makes them the good phosphors for applications in different light emitting devices and radiation oncology (the use of radiation therapy to treat cancer). This study was focused on the preparation of different inorganic phosphate phosphors for applications in photodynamic therapy.

1.1.2 Photodynamic Therapy

Photodynamic therapy (PDT) is the medical treatment that utilizes visible light of specific wavelength to activate the photosensitizer (PS) in the presence of oxygen. The treatment involves the uptake of photosensitizer by cancer tissues followed by photoirradiation. The light source should therefore be based on photosensitizer absorption, disease, cost and size [9]. The upconverting nanophosphors are used as light source absorbing the long wavelengths to produce visible light that excites the photosensitizer. The selection of good upconverting nanophosphors to be used depends on the type of photosensitizer used. Mostly used nanophosphors absorb infrared light at the range from 700 – 1100 nm, and exhibit strong visible peaks in the range of 500 – 650 nm [10-11]. Wavelengths higher than 850 - 900 nm do not have sufficient energy to excite the photosensitizer and to produce reactive oxygen species essential for cancer treatment. The combined action of the phosphor and photosensitizer results in the formation of singlet oxygen ($^1O_2$), the phosphor will adsorb infrared light and emit in the visible light which further excites the photosensitizer molecules. The absorbed energy by PS molecules will interact with ground-state oxygen molecules generating $^1O_2$. Reactive oxygen species causes oxidative damage to biological substrates and ultimately cell death. Figure 1 shows the procedure during photodynamic therapy.

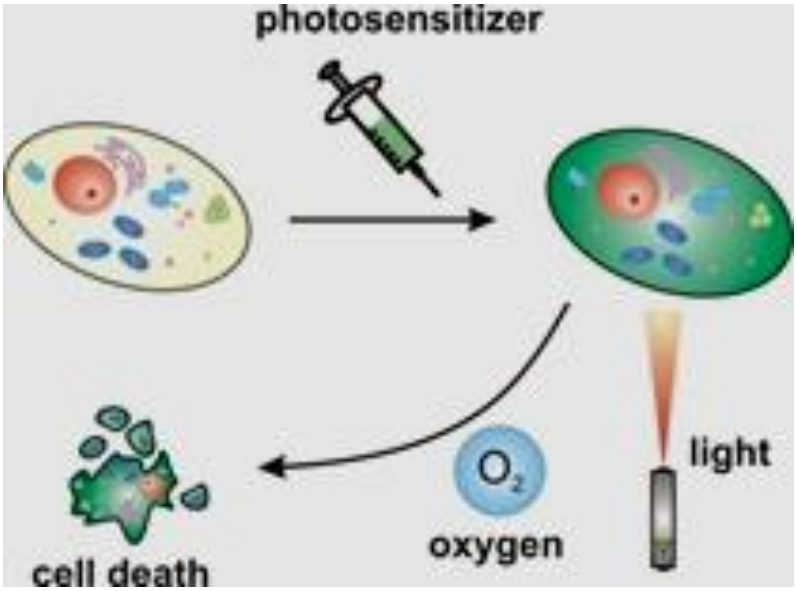

Figure 1. 1 Photodynamic treatment [12].

1.2 Problem statement

Million people die every year from different types of cancer such as head and neck, gastrointestinal and lung cancer. Frequently used therapies for treatment of these cancers include surgery, radiotherapy and chemotherapy. PDT has gained acceptance as a new technique for treatment of different cancers [10]. The drawbacks of this treatment are that (i) it makes the skin and eyes sensitive to light for about 6 weeks after the treatment, thus these effects can be treated by avoiding direct sunlight and bright indoor light for at least 6 weeks, (ii) the light needed to activate most photosensitizes cannot pass through more than 1 cm of a tissue. PDT is used to treat just tumors on or just under the skin. It is also less effective in treating large tumors, because the light cannot pass far into these tumors. The limited tissue penetration of light prohibits the destruction of cancer cells. This study is focused on development of light that can penetrate and treat deep or large tumors by improving the luminescent properties of phosphor powders used as light sources in the treatment.

1.3 Aim

The aim of this study is to investigate the upconversion luminescence of various phosphate phosphors for possible application in photodynamic therapy.

1.4 Objectives

- To prepare and investigate the photoluminescent properties of various phosphates ($M_5(PO_4)_3X$, M = Ca, Sr, Ba and X = OH) phosphors doped with various lanthanides such as erbium (Er^{3+}), and europium (Eu^{3+}) using urea combustion method by varying the concentrations of Eu^{3+} and Er^{3+} ions.
- To enhance the red luminescence of the phosphors by co-doping with different concentrations of ytterbium (Yb^{3+}) ion.
- To study the energy transfer from Yb^{3+} to Er^{3+} and Eu^{3+} in various phosphate phosphors.
- To perform the photodynamic therapy activity in the cancerous cells using the phosphate phosphors prepared in this study.

1.5 Thesis Layout

This thesis is divided into the following 11 chapters

Chapter 1: Provides a general introduction on phosphate phosphors and photodynamic therapy, problem statement and aims of the study.

Chapter 2: Provides theoretical background on different metals (Ba^{2+}, Ca^{2+} and Sr^{2+}) and phosphate materials, rare earths, upconversion luminescence process, energy transfer in rare earths activated phosphors, and applications in photodynamic therapy.

Chapter 3: This chapter provide a brief description of the synthesis method and characterization techniques used in this study.

Chapter 4: This chapter discusses the enhanced upconversion emission of Er^{3+}/Yb^{3+} co-doped barium hydroxide phosphate phosphors.

Chapter 5: Upconversion luminescence properties of Eu^{3+}/Yb^{3+} co-doped $Ba_5(PO_4)_3OH$ phosphor powders are discussed in this chapter.

Chapter 6: This chapter discusses the energy transfer in Er^{3+}:Yb^{3+} co-doped calcium phosphate phosphor powders.

Chapter 7: This chapter discusses the cooperative upconversion luminescence in Eu^{3+}/Yb^{3+} co-doped $Ca_5(PO_4)_3OH$ phosphor powders.

Chapter 8: This chapter discusses the upconversion luminescence of Er^{3+}/Yb^{3+} doped $Sr_5(PO_4)_3OH$ phosphor powders.

Chapter 9: This chapter discusses the synthesis and upconversion properties of Eu^{3+}/Yb^{3+} co-doped $Sr_5(PO_4)_3OH$ nanoparticles and their applications in photodynamic therapy.

Chapter 10: This chapter discusses the evaluation of photodynamic therapy activity of phosphate based upconversion nanoparticles against human breast adenocarcinoma cells.

Chapter 11: Summary and future work.

References

[1] H. Onoda, S. Fujikado, Journal of Material Science and Chemical Engineering, 2014, 2, 27-34

[2] H. Onoda, H Nariai, A. Moriwaki, H. Maki, I. Motooka, Journal of Material Chemistry, 2002, 12, 1754-1760

[3] H. Onoda, T. Yamaguchi, Materials Sciences and Applications, 2014, 3, 18-23

[4] F. Chen, Y. Zhu, J. Wu, P. Huang, D. Cui, Nano Biomedicine and Engineering, 2012, 4, 41-49

[5] I.M. Nagpure, K.N. Shinde, V. Kumar, O.M. Ntwaeaborwa, S.J. Dhoble, H.C. Swart, Journal of Alloys and Compounds, 2010, 492, 384-388

[6] K.N. Shinde, S.J. Dhoble, Advanced Materials Letters, 2010, 1, 254-258

[7] X. Chen, P. Dai, P. Zhang, C. Li, S. Lu, X. Wang, Y. Jia, Y. Liu, Inorganic Chemistry, 2014, 53, 3441-3448

[8] U. Kempe, J. Gotze, Mineralogical Magazine, 2002, 66, 151-172

[9] S. Rahul, A. Jahardhan, D.M. Parvathi, J. Bhuvan, Journal of Indian Academy of Oral Medicine and Radiology, 2013, 25, 31-37

[10] P. Zhang, W. Steelant, M. Kumar, M. Scholfield, Journal of the American Chemical Society, 2007, 129, 4526-4527

[11] D.C. Kumar, L.F. Shan, Y. Zhang, Advanced Drug Delivery Reviews, 2008, 60, 1627-1637

[12]http://portal.faf.cuni.cz/Groups/Azaphthalocyanine-group/Research-Projects/Photodynamic-therapy/

Chapter 2

Theoretical Background

2.1 Phosphate materials

Phosphate materials have attracted the attention of various phosphate groups worldwide due to their excellent properties such as excellent thermal stability, fine-grained, insoluble, contain metastable phases, biocompability, non-inflammatory and have low environmental toxicity [1, 2]. They are widely used as ceramic materials, catalysts, adsorbent, fluorescent materials, biomaterials, food additives, pigment and detergent. Most phosphates are biocompatible, they can therefore easily form bonds with living tissues. Phosphates have emerged as excellent hosts for rare earth ions to prepare light emitting materials (phosphors) [3]. Rare earth activated alkaline phosphate based compounds are of interest due to their unusual stability and useful luminescent properties. They have been investigated because of varied optical energy level structures of the rare earth elements which result in light emission from ultraviolet to far-infrared regions [4]. They have a large bandgap and PO_4^{3-} highly absorbing in the VUV region, they have moderate phonon energy, and exceptional damage threshold [5]. They can be synthesized using low-cost and time-saving synthesis methods at relatively low synthesis temperature. They can be synthesized using wet chemical and combustion methods. They are used in different applications such fluorescent lamps, color TV screen, long afterglow devices, solid state lasers, scintillators, and pigments. Despite the wide range of applications, the use of alkaline phosphates, such as barium (Ba^{2+}), calcium (Ca^{2+}) and strontium (Sr^{2+}) has not been receiving attention in organic compounds. These alkaline ions play an important role in enhancing the luminescence efficiency of phosphors by modification of composition and charge compensation in many phosphors, they introduce an oxygen vacancy in the lattice as charge compensating defects and also increases the ionic conductivity [6]. The ionic radii of six coordinates of Ba^{2+}, Ca^{2+}, and Sr^{2+} are 1.35, 1.00 and 1.18 Å, respectively [7]. Therefore, these alkaline are expected to be better substitutes for rare earth ions to prepare luminescent materials for various applications.

2.2 Rare-earth Elements

Rare earth elements are a set of seventeen chemical elements in the periodic table with the atomic number in the range of 57-71. Specifically they are the fifteen lanthanides, as well as scandium and yttrium. Scandium and yttrium are considered rare earth elements because they tend to occur in the same ore deposits as the lanthanides and exhibit similar chemical behaviour [8]. Rare earth elements are categorized into two groups namely; light rare earth elements (LREE) and heavy rare earth elements (HREE). Light rare earth elements which are also known as the cerium group are Sc, La, Ce, Pr, Nd, Pm, Sm, Eu, and Gd [9, 10]. Heavy rare earth elements are Y, Tb, Dy, Ho, Er, Tm, Yb and Lu, and they are known as yttrium group [11]. The definition of LREE and HREE is based on the electron configuration of each rare-earth element. Rare earth ions are well known for their *4f* shell level that resides deep inside the atom. Each rare earth ion contains a *4f* orbital shielded by *4d* and *5p* orbital electrons. Figure 2.1 shows the LREE and HREE rare earth elements. Rare earth elements are used as catalysts, polishing compounds and also as luminescent centres in phosphors. Rare-earths doped phosphors are used in many devices such as dyes, cell phones, and fluorescent lamps, lasers.

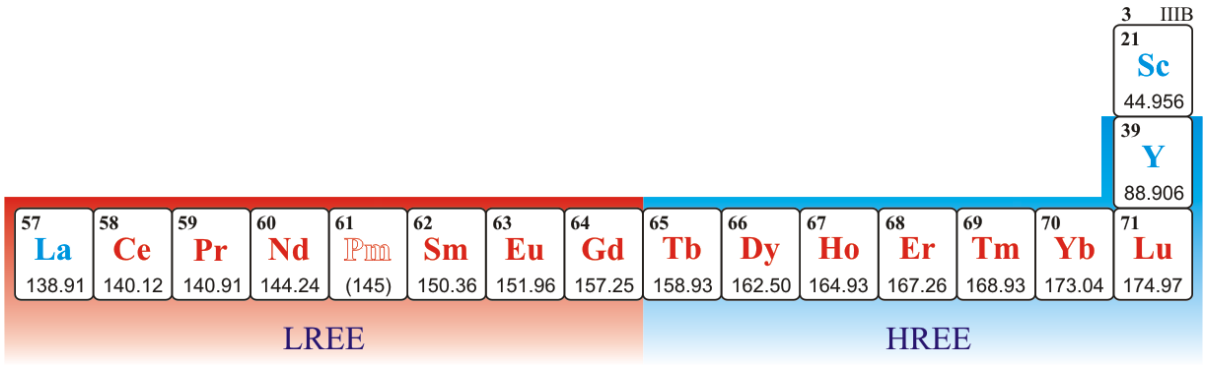

Figure 2. 1 Rare-earth elements divides into LREE and HREE [12].

2.2.1 Erbium, Europium and Ytterbium

Rare earth ions such as erbium can be used in medical applications (i.e. dermatology and dentistry) for laser surgery in shallow tissue deposition and enamel ablation using dental laser. It is also used in treatment of skin diseases, to remove wrinkles and acne scars [13]. Erbium is a chemical element in the lanthanide series, with a symbol Er and atomic number 68. It is a silver-white solid metal when artificially isolated, natural erbium is always found in chemical combination with other elements on Earth. Erbium's principal uses involve its pink-colored Er^{3+} ions, and it does not react with oxygen as quickly as other lanthanides. Erbium is slightly toxic when ingested but the erbium compounds are not toxic [14]. Co-

doping of optical fiber with Er and Yb is used in high-power Er/Yb fiber lasers. Er^{3+} ions can be easily pumped by 808 and 980 nm commercial laser diode and upconvert the absorbed energy in the infrared region by giving luminescence in the visible region.

Europium is a chemical element with symbol Eu and atomic number 63. It is moderately hard, silver metal which readily oxidizes in air and water. It has an oxidation state of +3, but the oxidation state of +2 is also common. It is relatively non-toxic and it has no significant role in biology compared to other heavy atoms. It is used as a dopant in some types of glasses in lasers and other electronic devices. It exhibits an intense red luminescence upon irradiation with ultraviolet (UV) radiation. Eu^{3+} has 60 electrons: 54 electrons are in the closed shells as the xenon atom and 6 electrons in the 4f shell. The 4f shell is well shielded from its environment by the closed $5s^2$ and $5p^6$ outer shells [15]. It is widely used as a red phosphor in TV screens and fluorescent lamps; it can also be used as an excellent probe for biomedical applications [16]. Its fluorescence is usually used to interrogate biomolecular interactions in drug-discovery screens.

Ytterbium is a chemical element with symbol Yb and atomic number 70. Its most common oxidation state is +3, in oxides, halides and other compounds [17]. It has few uses; it is alloyed with stainless steel to improve some of its mechanical properties, to make certain lasers and is also used as a doping agent. It has attracted more attention as a dopant in laser materials. It has a $4f^{13}$ shell that lacks one electron compared to the fitted shell and has only two manifolds, namely the ground state ($^4f_{7/2}$) and excited state ($^2F_{5/2}$) which are separated by about 10 000 cm^{-1} that can form a quasi-three-level system due to Stark splitting [18-19]. The two manifolds of the Yb^{3+} have few advantages such as weak concentration quenching effect, no excited state absorption, and no up-conversion losses [20]. Yb^{3+} doping has been extensively studied in many matrices. Due to its high cross-section, it has been used as a sensitizer or other rare earth ions via energy transfer process. Table 2.1 shows the basic properties of Er, Eu and Yb elements.

Table 2.1 Basic properties of Er, Eu, and Yb [21-23].

Property	Rare earth elements		
	Erbium	Europium	Ytterbium
Atomic number	68	63	70
Atomic weight (g/mol)	167.26	151.96	173.04
Melting point (^{o}C)	1529	826	824
Boiling point (^{o}C)	2868	1489	1196
Oxidation state	+3	+3	+3/+2
Electron configuration	[Xe]$4f^{12}6s^{2}$	[Xe]$4f^{7}6s^{2}$	[Xe]$4f^{14}6s^{2}$
Ionic radius (Å)	1.14	1.01	1.12

2.3 Upconversion luminescence

Upconversion (UC) is a process in which the sequential absorption of two or more photons leads to the emission of light at shorter wavelength than the excitation wavelength via multiphonon process or energy transfers, which has emerged as an attractive platform for the construction of upconversion luminescence (UCL) imaging probes [24]. This fundamental process has many applications in biomedical imaging, light source and display technology, and solar energy harvesting. Lanthanide UC shows advantages of deeper tissue penetration. UC mechanisms are generally divided into four broad categories according to recent advances: excited state absorption (ESA), energy transfer UC (ETU), photon avalanche (PA), cooperative sensitization upconversion (CSU) and a recently proposed energy migration-mediated UC (EMU) [25]. These processes can be observed in materials with very different sizes and structures, including optical fibers, bulk crystals or nanoparticles. The most efficient upconversion process is ESA and ETU. ESA shown in figure 2.2 (a) plays an important role when the doping concentration is relatively low, that is energy transfer between activators is negligible, which lead to insufficient absorption and low UC efficiency. In ETU in figure 2.2 (b), two adjacent rare earth ions are involved. First step, there is a ground state absorption (GSA) induced by resonant photon excitation, which populates the E1 excited state of an activator ion. Second step, another absorbed pump photon excites a sensitizer ion. Third step, energy is sequentially transferred from the excited state of a sensitizer ion to the excited state of an activator ion in a non-radiative, resonant way. Lastly, the activator ion relaxes back radiatively from its excited state to its ground state and upconversion luminescence is observed. PA only occurs after a critical level of pump

density. If the pump density is sufficiently high, the intermediate reservoir level of many ions becomes populated initially by a non-resonant ground state absorption process, followed by resonant ESA or ETU from another excited ion to populate the UC emitting level. Efficient cross relaxation takes place between the excited and ground state ions, population of the reservoir level and the UC emitting level increases and causes an avalanche effect of generating more excited ion. The PA process is shown by figure 2.2 (c). There are reports assigning the mechanism as cooperative sensitization shown by figure 2.2 (d). Cooperative sensitization is similar to ETU, two different ions are involved in the excitation process, and it is closer to ESA because emission is from only one ion. In cooperative sensitization two ions from sensitizer cooperatively sensitize one activator to be excited in higher energy state than the excitation photon. Lastly, the upconversion process is cooperative luminescence. Cooperative luminescence is an emission process in which two interacting ions in the excited state emit a photon of twice the energy simultaneously. This upconversion emission is mostly observed from Yb^{3+} system. And this process is weaker than ETU and it involves only one type of ions and from ESA because it involves multiple ions [26]. EMU involves the four types of luminescent centres, namely sensitizers, accumulator, migrators and activator. The sensitizers or accumulator and the activator are in separate layers of the core-shell and connected by migrators. The sensitizer is first excited by ground state absorption and transfers its energy to an accumulator, promoting it to higher excited state. The accumulator possesses energy levels with longer lifetimes to accept the energy from the sensitizer. Energy migration takes place from higher excited state of accumulator to migrator followed by migration of the excitation energy through the migrators via core shell interface [27]. The migrated energy is trapped by an activator in the shell and emits UC luminescence as shown in figure 2.2 (e). Usually, efficient UC is restricted to erbium (Er^{3+}), holmium (Ho^{3+}) and thulium (Tm^{3+}) activators together with the luminescence sensitizer ytterbium (Yb^{3+}) [28]. Figure 2.2 depicts the basics of UC processes.

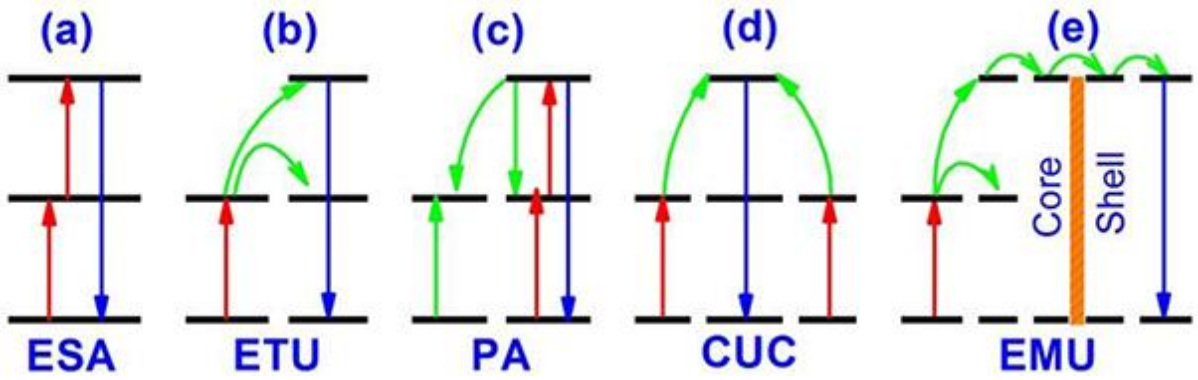

Figure 2. 2 Energy level diagrams describing upconversion processes (a) ESA, (b) ETU, (c) PA, (d) CUC and (e) EMU [29].

2.4 Photodynamic Therapy

Photodynamic therapy (PDT) is a medical treatment that uses drugs called photosensitizing agents along with light to kill cancer cells. The drugs only work after they have been activated by certain kinds of light [30]. When photosensitizers are exposed to a specific light, they produce a form of oxygen that kills nearby cells. Each photosensitizer is activated by light of a specific wavelength as shown in table 2.2, and the wavelength determines how far the light can travel into the body.

Table 2.2 Photosensitizers and the activation energy.

Photosensitizers	Activation wavelengths (nm)
HPD porfimer sodium	630
BPD-MA	689
m-THPC	652
5-ALA	635
5-ALA-methylesther	635
5-ALA-benzylesther	635
5-ALA-hexylesther	345- 400
SnET2	664
Protoporphyrin IX	635
HPPH	665
Lutetium Texaphyrin	732
Phthalocyanine-4	670
Taporfin sodium	664

Depending on the part of the body treated, the photosensitizing agent is either put into the bloodstream through a vein or put on the skin. After certain time the drug is absorbed by cells over the body, it stays in the cancer cells longer than in the normal cells. Approximately 24 to 72 hours after the injection [31]. Healthy cells shed the drugs and the agents remain heavily concentrated in cancer cells. Then the light is applied to the area to be treated. Laser light can be directed through fiber optic cables to deliver light to areas inside the body. Fiber optic cable can be inserted through an endoscope into the lungs or esophagus to treat cancer in these areas. When the photosensitizer is in its excited state, it interacts with molecular triplet oxygen ($^3O_2$) and produce radicals and reactive oxygen species (ROS). These species include singlet oxygen ($^1O_2$), hydroxyl radicals (OH) and superoxide (O_{2^-}) ions. They interact with cellular components, including unsaturated lipids, amino acids residues and nucleic acids. When sufficient oxidative damage ensues, this will result in a target cell death. Figure 2.3 show the PDT treatment and breakdown of molecular oxygen into singlet oxygen and free radicals in the cancer cells. PDT can also destroy the blood vessels that feed the cancer cells.

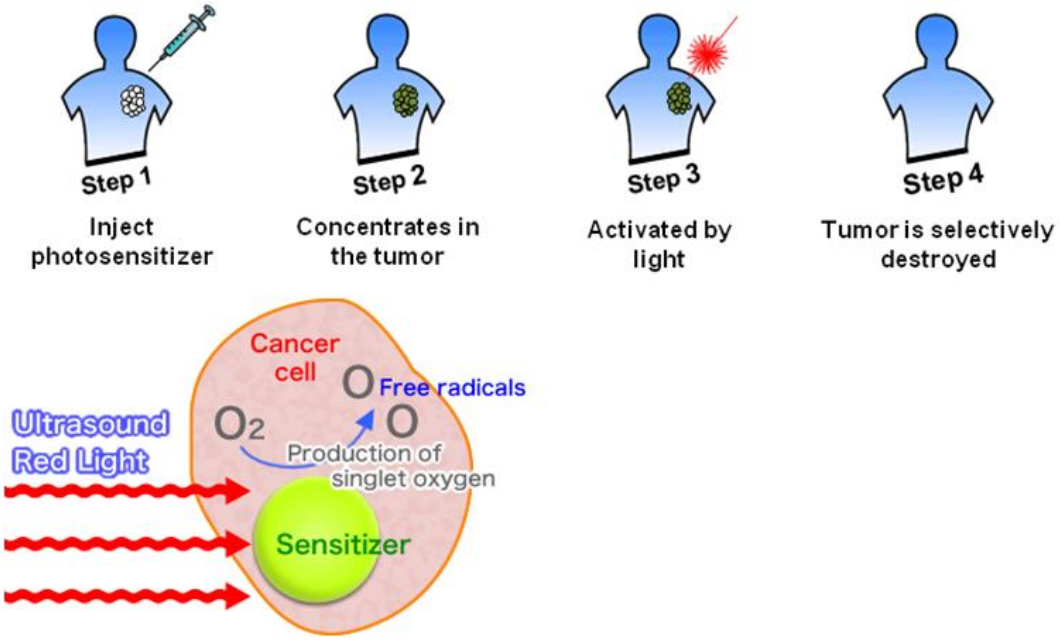

Figure 2. 3 PDT processes [32-33]

Advantages of PDT are as follows:

- It has no long-term side effects when used properly
- Its less invasive than surgery
- It usually takes a short time
- It can be targeted very precisely
- It can be repeated many times at the same site, if needed
- There's usually little or no scarring after the site heals
- It often costs less than other cancer treatment

However, PDT can only treat areas where light can reach; it is mainly used to treat problems on or just under the skin, or in the lining of organs that can be reached with a light source. Because light can't travel very far through body tissues, PDT can't be used to treat large cancers that have grown deeply into the skin or other organs. RE-doped UC nanomaterials are appropriate for a wide range of potential biological applications in photodynamic therapy (PDT), drug delivery, biological imaging, and sensing. Most important point to be concerned for biomedical applications of UC nanomaterials is that the toxicity of the nanoparticles should be evaluated and the nanomaterials must be nontoxic in nature for biological applications.

References

[1] L.J. Vasquez-Elizondo et al., Urea decomposition enhancing the hydrothermal synthesis of lithium iron phosphate powders: Effect of the lithium precursor, Advanced Powder Technology (2017), http://dx.doi.org/10.1016/j.apt.2017.03.031

[2] Z. Zyman, M. Epple, A. Goncharenko, D. Rokhmistrov, O. Prymak, K. Loza, Journal of Crystal Growth, 450, 2016, 190-196

[3] A. Balakrishna, O.M. Ntwaeaborwa, Sensors and Actuators B: Chemical, 242, 2017, 305-317

[4] I.M. Nagpure, K.N. Shinde, S.J. Dhoble, A. Kumar, Journal of Alloys and Compounds, 481, 2009, 632-638

[5] A. Balakrishna, V. Kumar, A. Kumar, O.M. Ntwaeaborwa, Journal of Alloys and Compounds, 686, 2016, 533-539

[6] Y.C. Wu, C.C. Lin, International Journal of Hydrogen Energy, 39, 2014, 7988-8001

[7] Y. Watanabe, Y. Hiruma, H. Nagata, T. Takenaka, Ceramics International, 34, 2008, 761-764

[8] https://en.wikipedia.org/wiki/Rare_earth_element

[9] https://www.dnrm.qld.gov.au/__data/assets/pdf_file/0009/306855/lree.pdf

[10] https://www.thoughtco.com/light-rare-earth-elements-lree-606665

[11] https://www.dnrm.qld.gov.au/__data/assets/pdf_file/0018/238104/hree.pdf

[12] http://www.periodni.com/rare_earth_elements.html

[13]http://www.encyclopedia.com/science-and-technology/chemistry/compounds-and-elements/erbium

[14] https://en.wikipedia.org/wiki/Erbium

[15] K. Binnemas, Coordination Chemistry Reviews, 295, 2015, 1-45

[16] Y.Chen, X. Liu, G. Chen, T. Yang, C. Yuan, Journal of Materials Science: Materials in Electronics, 28, 2017, 5592-5596

[17] https://en.wikipedia.org/wiki/Ytterbium

[18] I. Sokolska, W. Ryba-Romanowski, S. Golab, T. Lukasiewicz, Applied Physics B, 65, 1997, 495-498

[19] H. Jiang, J. Wang, H. Zhang, X. Hu, P. Burns, J.A. Piper, Chemical Physics Letters, 361, 2002, 499-503

[20] Y. Chen, X. Lin, Y. Lin, Z. Luo, Y. Huang, Solid State Communications, 132, 2004, 533-538

[21] http://www.rsc.org/periodic-table/element/68/erbium

[22] http://www.rsc.org/periodic-table/element/63/europium

[23] http://www.rsc.org/periodic-table/element/70/ytterbium

[24] Y. Zhou, W. Pei, X. Zhang, W. Chen, J. Wu, C. Yao, L. Huang, H. Zhang, W. Huang, J.S.C. Loo, Q. Zhang, Biomaterials, 54, 2015, 34-43

[25] Y. Zhang, W. Wei, G.K. Das, T.T.Y. Tan, Journal of Photochemistry and Photobiology C: Photochemistry Reviews, 20, 2014, 71-96

[26] D.H. Kim, J.U. Kang, Microscopy: Science, Technology, Applications and Education, 2010, 571-582

[27] C. Altavilla, Upconverting Nanomaterials;perspectives, synthesis, and applications, ISBN 9781498707749

[28] J. Zhang, Y. Wang, L. Guo, F. Zhang, Y. Wen, B. Liu, Y. Huang, Journal of Solids State Chemistry, 184, 2011, 2178-2183

[29] M.K. Mahata, H. C. Hofsäss, U. Vetter (2016). Photon-Upconverting Materials: Advances and Prospects for Various Emerging Applications, Luminescence - An Outlook on the Phenomena and their Applications, Prof. Jagannathan Thirumalai (Ed.), InTech, DOI: 10.5772/65118. Available from: https://www.intechopen.com/books/luminescence-an-outlook-on-the-phenomena-and-their-applications/photon-upconverting-materials-advances-and-prospects-for-various-emerging-applications.

[30]https://www.cancer.org/treatment/treatments-and-side-effects/treatment-types/photodynamic-therapy.html

[31] https://www.cancer.gov/about-cancer/treatment/types/surgery/photodynamic-fact-sheet

[32] http://www.resurrection-clinics.eu/index.php/de/13-therapy/97-photodynamic-pdt-and-sonodynamic-therapy-sdt-english

[33] http://www.photolitec.org/Tech_PDT.html

Chapter 3

Synthesis method and Research Technique

3.1 Introduction

In this chapter, a brief description of synthesis method and different research techniques used to prepare and characterize the prepared phosphor materials is discussed. The research techniques used to analyse the crystalline structure, vibrational bands/modes, particle morphology, chemical composition, absorption and bandgap energy, and photoluminescence were Bruker AXS D8 X-ray Diffraction (XRD), Fourier Transform Infrared (FTIR) spectroscopy, Jeol JSM-7800F thermal field emission scanning electron microscopy (FE-SEM) coupled with Oxford Aztec 350 X-Max80 Energy x-ray Dispersive Spectroscopy (EDS), Perkin Elmer Lambda 950 UV-Vis spectrometry, Cary eclipse fluorescence with monochromatized xenon lamp, fiber-coupled 980 nm NIR (near infrared) laser as the excitation source, iHR320 Horiba Yvon imaging spectrometry, R943 -02 Hamamatsu Photonics photomultiplier (PMT) detector and a SR830 Standford Research System lock-in amplifier, and Edinburgh Instruments FLS980 Fluorescence Spectrometer with 980 nm NIR laser as the excitation source and photomultiplier (PMT) detector, respectively. The urea combustion method was used to prepare different phosphor materials. Detailed description on this type of synthesis method will be discussed at the end of this chapter.

3.2. Synthesis method

3.2.1 Combustion method

Combustion synthesis is an attractive, effective, and low cost synthesis method of nanomaterials for variety of advanced applications. It is a versatile, simple and a rapid process, which allows effective synthesis of nanosize materials. It has become a very popular approach or preparation of nanomaterials and a number of breakthroughs in this field have been made, notably for development of new catalysts and nanocarriers with properties better than those for similar traditional materials [1]. This process involves a self-sustained reaction in homogenous solution of different oxidizers (e.g. metal nitrates) and fuels (e.g. urea, citric

acid and glycine). The mixture of metal nitrates and fuel are broken down quickly by deflagration burning or combustion [2]. During the combustion process a large volume of gases evolve, leading to formation of fine powders. Excellent homogeneity is obtained when the precursors are well mixed, which is when oxidants and fuel are dissolved in water. The fuel serves as a complexing agent, limiting the precipitation of individual precursor components prior to ignition and also for the synthesis of nanocrystalline metal oxides. This method is based on the principle that once a reaction is initiated under heating, an exothermic reaction occurs and becomes self-sustained within a certain time interval resulting in a final product. Choice of fuel is very important in deciding the exothermicity of the redox reaction between the metal nitrate and the fuel. The fuel must satisfy the following criteria: (i) it should be water soluble, (ii) have low ignition temperature, (iii) the combustion should be controlled and smooth and not lead to explosion, (iv) should give out large amounts of low weight and environmentally safe gases, (v) be readily available or easy to prepare and (vi) yield no other residual mass except the oxide [3]. In this study, urea was used as a fuel to prepare nanomaterials. Urea is an attractive fuel for originating the formation of powders with crystallite sizes in the nanosized range and act as a complexing agent for metal ions because it contains two amino group located at the extremes of its chemical structure. It is also a source of C, H, and N which on combustion form simple gaseous molecules of N_2, CO_2 and H_2O and liberate heat. Snapshots in figure 3.1 show the urea combustion synthesis.

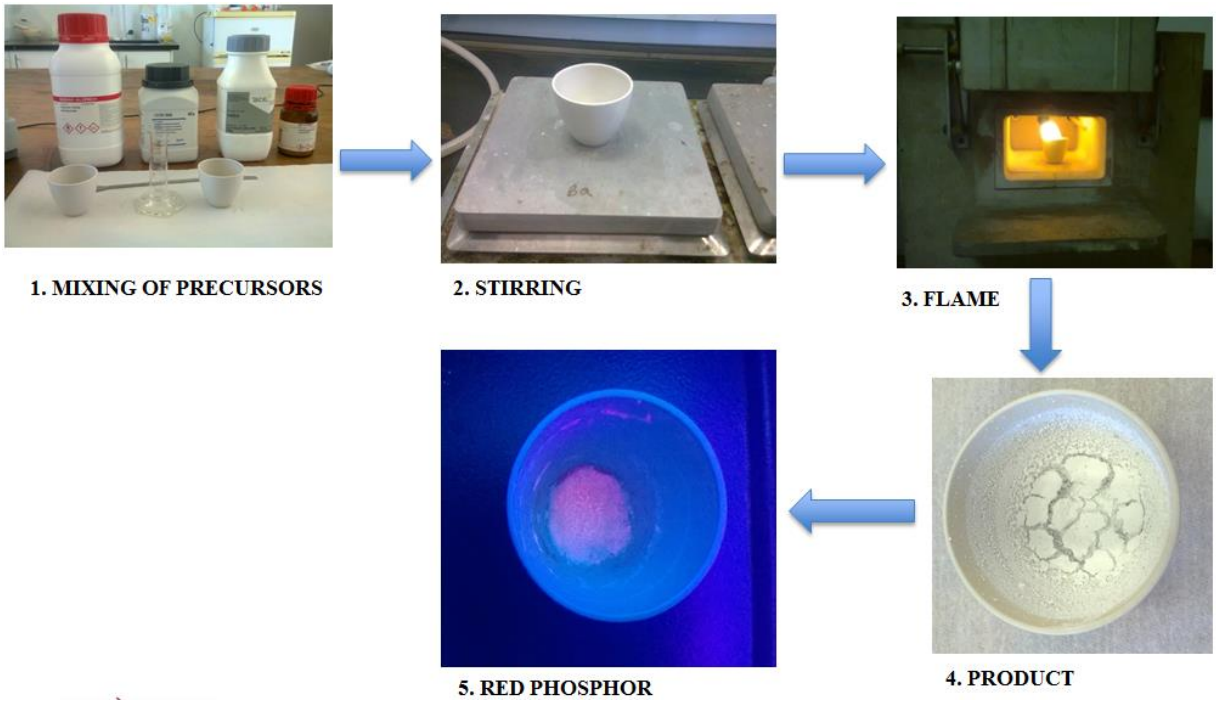

Figure 3. 1 Combustion method of nanomaterials.

3.3. Characterization Techniques

3.3.1 X-ray Diffraction (XRD)

X-ray Diffraction (XRD) is an analytical technique primarily used for phase identification of unknown crystalline material and can provide information on unit cell. It is now commonly used for the study of crystal structure, crystallite size, strain and atomic spacing [4]. It is based on the constructive interference of monochromatic X-rays and a sample. X-ray diffractometer consists of three basic elements: an X-ray tube, a sample holder, and X-ray detector. The X-rays are generated in a cathode ray tube, filtered to produce monochromatic radiation, collimated to concentrate and directed toward the samples by applying voltage. The interaction of the incident rays with the sample produces constructive interference when conditions satisfy Bragg's Law:

$$n\lambda = 2d \sin\theta \qquad (3.1)$$

where n (an integer) is the order of the reflection, λ is the wavelength of the incident X-rays, d is the interplanar spacing of the crystal and θ is the angel of incidence. The equation is described as follows: constructive interference occurs only if the path difference (given by 2d Sinθ) is a multiple (n=1, 2, …) of the used wavelength of the X-ray beam. The scattered X-rays from the sample interfere with each other, and detectors can only read-out the signal at

the angles where constructive interference occurs. This is schematically shown in figure 3.2.

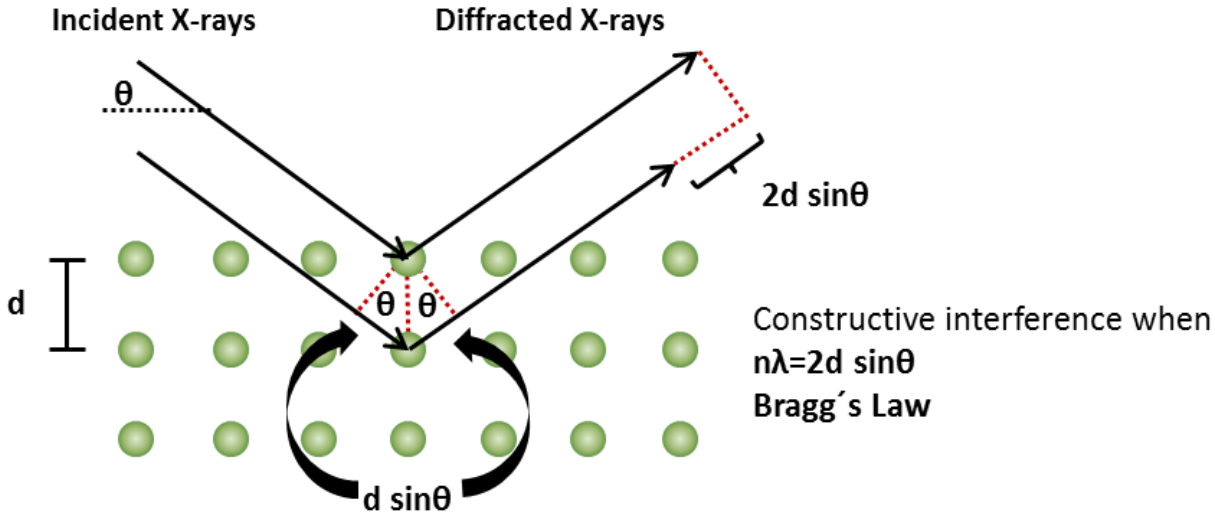

Figure 3. 2 Bragg's Law reflection on X-ray diffraction by crystal plane [5].

By scanning the samples through a range of 2θ angles, all possible diffraction directions of the lattice are attained due to the random orientation of the material. XRD pattern is the fingerprint of the periodic atomic arrangements in a given sample/material. International Centre for Diffraction Data (ICDD) database of XRD enables the phase identification of samples. The diffraction patterns are used in the determination of crystallite size. The average crystallite size can be estimated from the broadened peaks using Scherrer equation:

$$D = \frac{0.9\lambda}{\beta Cos\theta} \tag{3.2}$$

where λ is the wavelength, β is the line broadening at half maximum intensity, θ is the Bragg angle.

In this study, D8 Advanced AXS GmbH X-ray diffractometer shown in figure 3.3 was used. The XRD patterns were recorded in the 2θ range of 10-80^0 at a scan speed of 0.0020 s^{-1}, with accelerating voltage of 40 kV and current of 40 mA, and a continuous scan mode with coupled 2θ scan type was used.

Figure 3. 3 D8 Advanced AXS GmbH X-ray difffractometer.

3.3.2 Fourier Transform Infrared (FTIR) spectroscopy

Fourier Transform Infrared (FTIR) spectroscopy is technique used to identify types of chemical bonds or presence of certain functional group of molecules by producing an infrared absorption spectrum that is a molecular fingerprint and the wavelength of absorbed light is characteristic of the chemical bonds. It is based on the vibrations of the atoms of the molecule. One of the greatest advantages of the infrared spectroscopy is that virtually any sample in any state may be analysed. For example, liquids, solutions, pastes, powders, films, fibres, gases, and surfaces can all be examined this technique [6]. The spectrometer consists of a source, beamsplitter, two mirrors, a laser, and a detector; the beamsplitter and mirrors are collectively called interferometer. The assembled diagram is shown in Figure 3.4

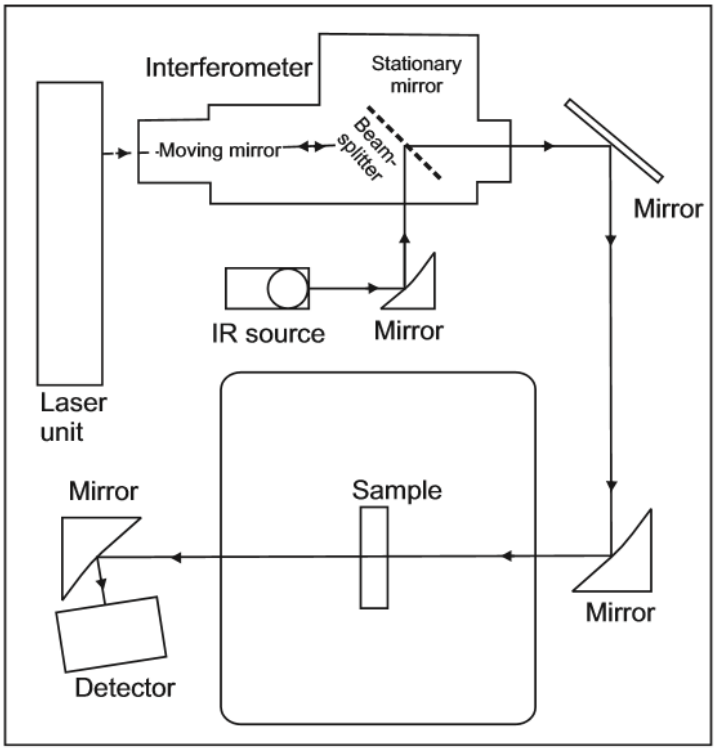

Figure 3. 4 Schematic diagram of IR spectroscopy [7].

The IR light from the source strikes the beamsplitter, which produces two beams of roughly the same intensity. One beam strikes a fixed mirror and returns, while the second strikes a moving mirror. A laser parallels the IR light, and also goes through the interferometer [8]. The moving mirror oscillates at a constant velocity, timed using the laser frequency. The two beams are reflected from the mirrors and are recombined at the beamsplitter and interfere. The IR beams then passes through the sample, where some energy is absorbed and some is transmitted. The transmission portion reaches the detector, which records the total energy.

The absorption or transmission of the IR radiation is commonly measured as a function of wavenumber. A wavenumber is the reciprocal of the wavelength and is commonly expressed in unit of cm^{-1}. The infrared spectrum can be divided into three main regions: the *far infrared* (<400 cm^{-1}), the *mid infrared* (4000-400 cm^{-1}) and the *near-infrared* (13 000-4000 cm^{-1}) [9]. The most scanned wavenumbers are 4000 to 400 cm^{-1}, which encompass absorptions by the majority of common organic functional groups. For a molecule to absorb IR radiation, it must change its dipole moment upon vibration, and the frequency of the radiation must exactly match the natural vibrational frequency of the molecule, resulting in a change in the amplitude of the vibration. There are two fundamental types of molecular vibrations are stretching and bending modes [10]. The stretching mode consists of a change in the distance

along the axis of a bond between two atoms. The bending bond results from the change in the angle between two bonds.

In this study, Nicolet 6700 FTIR spectrometer was used to measure the vibrational frequency modes of the samples. The spectrometer is shown in Figure 3.5.

Figure 3. 5 Nicolet 6700 FTIR spectometer.

3.3.3 Scanning Electron Microscopy (SEM)

Scanning Electron Microscopy is a technique that is used to produce images of the sample by scanning the surface with a focused beam of electrons. The electrons interact with the atoms in the sample, producing various signals that contain information about the sample's surface topography and composition [11]. The main components of SEM are electron column, scanning system, detectors, display, vacuum system and electronic controls. The electron column is consists of an electron gun and two or more electromagnetic lenses operating in vacuum. The electron gun generates free electrons and accelerates these electron to energies in the range 1-40 KeV in the SEM [12]. The electron lenses create a small, focused electron probe on the specimen. In order to produce images, the electron beam is focused into a fine probe, which is scanned across the surface of the specimen with help of scanning coils. Each point of the specimen that is struck by the accelerated electrons emits signal in the form of electromagnetic radiation. Selected portion of radiation, usually secondary electron (SE) or backscattered electrons (BSE) are collected by detector and resulting image is generally straightforward to interpret at least for topographic imaging of objects at low magnifications. A schematic drawing of SEM is shown in Figure 3.6.

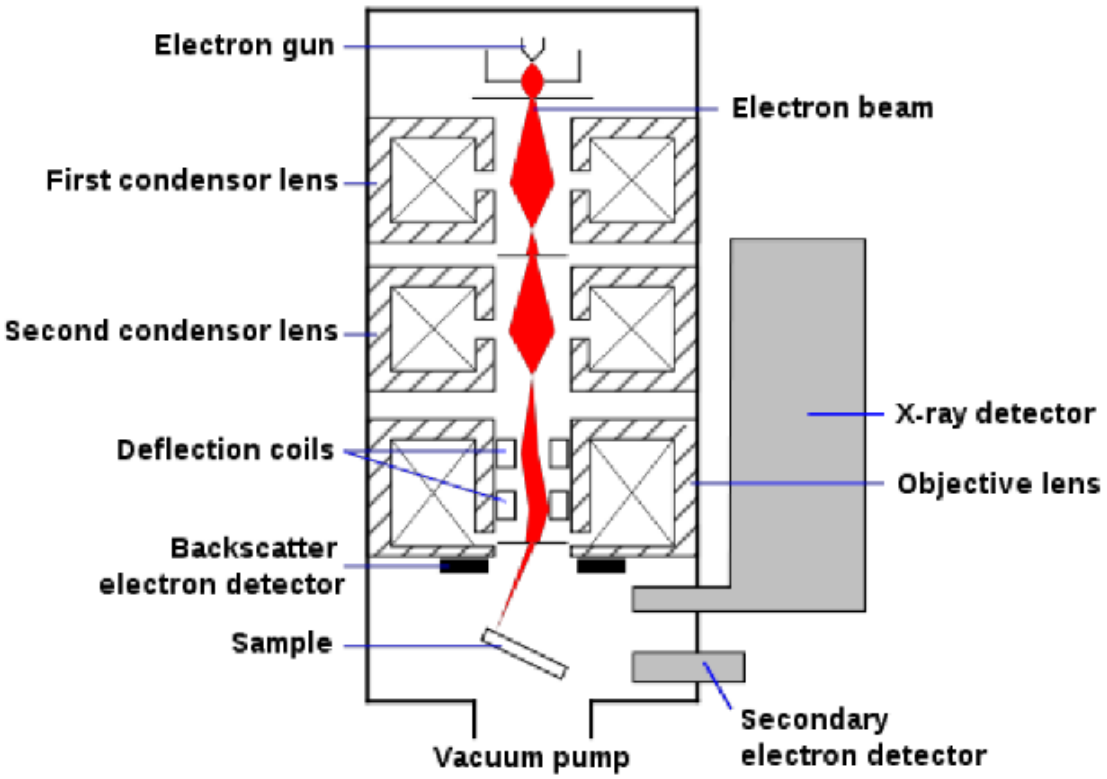

Figure 3. 6 Schematic diagram of SEM column [11].

Accelerated electron in an SEM carry significant amounts of kinetic energy, and this energy is dissipated as a variety of signals produced by electron-sample interactions when the incident electrons are decelerated in the solid sample [12]. The signals include secondary electrons (that produce SEM images), backscattered electrons (that produce atomic number and phase difference), and characteristic X-rays (characteristic X–rays that are used for elemental analysis). Secondary electrons and backscattered electrons are commonly used or imaging samples. Secondary electrons are most valuable for showing morphology and topography on samples and backscattered electrons are most valuable for illustrating contrasts in composition in multiphase samples. Elements with higher atomic numbers have more positive charges on the nucleus; as a result, more electrons are backscattered, causing the resulting backscattered signal to be higher [13]. Since heavy elements (high atomic number) backscatter electrons more strongly than light elements (low atomic number), and thus appear brighter in the mage.

3.3.3 Energy Dispersive X-ray Spectrometry (EDS)

EDS is a powerful technique that is that is ideal for revealing chemical composition of elements. It is possible to determine which elements are present in the surface layer of the sample (at the depth in micrometer range) and where these elements are present (mapping technique). Using a process known as X-ray mapping, information about the elemental composition of a sample can be overlaid on top of the magnified image of the sample. EDS detect the characteristic X-rays generated when a solid sample is bombarded with high energy electrons in an electron microscope to obtain a localized chemical analysis. Figure 3.7 shows that the electrons in the deeper electron shell can be ejected by primary electrons, resulting in an electron hole [14]. When this lower-shell position is filled by an electron from higher shell energy is released as X-ray. These characteristic X-rays are used to identify the composition and measure the abundance of elements in the sample. X-ray intensities are measured by counting photons and precision obtainable limited by statistical error. X-rays emitted by each element present in a sample bears a direct relationship with the concentration of that element (mass or atomic fraction).

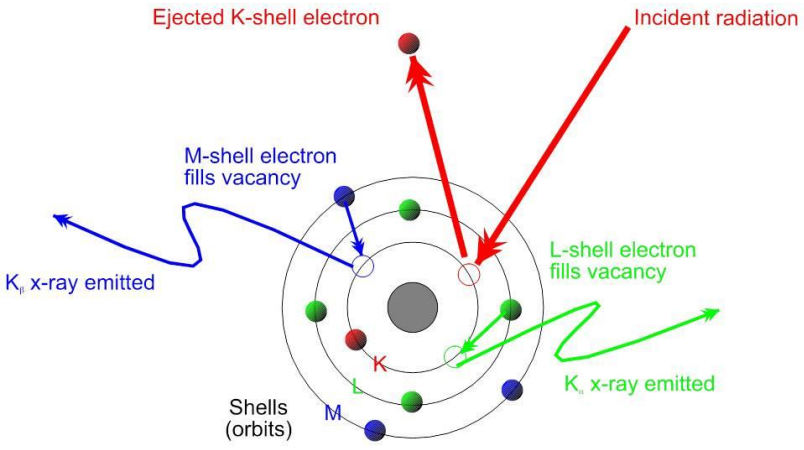

Figure 3.7 Schematic of X-ray fluorescence process [15].

The X-rays are detected by Energy Dispersive X-ray detector which displays the signal as a spectrum of X-ray count rate versus X-ray energy. The EDX detector is attached to the SEM as shown in Figure 3.8.

Figure 3. 8 JEOL-JSM7800 Field Emission Scanning Electron Microscope.

3.3.4. Ultraviolet-visible (UV-Vis) spectrophotometry

Ultraviolet-visible spectrophotometry is a technique that is used to measure absorption and reflectance in the ultraviolet-visible spectral region. In this region of the electromagnetic spectrum, atoms and molecules undergo electronic transitions [16]. Absorption is complementary to fluorescence, fluorescence deals with transitions from the excited state to the ground state, while absorption measures transitions from the ground state to the excited state. The instrument measures the intensity of light passing through a sample (I), and compares it to the intensity of light before it passes through the sample (I_0). The ratio I/I_0 is called transmittance, and is usually expressed as a percentage (%T). The absorbance (A) is based on the transmittance:

$$A = -\log\left(\frac{\%T}{100\%}\right) \tag{3.3}$$

The absorption data can be used to determine the bandgap energy (E_g) of the material. Bandgap indicates the difference in the energy between the top of the valence band and the bottom of the conduction band. The bandgap is determined by using Tauc's relation:

$$(\alpha h\nu) = A(h\nu - E_g)^n \tag{3.4}$$

where h is Planck's constant, v is frequency of vibration, α is absorption coefficient, A is proportional constant, n denotes optical electronic transition, and E_g is bandgap energy. E_g is estimated by extrapolating a tangent line through a plot of $(h\nu\alpha)^n$ against $h\nu$.

The UV-Vis spectrophotometer can be used to measure reflectance. The spectrophotometer measure the intensity of light reflected from a sample (I), and compares it to the light reflected from a reference material (I_0). The ratio I/I_0 is called reflectance, and is usually expressed as a percentage (%R). The reflectance data can be used to determine the bandgap energy (E_g) of the material. The bandgap is determined by using Kubelka-Munk function:

$$F(R_\infty) = \frac{(1-R_\infty)^2}{2R_\infty} = \frac{K}{S} \tag{3.5}$$

where $F(R)$ is Kubelka-Munk function, R is the fractional reflectance, S is the scattering coefficient and K is the absorption coefficient [17]. E_g is estimated by extrapolating the K-M function to K/S=0.

The basic components of spectrophotometer are a light source, a holder for the sample, diffraction grating in a monochromator or a prism to separate the different wavelengths of light, and a detector. The radiation source is often a tungsten lamp (300-2500 nm), and deuterium lamp (190-400 nm). The detector is typically a photomultiplier or photodiode. Single photodiode detectors and photomultiplier tubes are used with scanning monochromator, which filter the light of a single wavelength reaches the detector at one time. The layout of UV-Vis spectrophotometer is demonstrated by figure 3.9.

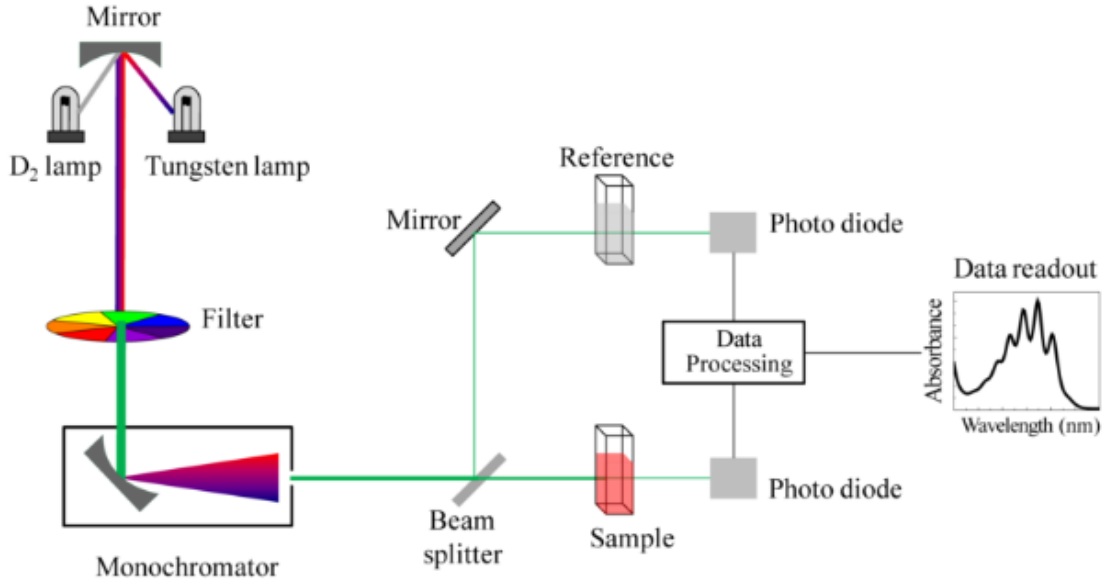

Figure 3. 9 Schematic diagram of UV-Vis spectrophotometer [18].

Figure 3.10 and 3.11 below show the Perkin Elmer Lambda 950 UV-Vis and UV/VIS/NIR spectrometers that were used in this study to measure the diffuse reflectance spectra.

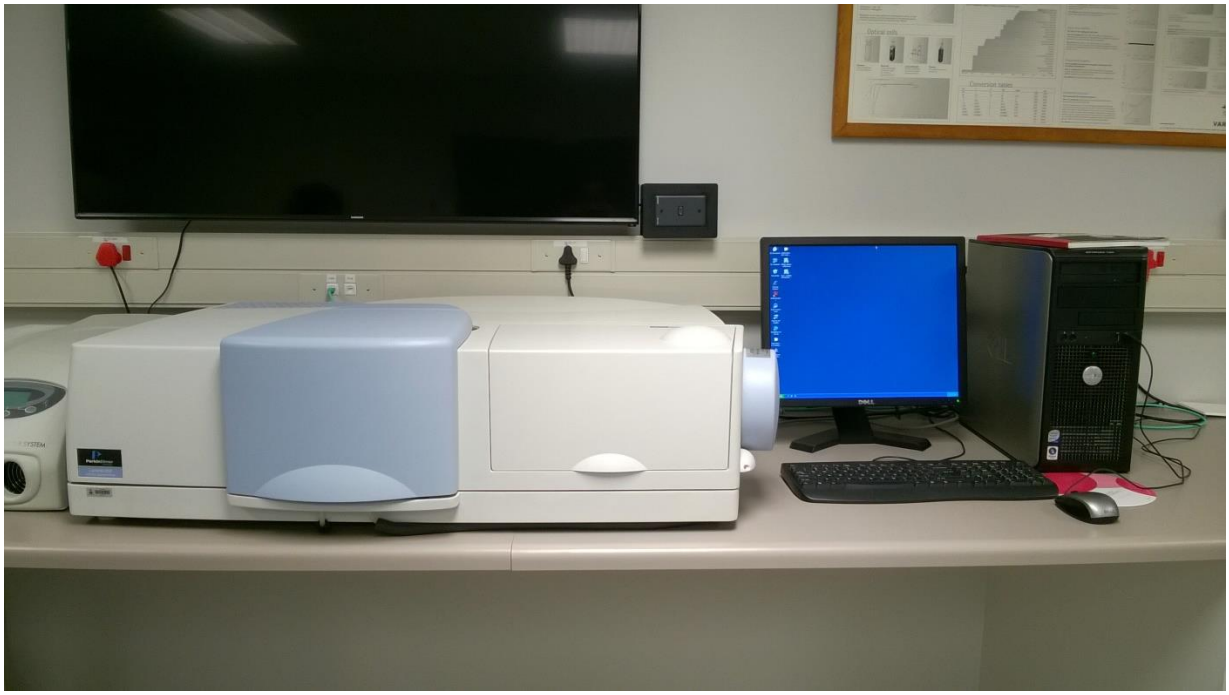

Figure 3. 10 Perkin Elmer Lambda UV-Vis spectrometer.

Figure 3. 11Perkin Elmer Lambda 950 UV/Vis/NIR spectrometer.

3.3.4. Photoluminescence (PL) spectroscopy

3.3.4.1 Fluorescence Spectrophotometry

Fluorescence spectroscopy is a technique that is used to measure the intensity of photons emitted from a sample after it has absorbed photons. Fluorescence occurs when a fluorescent material is excited into a higher electronic state by absorbing an incident photon and cannot

return to the ground state except by emitting a photon [19]. The emitted photons will have different energies. The technique consists of the following components, the light source (Xenon lamp) which produces photons, monochromator that allow only selected wavelength to pass through to the sample cell and analysis of sample emission. The luminescence given is then converted to the electric signal that is processed by the electric device and finally controlled by the computer. The emission spectrum is obtained by measuring and plotting the intensity of light of sample as a function of wavelength. Figure 3.12 show the outline of the schematic diagram of fluorescence spectroscopy. In this study, Varian Cary-Eclipse spectrometer was used to measure the luminescence of the samples. The spectrometer is shown in Figure 3.13.

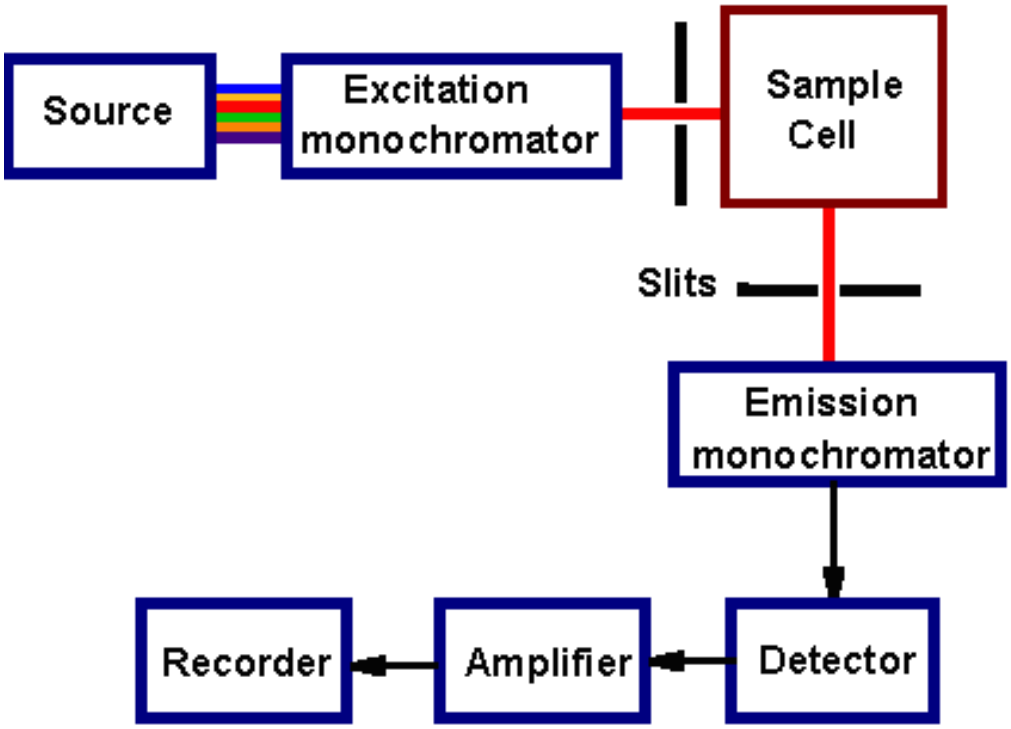

Figure 3. 12 Schematic diagram of fluorescence spectroscopy [20].

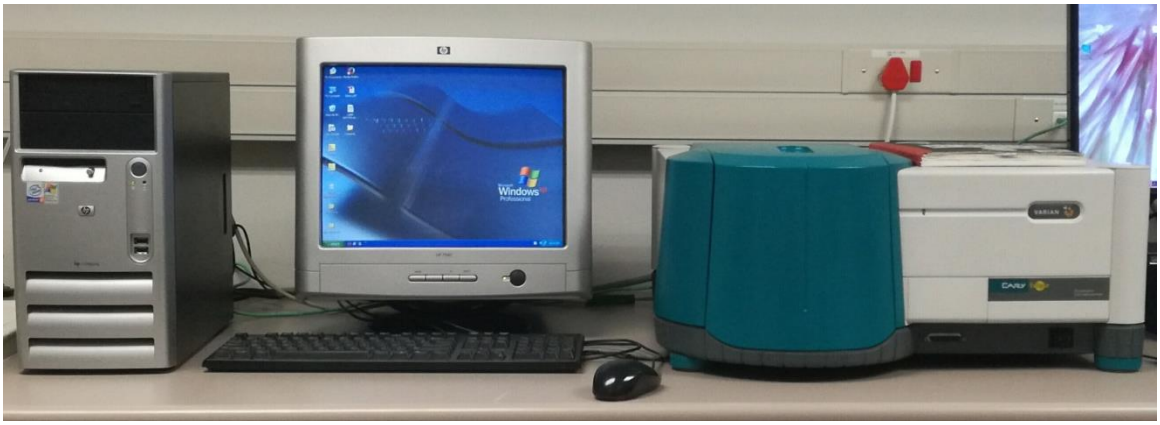

Figure 3. 13 Varian Cary-Eclipse spectrometer.

3.3.4.2 Helium-Cadmium Laser

Helium-Cadmium (HeCd) laser is a gas laser. It uses helium in conjunction with a metal with a low vaporization temperature. The lasing element, cadmium, is heated to convert it into the gas phase. The basic components of the HeCd laser consist of a tube, terminated by two Brewster angle windows with two laser mirrors mounted separately from the tube. In the setup, the tube of the laser is filled with helium gas, cadmium reservoir and a heater located near the main anode. The heater is used to vaporize the metal. The desired vapour of Cd in the tube is produced when the reservoir is raised to high temperature of ~250 ^{0}C. The measurements are done by directing the laser beam to the sample by using lenses and mirrors, followed by the chopper, to ensure that the light beam from the sample is directed to the photomultiplier tube detector. The schematic setup of the laser is shown by figure 3.14 (a). This type of laser is used for applications in biological fluorescence, cancer detection, photoluminescence, and optical data storage [21]. The lasers demonstrated in figure 3.14 (b) and (c) were used to measure the upconversion luminescence of the samples. Varian Cary-Eclipse, He-Cd laser and FLS 980 spectrometers using 980 nm IR lasers were used to measure the luminescent properties of the samples.

The next few chapters are presented as parts of papers and some repetition may occurred in the different chapters.

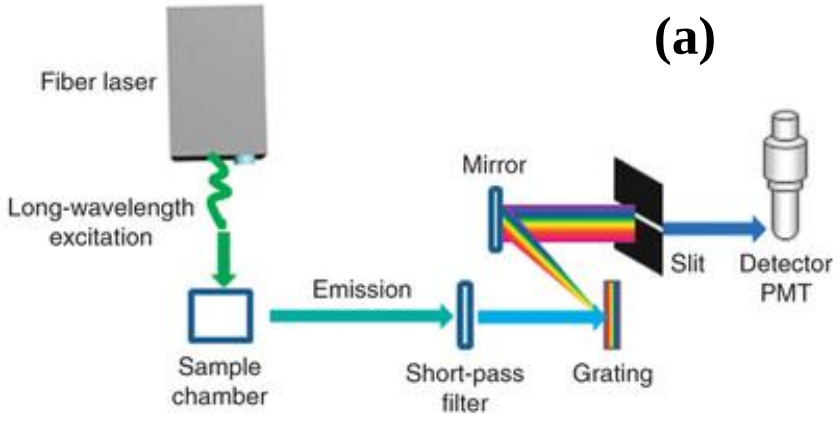

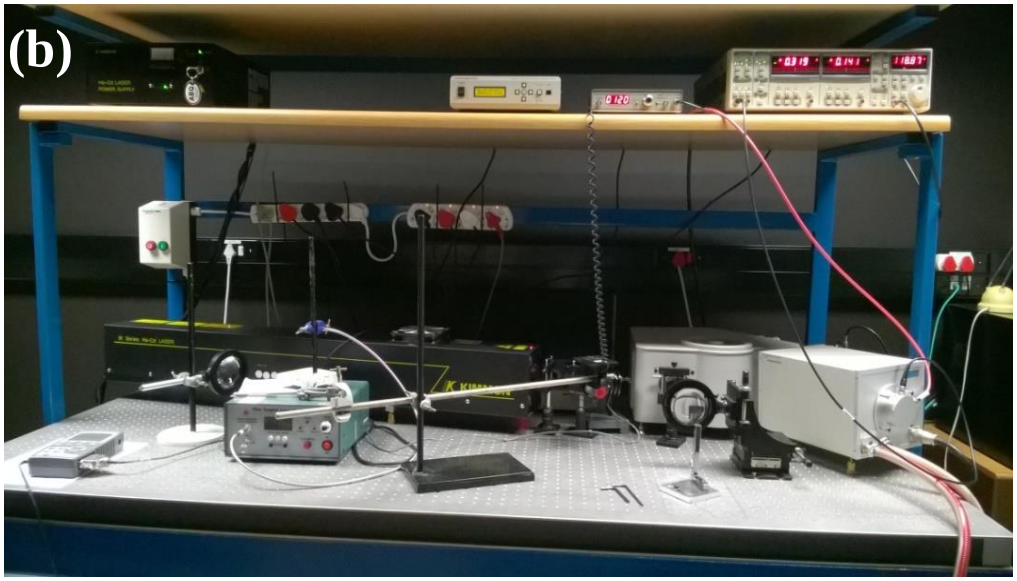

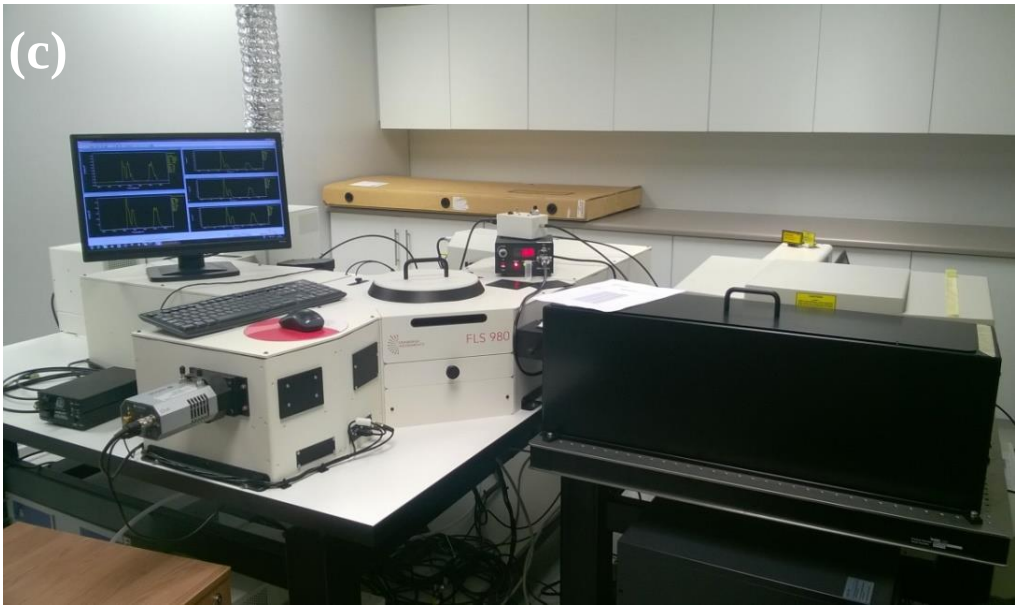

Figure 3. 14 (a) schematic setup of the laser, (b) He-Cd laserand (c) FLS 980 Spectrometers used to investigate luminescence properties of samples [22].

References

[1] T.S Aruna, A.S. Mukasyan, Current Opinion in Solid State and Materials Science, 2008, 12, 44-50

[2] A. Alves, C.P. Bergmann, F.A. Berutti, Novel Synthesis and Characterization of Nanostructured Materials, 2013, ISBN: 978-3-642-41274-5

[3] M. Lackner, Combustion Synthesis:Novel Routes to Novel Materials, 2010, ISBN:978-1-60805-155-7

[4] http://serc.carleton.edu/research_education/geochemsheets/techniques/XRD.html

[5] http://wiki.anton-paar.com/x-ray-diffraction-xrd/

[6] Mizi Fan, Dasong Dai and Biao Huang (2012). Fourier Transform Infrared Spectroscopy for Natural Fibres, Fourier Transform - Materials Analysis, Dr Salih Salih (Ed.), ISBN: 978-953-51-0594-7, InTech, Available from: http://www.intechopen.com/books/fourier-transform-materials-analysis/fourier-transform-infraredspectroscopy-for-natural-fibres

[7] http://www.pitt.edu/~mramsey/papers/GAC2.pdf

[8]https://tools.thermofisher.com/content/sfs/brochures/TN50674-E-0215M-FT-IR-Advantages.pdf

[9] http://www.kinetics.nsc.ru/chichinin/books/spectroscopy/Stuart04.pdf

[10] http://aerosol.chem.uci.edu/AirUCI_summer/PDFs/labs/2014_FTIR_Lab.pdf

[11] https://en.wikipedia.org/wiki/Scanning_electron_microscope

[12] file:///E:/D/Recovered%20FAT%20Partition%20@%2032736/PhD%20Project/FE-SEm/sem-intro.pdf

[13]http://homes.ufam.edu.br/berti/nanomateriais/aulas%20pptx%20e%20livros/livro/Scanning%20Microscopy%20for%20Nanotechnology/Fundamentals%20of%20Scanning%20Electron%20Microscopy%20(SEM).pdf

[14]file:///E:/D/Recovered%20FAT%20Partition%20@%2032736/PhD%20Project/Literature/EDS/EDS SEM.pdf [access 8/24/2017]

[15] https://www.bruker.com/products/x-ray-diffraction-and-elemental-analysis/handheld-xrf/how-xrf-works.html[acess 8/25/2017]

[16] https://en.wikipedia.org/wiki/Ultraviolet%E2%80%93visible_spectroscopy

[17] D. Xu, F. Zhanfg, Y. Sun, Z. Yang, X. Dong, S. Pan, Royal Society of Chemistry, 2016, 40, 7407-7413

[18] https://chem.libretexts.org/Textbook_Maps/Organic_Chemistry_Textbook_Maps/Map%3A_Organic_Chemistry_with_a_Biological_Emphasis_(Soderberg)/Chapter_04%3A_Structure_Determination_I/4.4%3A_Ultraviolet_and_visible_spectroscopy

[19] http://www2.warwick.ac.uk/services/ris/impactinnovation/impact/analyticalguide/fluorescence/

[20] http://elchem.kaist.ac.kr/vt/chem-ed/spec/molec/mol-fluo.htm

[21] http://www.photonicsolutions.co.uk/product-detail.php?prod=5992

[22] Q. Liu, W. Fei, T. Yang, T. Yi, F. Li, Nature Protocol, 2013, 8, 2033-2044

Chapter 4

Enhanced upconversion emission of Er^{3+}/Yb^{3+} co-doped barium hydroxide phosphate phosphors

4.1. Introduction

In recent years, rare earths ions doped phosphates have gained much attention due to their numerous uses in applications such as X-rays, gamma ray scintillators, plasma display and lasers, among other things [1]. Barium phosphate, for example, has generated interest for a variety of technological applications due to several exclusive properties such as high thermal expansion coefficient, low viscosity, ultraviolet (UV) transmission, electrical conductivity and non-toxicity [2]. They are biocompatible and can easily form bonds with tissues in the human body. With their high biocompatibility and good surface properties, synthetic barium phosphates materials have promising application in biomedicine. PO_4^{3-} group has a capacity for substitution or to bond with other cations and anions. This makes them even appropriate to serve as hosts for rare earths dopant ions such as erbium (Er^{3+}), ytterbium (Yb^{3+}), europium (Eu^{3+}), praseodymium (Pr^{3+}), gadolinium (Gd^{3+}) and terbium (Tb^{3+}), among others, to prepare light emitting materials or phosphors that can be used in a variety of applications including general lighting, energy efficiency, theft prevention, advertising, diagnosis and phototherapy [3]. The focus of this chapter is on the synthesis and photoluminescence (PL) upconversion properties of Er^{3+} and Yb^{3+} co-doped barium hydroxide phosphate or $Ba_5(PO_4)_3OH$. Erbium ion (Er^{3+}) has got good chemical, photothermal, photochemical stabilities as well as low phonon-energy. It possesses excellent electronic energy level scheme with equally spaced and longer lifetime excited states, which are favourable for upconversion of near infrared (NIR) light to visible light [4]. In addition, it can also be used as auxiliary ions to serve as trap center to improve the long afterglow properties. In our study, ytterbium ion (Yb^{3+}) is used as a sensitizer of upconverted photoluminescence from Er^{3+} since it has a large absorption cross section around the wavelength of 980 nm, therefore it has got the potential to harvest primary excitation energy and transfer it non-radiatively to Er^{3+} thereby enhancing the photoluminescence intensity of the upconverted emission [5]. As sensitizer, Yb^{3+} acts to harvest and transfer the primary NIR excitation energy (absorbed at

980 nm) to excite the second (co-dopant) trivalent rare earth ion (Er^{3+} in our case) that will relax to the ground state, producing up-converted emission in the visible region of the spectrum. It has two energy levels, namely the ground $^2F_{7/2}$ state and the excitation $^2F_{5/2}$ state. Its excitation state matches well with the transition energy between the $^4I_{11/2}$ and $^4I_{15/2}$ states and $^4F_{7/2}$ and $^4I_{11/2}$ states of Er^{3+} ion.

This chapter reports on the urea combustion synthesis of $Ba_5(PO_4)_3OH$ based phosphor materials either singly doped with Er^{3+}/ Yb^{3+} or co-doped with $Er^{3+}$and Yb^{3+} ions. This synthesis method is quick, simple and cost-effective. Lately it is commonly used for synthesis of different materials with particles sizes in the nanoscale. The structure, particle morphology, absorption and upconversion luminescence properties of the phosphors were investigated for possible applications in photodynamic therapy.

4.2. Experimental

4.2.1 Preparation of phosphor powders

$Ba_5(PO_4)_3OH$ co-doped Er^{3+}/Yb^{3+} phosphor powders were synthesized by combustion method using urea as a fuel. The following starting materials with 99% purity were used for the preparation of materials reported in this paper: strontium nitrate (6M $Ba(NO_3)_2{\cdot}4H_2O$), di-ammonium hydrogen phosphate ((4M $NH_4)_2HPO_4$), erbium nitrate ($Er(NO_3)_3{\cdot}5H_2O$), ytterbium nitrate ($Yb(NO_3)_3{\cdot}6H_2O$) with different concentrations of Er^{3+} (3 mol %), Yb^{3+} (7 mol %), and Er^{3+}:Yb^{3+} (3:5-15 mol %), and urea ($CO(NH_4)_2$). When a complete reaction is assumed, the theoretical equation for the formation of $Ba_5(PO_4)_3OH$ is given by:

$$15Ba(NO_3)_2{\cdot}4H_2O + 9(NH_4)_2HPO_4 + 16CH_4N_2O = 3Ba_5(PO_4)_3OH + 16CO_2 + 131H_2O + 40N_2 \quad (4.1)$$

All reagents, in stoichiometric amounts, were dissolved in 2 ml of distilled water and the mixture was stirred vigorously for 15 min in room temperature until a thick homogenous solution was formed. The solution was kept in a furnace for 10 minutes maintained at 600 °C. The solution boiled, underwent dehydration and decomposed while generating combustible gases such as CO_2, N_2 and H_2O. The combustion ashes were cooled to room temperature and were ground gently using a pestle and mortar resulting in a fine powder. The materials synthesized were $Ba_5(PO_4)_3OH$, $Ba_5(PO_4)_3OH:Er^{3+}$, $Ba_5(PO_4)_3OH:Yb^{3+}$ and $Ba_5(PO_4)_3OH:Er^{3+},Yb^{3+}$. All the powders were annealed at 800 °C in air for 2 hours.

4.2.2 Measurements

The crystalline structure of the phosphors was analyzed using a Bruker AXS D8 X-ray Diffraction (XRD) with Cu Kα1 radiation (λ = 1.5406Å) in the range from 20 to 60° (2θ). The schematic representation of the different sites of Ba with the coordination PO_4^{3-} material was drawn using DIAMOND crystal structure software. The vibrational bands/modes were analyzed using Fourier Transform Infrared (FTIR) spectrometer. Particle morphology was examined using Jeol JSM-7800F thermal field emission scanning electron microscope (FE-SEM) coupled with Oxford Aztec 350 X-Max80 Energy Dispersive X-ray Spectroscopy (EDS) which was used to analyse the chemical composition of the phosphors under typical vacuum of 9.634×10^{-5} Pa. The absorption and bandgap energy were evaluated using Perkin Elmer Lambda 950 UV-Vis spectrometer. Upconversion photoluminescence emission was measured by using a photoluminescence system consisting of fibre-coupled 980 nm NIR (near infrared) laser as the excitation source, iHR320 Horiba Yvon imaging spectrometer, R943 -02 Hamamatsu Photonics photomultiplier (PMT) detector and a SR830 Standford Research System lock-in amplifier.

4.3. Results and Discussion

4.3.1 Phase analysis

The XRD patterns of $Ba_5(PO_4)_3OH$ powder measured at room temperature in the range of 2θ from 20° to 60° are shown in Figure 4.1. The diffraction pattern exhibited hexagonal structure referenced in the ICDD Card Number [00-024-0028]. There were no peak shifts nor secondary peaks observed suggesting that pure phases of $Ba_5(PO_4)_3OH$ were crystallized. The sharp peaks point to the formation of $Ba_5(PO_4)_3OH$ with fine and pure crystallinity. The crystallite size of the powder was determined using the Debye-Scherrer equation.

$$D = \frac{k\lambda}{\beta \cos\theta} \tag{4.2}$$

Where

k is the Scherrer's constant (0.98)

λ is the wavelength of X-ray (1.54060 Å)

β is the full-width at half maxima

θ is the Bragg angle of the XRD peak

The average crystallite size estimated was 39 nm for annealed powder at 1000 ^{o}C in air. The pure phase of the $Ba_5(PO_4)_3OH$ shows that it crystallized in the hexagonal system with the space group $P6_3$ (173). This allows ease of incorporation of rare earth ions in the host lattice. A schematic crystal structure of hexagonal unit cell of $Ba_5(PO_4)_3OH$ is presented in Figure 4.2. The crystallographic parameters of $Ba_5(PO_4)_3OH$ are shown in Table 4.1.

There are two non-equivalent crystallographic sites in each unit cell for the Ba, name Ba_1 atom at the 6c Wyckoff position and Ba_2 atom at the 2b Wyckoff position. The P and O atoms form the PO_4 tetrahedral group. The OH group are located in the channels built up from Ba atoms. The location of OH group allows them to move freely under certain activation energy and the activity of OH group can have a great effect on the electric properties of $Ba_5(PO_4)_3OH$ [6]. Table 4.2 shows the structural parameters of $Ba_5(PO_4)_3OH$ powder.

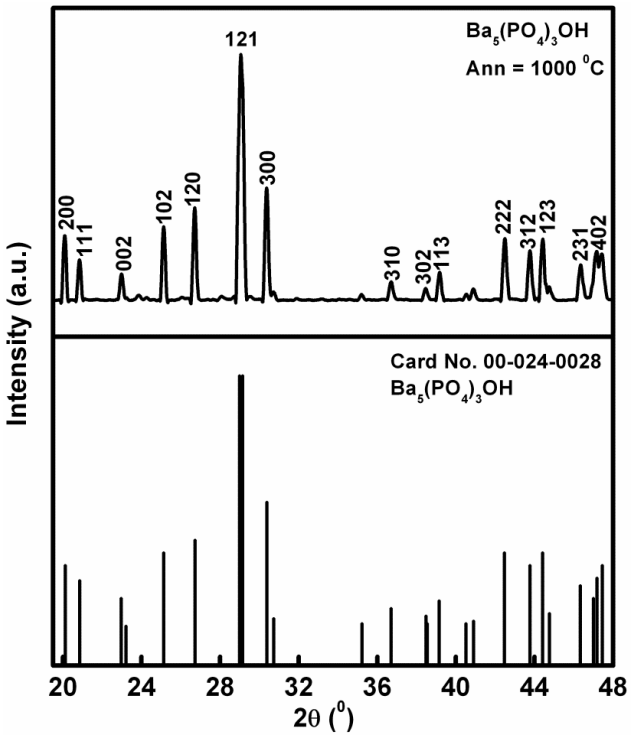

Figure 4.1 XRD pattern and crystal structure of $Ba_5(PO_4)_3OH$ powder.

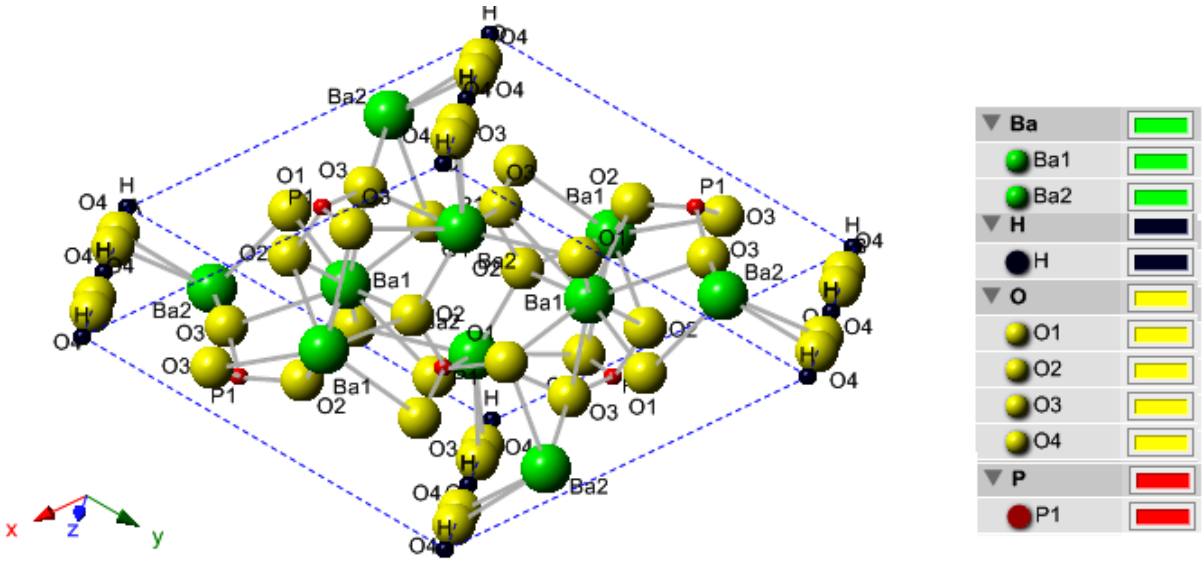

Figure 4.2 Crystalline structure of $Ba_5(PO_4)_3OH$ powder.

Table 4.1. Crystallographic data for $Ba_5(PO_4)_3OH$ lattice

Phase	**$Ba_5(PO_4)_3OH$**
Empirical formula	$Ba_5P_3O_{13}H_1$
Structure	Hexagonal
Space group	$P6_3$ (173)
Formula weight	988.5564 g/mol
Cell ratio	a/b = 1.000 b/c=1.3198 c/a=0.7577
Lattice parameter	
a (Å)	10.190
c (Å)	7.721

Table 4.2. Atomic parameters

Atom	**Ox**	**Wyck**	**Site**	**x/a**	**y/b**	**z/c**
Ba1	2	6c	1	0.7393	-0.01890	0.255
Ba2	2	2b	3	1/3	2/3	0
P1	5	6c	1	-0.0322	0.3699	0.256
O1	-2	6c	1	0.576	0.118	0.24
O2	-2	6c	1	0.260	0.331	0.908
O3	-2	6c	1	0.089	0.728	0.593
O4	-2	6c	1	0.343	0.859	0.25

4.3.2 Particle morphology and chemical composition analysis

Figure 4.3 (a) shows the SEM image of $Ba_5(PO_4)_3OH$ powder. The particles are agglomerated together forming ellipsoidal shape. The agglomeration is attributed to foaming action from the combustion method [13]. Figure 4.4 (b) shows the high magnification image of the encircled area in figure 4.3 (a). The ellipsoidal shape is formed by small agglomerated particles. Figure 4.3 (c) show the EDS spectrum pattern of $Ba_5(PO_4)_3OH$ powder. The EDS is used to identify and quantify the elemental composition of sample area as small as nanometers. The intense peaks of Ba, P, and O were observed confirming the formation of $Ba_5(PO_4)_3OH$. The impurity C (carbon) is due to carbon tape used to mount the sample. The bar graph in the top right corner shows the weight percentage of the elements. The weight percentage of Ba, P, and O were 62, 10 and 28%, respectively. Figure 4.3 (d) show the elemental mapping of $Ba_5(PO_4)_3OH$ powder. Mapping indicates that the elements (Ba, P, O and C) are evenly distributed on the surface. Table 4.3 shows the elemental composition, corresponding X-rays and quantitative percentage of each element in $Ba_5(PO_4)_3OH$ powder. Ba, P, and O peaks are located in the range from 4.0-5.8 eV, 2.0 and 0.5 eV corresponding to Lα, Kα and Kα, respectively. The weight percentage or concentration of Ba is greater than of P and O, confirming that heavy atoms are stronger than lighter atoms. Figure 4.3 (e) and (f) show the particle size distribution of $Ba_5(PO_4)_3OH$ powder which is taken from statistics analysis by measuring approximately 10 particles. The average particles length and width are 867 and 169 nm, respectively.

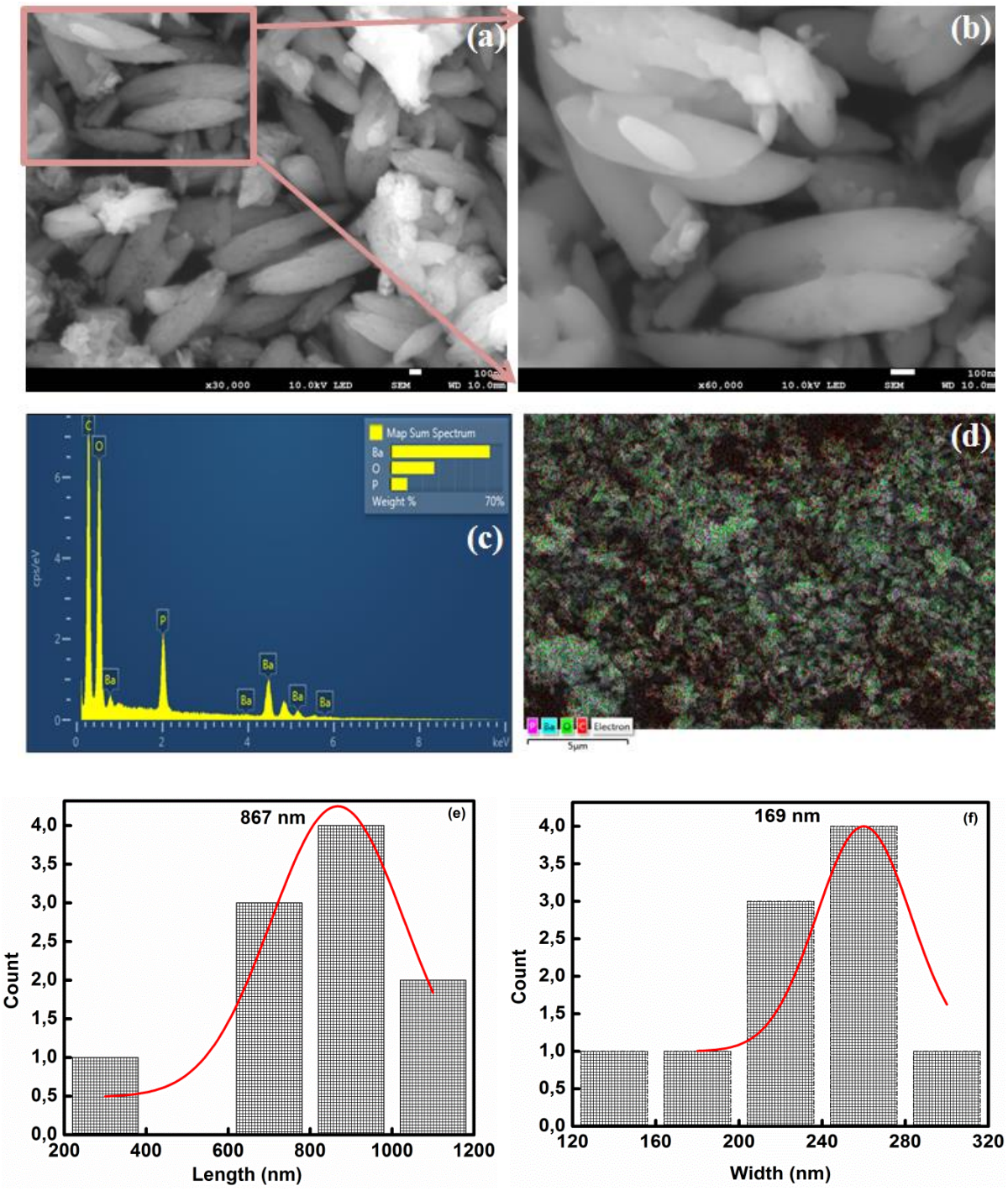

Figure 4.3 (a) – (b) SEM image, (c) EDS analysis, (d) elemental mapping, (e) and (f) particle size distribution of $Ba_5(PO_4)_3OH$ powder.

Table 4.3. Elemental composition of $Ba_5(PO_4)_3OH$ powder

Elements	Position (eV)	Characteristic X-rays shells	Wt %
Ba	**4.0-5.8**	**Lα**	**62**
P	**2.0**	**Kα**	**10**
O	**0.5**	**Kα**	**28**

4.3.4 UV-Vis diffuse reflectance spectra and Bandgap analysis

Diffuse reflection spectra of different phosphate phosphors in the range from 200 to 1100 nm are shown in Figure 4.4. Figure 4.4 (a) (i) show the absorption bands at 245 and 318 nm attributed to intrinsic transition (band- to-band and crystal defects) of host lattice [14, 15]. The absorption peaks at 380, 525, and 657 nm in figure 4.4 (a) (ii) are attributed to 4*f*-4*f* transitions of Er^{3+} ion from the ground state $^4I_{15/2}$ to $^2G_{11/2}$, $^2H_{11/2}$ and $^4F_{9/2}$ states respectively [16-18]. Figure 4.4 (iii) shows the absorption peaks at 227 and 318 nm attributed to host lattice and an extra peak at 980 nm attributed to Yb^{3+} transitions from the ground state $^2F_{7/2}$ to excited state $^2F_{5/2}$ [19]. Upon co-doping with 15 mol % of Yb^{3+}, a similar trend of peaks is observed. The host absorption peak is observed at 227 nm attributed to interband transition of $Ba_5(PO_4)_3OH$. Er^{3+} absorption peaks are observed at 380, 524, and 655 nm and Yb^{3+} absorption peak is observed at 980 nm attributed 4*f*-4*f* transitions of Er^{3+} and Yb^{3+} ions as mentioned above. Data plot of absorption versus energy in the absorption edge region is shown in figure 4.5 (b), which is obtained from the corresponding diffuse reflection spectrum by using Kubelka-Munk function:

$$F(R) = \frac{(1-R)^2}{2R} = \frac{K}{S} \tag{4.3}$$

where *K, S,* and *R* are the absorption, scattering and reflection coefficients, respectively [20]. By extrapolating the K-M function to K/S = 0, the bandgap energies of $Ba_5(PO_4)_3OH$, $Ba_5(PO_4)_3OH:Er^{3+}$, $Ba_5(PO_4)_3OH:Yb^{3+}$ and $Ba_5(PO_4)_3OH:Er^{3+},Yb^{3+}$ were estimated to be 3.7, 5.6, 4.5 and 4.9 eV respectively. Unfortunately, there are no available theoretical band gaps of $Ba_5(PO_4)_3OH$ to be compared [21]. The band gap energy calculated is comparable to the bandgap energy of $Ba_3In_2P_4O_{16}$ reported by Zhang et al [22]. The increase in bandgap (blue

shift) is due to electrons filling or moving to a high energy state. The excess electrons cause an enlargement of the bandgap and the process is known as Burstein-Moss effect [23].

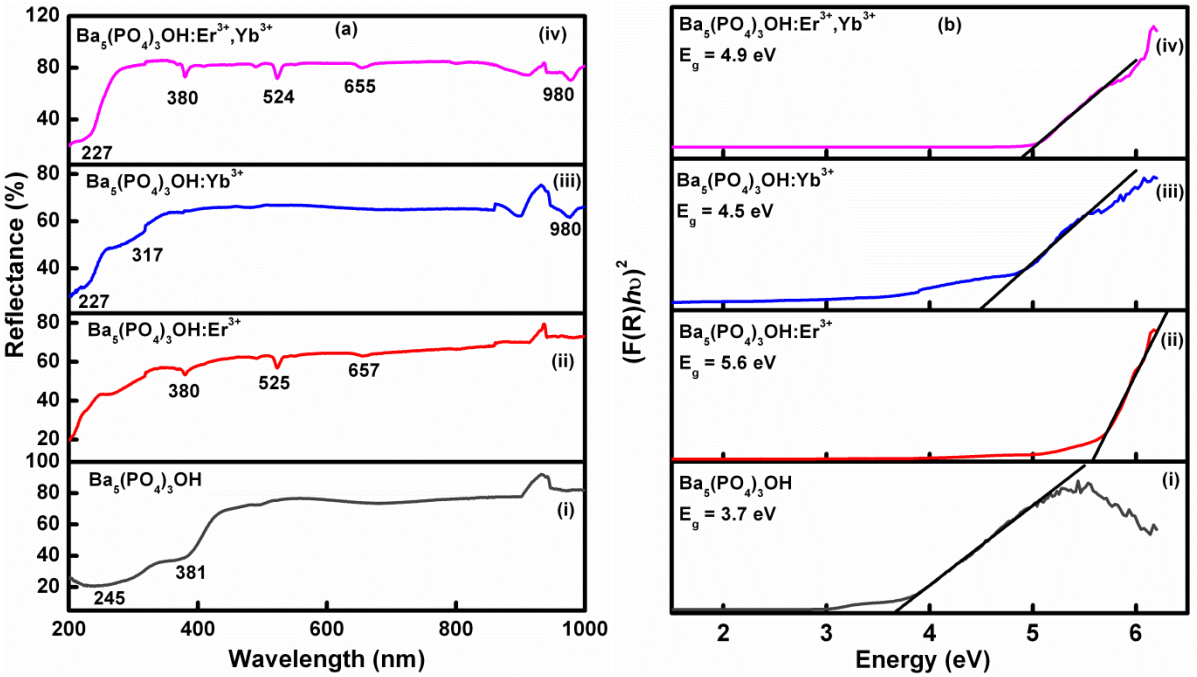

Figure 4.4 (a) Reflectance and (b) bandgap energy spectra of (i) $Ba_5(PO_4)_3OH$, (ii) $Ba_5(PO_4)_3OH:Er^{3+}$ and (iii) $Ba_5(PO_4)_3OH:Yb^{3+}$ and (iv) $Ba_5(PO_4)_3OH:Er^{3+},Yb^{3+}$ phosphor powders.

4.3.5. Photoluminescence properties of Er^{3+}/Yb^{3+} co-doped $Ba_5(PO_4)_3OH$ phosphor powder.

Figure 4.5 (a) shows the up-conversion (UC) PL emission spectrum of $Ba_5(PO_4)_3OH:Er^{3+}$ powder recorded at room temperature from the range of 400 – 700 nm when the powder was pumped using the 980 nm laser. The samples exhibited multiple emission peaks at 549 and 560 nm in the green region corresponding to $^4S_{3/2} \rightarrow {}^4I_{15/2}$ and another peaks at 662 and 680 nm in the red region that are corresponding to $^4F_{9/2} \rightarrow {}^4I_{15/2}$ transition of Er^{3+} [24 - 27]. Figure 4.5 (b) shows the up-conversion PL emission spectrum of $Ba_5(PO_4)_3OH:Yb^{3+}$ recorded upon 980 nm pump laser. The emission peaks are observed at 475, 648, and 660 nm assigned to transitions of Yb^{3+} ion.

Upon addition of Yb^{3+}, red emission peak at 658 nm and minor peaks at 676 and 682 nm are enhanced due to energy transfer process between Er^{3+} and Yb^{3+}. The enhanced red emissions at 658, 676, and 682 nm observed from Er^{3+}-Yb^{3+} co-doped phosphor and are attributed to $^4F_{9/2} \rightarrow {}^4I_{15/2}$ transitions of Er^{3+} as shown in figure 4.5 (c). Yb^{3+} makes a significant contribution to the upconversion emissions by acting as a sensitizer which strongly absorbs

the primary excitation energy and then transfers it to Er^{3+} [28]. The energy of 980 nm laser matches well with the level spacing of $^4I_{15/2} \rightarrow {}^4I_{11/2}$ of Er^{3+} ion and $^2F_{7/2} \rightarrow {}^2F_{5/2}$ of Yb^{3+} ion, but Yb^{3+} has higher excitation cross section which induces Yb^{3+} ion to act as a sensitizer to Er^{3+} ion [29].

Er^{3+} and Yb^{3+} are excited from the ground state $^4I_{15/2}$, $^2F_{5/2}$ level to the excited levels $^4I_{11/2}$ and $^2F_{5/2}$, respectively when phosphors are pumped with 980 nm laser. The Yb^{3+}: $^2F_{5/2}$ state becomes highly populated and metastable. Amount of ion in Yb^{3+}:$^2F_{5/2}$ level transfer energy to Er^{3+}:$^4I_{11/2}$, $^4I_{13/2}$ level via the efficient energy transfer process due to the small energy gaps among them [30]. The energy transfer rate of Yb^{3+}:$^2F_{5/2} \rightarrow Er^{3+}$:$^4I_{11/2}$ is demonstrated to be larger than that of Yb^{3+}:$^2F_{5/2} \rightarrow Er^{3+}$:$^4I_{13/2}$ because of the mismatch of Yb^{3+}:$^2F_{5/2} \rightarrow Er^{3+}$:$^4I_{13/2}$ is large [31]. The excited Yb^{3+} ions transfer their energy to Er^{3+} ions in the $^4I_{15/2}$ ground state, and excite them to $^4I_{11/2}$ state. Faster energy transfer from the second excited Yb^{3+} ion or direct absorption of the photon at 980 nm can further excites Er^{3+} ion from $^4I_{11/2}$ state to the $^4F_{7/2}$ level. After nonradiative relaxation from the $^4F_{7/2}$ level to the $^2H_{11/2}$ or $^4S_{3/2}$ level, the Er^{3+} return to the ground state introducing the green emission ($^2H_{11/2}$ + $^4S_{3/2} \rightarrow {}^4I_{15/2}$) and further nonradiatively relax to the $^4F_{9/2}$ level, leading to red emission ($^4F_{9/2} \rightarrow {}^4I_{15/2}$). Thus energy transfer from Yb^{3+} to Er^{3+} is illustrated in figure 4.5 (d).

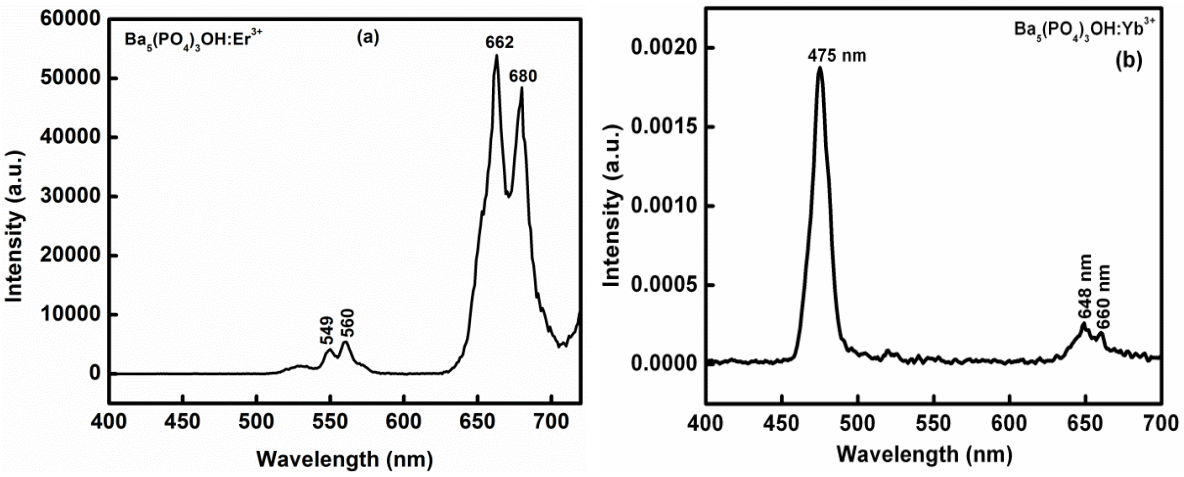

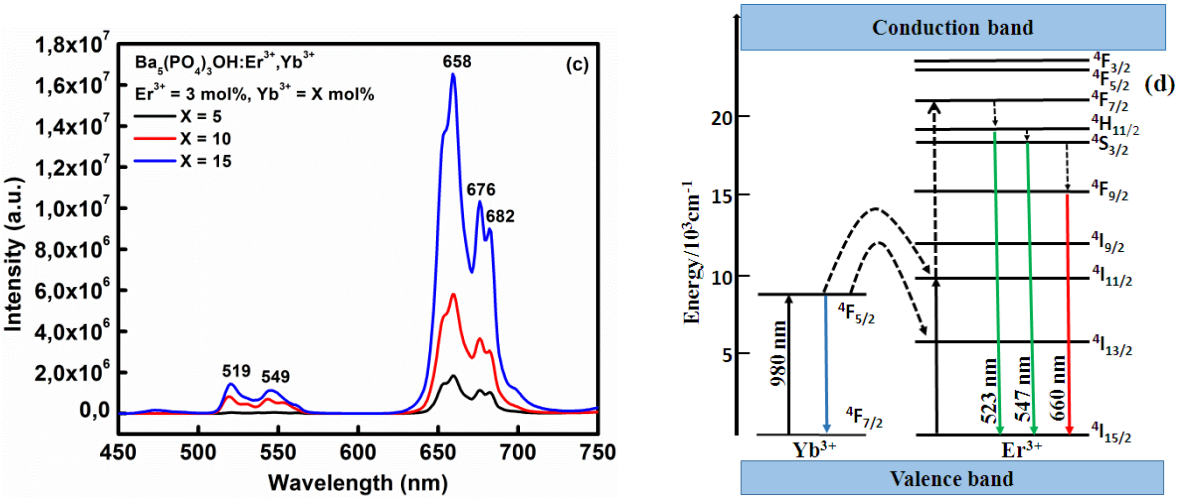

Figure 4.5. Upconversion emission spectra of (a) 0.5 mol% and 1 mol% Er^{3+} doped $Ba_5(PO_4)_3OH$, (b) $Ba_5(PO_4)_3OH:Yb^{3+}$, (c) $Ba_5(PO_4)_3OH:Er^{3+},Yb^{3+}$ phosphor powders and (d) energy transfer mechanism of Er^{3+} and Yb^{3+}.

4.4 Conclusion

In conclusion, $Ba_5(PO_4)_3OH:Er^{3+}/Yb^{3+}$ phosphor powders were synthesized by urea combustion method. The pure phase of the $Ba_5(PO_4)_3OH$ shows that it the powder is crystalline. The particles are agglomerated together and this is attributed to foaming action from the combustion method. The intense peaks of Ba, P, and O were observed confirming the formation of $Ba_5(PO_4)_3OH$. Under 980 nm excitation, $Ba_5(PO_4)_3OH:Er^{3+}$ phosphors exhibited green and red upconversion luminescence assigned to Er^{3+} transitions. $Ba_5(PO_4)_3OH:Yb^{3+}$ gives emission at 475, 648, and 660 nm assigned to transitions of Yb^{3+} ion. Upon co-doping with Yb^{3+}, red emission is enhanced; this is attributed to energy transfer process between Er^{3+} and Yb^{3+}.

References

[1] A. Boukhris, B. Gloriex, M. B. Amara, Journal of Molecular Structure, 2015, 1083, 319-329

[2] H. Taghrir, M. Ghashang, M. N. Biregan, Chinese Chemical Letters, 2016, 27, 119-126

[3] T. Hadi, G. Majid, N.B. Mohammad, Chinese Chemical Letters, 2016, 27, 119-126

[4] Y. Liang, P. Chui, X. Sun, Y. Zhao, F. Cheng, K. Sun, Journal of Alloys and Compounds, 2013, 552, 289-293

[5] U.F. Alejandra, L.L. Tzarara, J. Oliva, P. Salas, T.C. Alenjandro, E. De laRosa, Journal of luminescence, 2016, 172, 154-160

[6] C.J. Duan, X.Y. Wu, W.Liu, H.H. Chen, X.X. Yang, J.T. Zhao, Journal of Alloys and Compounds, 2005, 396, 86-1

[7] S. Hraiech, M. Ferid, Y. Guyot, G. Boulon, Journal of rare earths, 2013, 31, 685-693

[8] S.S. Das, N.P. Singh, P.K. Srivastava, Progress in Crystal Growth and Characterization of Materials, 2009, 55, 47-62

[9] S. Hraiech, M. Ferid, Y Guyot, G. Boulon, Journal of Rare Earths, 2013, 31, 685-6932

[10] K. Souiwa, M. Hidouri, O. Toulemonde, M. Duttine, M.B. Amara, Journal of Alloys and Compounds, 2015, 627, 153-160

[11] S. Sumathi, G. Buvaneswari, Ceramics International, 2012, 38, 3547-3552

[12] K. van Dijk, H.G. Schaeken, C.H.M. Maree, J. Verhoeven, J.C.G. Wolke, F.H.P.M. Habraken, J.A. Jansen, Surface and Coatings Technology, 1995, 76-77, 206-210

[13] C. Zhang, X. Zhang, C. Liu, K. Sun, J. Yuan, Ceramics International, 2016, 42, 279-285

[14] Z. Zhang, L. Liu, S. Song, J. Zhang, D Wang, Current Applied Physics, 2015, 15, 248-252

[15] J. Zhang, J. Jia, Z. Hua, Materials and Design, 2015, 87, 124-129

[16] I. Soltani, S. Hraiech, K. Horchani-Naifer, H. Elhouichet, M. Ferid, Optical Materials, 2015, 46, 454-460

[17] G. Li, C. Zhang, P. Song, P Zhu, K. Zhu, J. He, Journal of Alloys and Compounds, 2016, 662, 89-93

[18] L. Wu, B. Huang, F. Yang, Y. Qi, S. Peng, Y. Zhou, J. Li, Optical Materials, 2015, 43, 42-48

[19] Y. Qi, Y. Zhou, L. Wu, F. Yang, S. Peng, S. Zheng, D. Yin, Journal of luminescence, 2014, 153, 401-407

[20] J. Zhang, Z. Hua, S. Wen, Journal of alloys and Compounds, 2015, 637, 70-76

[21] J. Zhang, Y. Duan, L. Da, R. Li, Journal of Alloys and Compounds, 2016, 680, 121-128

[22] W.L. Zhang, G.L. Chai, H. Zhang, C.S. Lin, C.Z. He, W.D. Cheng, Materials Research Bulletin, 2010, 45, 1796-1802

[23] M. Daoudi, F. Hosni, N. Khalifa, I. Dhifallah, K. Farah, A.H. Hamzaoui, Physica B, 2014, 440, 113-117

[24] R.V. Perrella, M.A. Schiavon, E. Peceraro, S.J.L. Ribeiro, J.L. Ferrari, Journal of Luminescence, 2016, 178, 226-233

[25] C.R. Kesavulu, H.J. Kim, S.W. Lee, J. Kaewkhao, N. Wantana, S. Kothan, Journal of Alloys and Compounds, 2016, 683, 590-598

[26] G. Tang, X. Wen, Q. Qian, T. Zhu, W. Liu, M. Sun, X. Chen, Z. Yang, Journal of Alloys and Compounds, 2016, 664, 19-24

[27] Alejandra U.F., Tzarara L.L., Oliva J., Salas P, Alejandro T.C., De la Rosa E., Journal of Luminescence, 2016, 172, 154-160

[28] Cao B.S., He Y.Y., Zhang L., Dong B., Journal of Luminescence, 2013, 135,128-132

[29] X.Q. Guo, Y. Yan, H.C. Zhang, Y. Han, J.J. Song, Ceramics International, 2016, 42, 8738-8743

[30] X. Shan, G. Tang, X. Chen, S. Peng, W. Liu, Q. Qian, D. Chen, Z. Yang, Journal of Rare Earths, 2016, 34, 868-875

[31] C. Wang, H. Xia, Z. Feng, Z. Zhang, D. Jiang, X. Gu, Y. Zhang, B. Chen, H. Jiang, Journal of Alloys and Compounds, 2016, 686, 816-820

Chapter 5

Upconversion luminescence properties of Eu^{3+}/Yb^{3+} co-doped $Ba_5(PO_4)_3OH$ phosphor powders

5.1. Introduction

Different types of phosphates are promising for the creation of efficient phosphors due to their properties such as, low toxicity, and thermal and chemical stability [1, 2]. Rare earth doped phosphate phosphors are of scientific and technological interest due to their structural and optical behavior which gives them wide range of applications in medical and biological labels, solar cells, colorful display, and light sources [3, 4]. Despite the wide range of applications, the use of alkaline phosphates such as barium, calcium and strontium phosphates has not been receiving much attention in organic synthesis for biomedical applications. Barium orthophosphate ($Ba_3(PO_4)_2$) has a high capacity for substitution of Ba^{2+} ions by other cations and anions. $Ba_3(PO_4)_2$ is used as a host for rare earth doped luminescent materials such as europium (Eu^{3+}) and ytterbium (Yb^{3+}) [5]. Eu^{3+} has strong absorption intensity in the ultraviolet-blue region and is an ideal red emitting activator [6, 7]. Eu^{3+} doped in most matrices exhibit red narrow band emission in various crystal lattices due to $4f \rightarrow 4f$ transitions [8]. It has been widely used to fabricate luminescent nanoparticles for biomedical applications [9]. Yb^{3+} shows a broad absorption band in the range of 850-1100 nm due to $4f \rightarrow 4f$ transitions. The $4f$ electrons from Yb^{3+} are less shielded than in other rare earth ions, they show a greater tendency to interact with the surrounding ions [10]. When excited at the lower energies such as in near infrared, it transfers its excited energy to the activator. The process in which Yb^{3+} absorbs low energies and sequentially transfers it to other ions is known as energy transfer up-conversion (ETU) [11].

$Ba_5(PO_4)_3OH$ co-doped with Eu^{3+} and Yb^{3+} phosphor were prepared by urea combustion method. The XRD analysis, morphology and upconversion emission studies have been analysed. The process responsible for upconversion emission and energy transfer from Yb^{3+} to Eu^{3+} is discussed in details.

5.2. Experimental

5.2.1 Preparation of phosphor powders

$Ba_5(PO_4)_3OH$ co-doped Eu^{3+}/Yb^{3+} phosphor powders were synthesized by combustion method using urea as a fuel. The following starting materials with 99% purity were used for the preparation of materials reported in this paper: strontium nitrate (6M $Ba(NO_3)_2{\cdot}4H_2O$), di-ammonium hydrogen phosphate ((4M $NH_4)_2HPO_4$), europium nitrate ($Eu(NO_3)_3{\cdot}5H_2O$), ytterbium nitrate ($Yb(NO_3)_3{\cdot}6H_2O$) with different concentrations of Eu^{3+} (0.1 - 7 mol %), Yb^{3+} (7 mol %), and Eu^{3+}:Yb^{3+} (3:7 mol %), and urea ($CO(NH_4)_2$). When a complete reaction is assumed, the theoretical equation for the formation of $Ba_5(PO_4)_3OH$ is given by:

$$15Ba(NO_3)_2{\cdot}4H_2O + 9(NH_4)_2HPO_4 + 16CH_4N_2O = 3Ba_5(PO_4)_3OH + 16CO_2 + 131H_2O + 40N_2 \quad (5.1)$$

All reagents, in stoichiometric amounts, were dissolved in 2 ml of distilled water and the mixture was stirred vigorously for 15 min in room temperature until a thick homogenous solution was formed. The solution was kept in a furnace for 10 minutes maintained at 600 °C. The solution boiled, underwent dehydration and decomposed while generating combustible gases such as CO_2, N_2 and H_2O. The combustion ashes were cooled to room temperature and were ground gently using a pestle and mortar resulting in a fine powder. The materials synthesized were $Ba_5(PO_4)_3OH$, $Ba_5(PO_4)_3OH:Eu^{3+}$, $Ba_5(PO_4)_3OH:Yb^{3+}$ and $Ba_5(PO_4)_3OH:Eu^{3+},Yb^{3+}$. All the powders were annealed at 800 °C in air for 2 hours.

The materials synthesized were $Ba_5(PO_4)_3OH$, $Ba_5(PO_4)_3OH:Eu^{3+}$, $Ba_5(PO_4)_3OH:Yb^{3+}$ and $Ba_5(PO_4)_3OH:Eu^{3+},Yb^{3+}$ phosphor powders with different concentrations of Eu^{3+} in the range from 0.1 -7 mol%, Yb^{3+} (7mol %), and Eu^{3+}:Yb^{3+} (3:7 mol%).

5.2.2 Measurements

The structure and crystallinity of the phosphors were analysed using a Bruker AXS D8 X-ray Diffraction (XRD) with Cu Kα1 radiation (λ = 1.5406Å) in the range from 20 to 50°. Particle morphology were examined using Jeol JSM-7800F thermal field emission SEM coupled with Oxford Aztec 350 X-Max80 EDS, that was used to analyse the chemical composition of the phosphors under typical vacuum of 9.634×10^{-5} Pa. The absorption and bandgap energy were evaluated using Perkin Elmer Lambda 950 UV-Vis spectrometry. The photoluminescence data were recorded using Cary eclipse fluorescence with monochromatized xenon lamp and upconversion emissions were measured by using Edinburgh Instruments FLS980

Fluorescence Spectrometer with 980 nm NIR laser as the excitation source and photomultiplier (PMT) detector.

5.3. Results and Discussion

5.3.1 Phase analysis

The crystal structure and phase composition of the $Ba_5(PO_4)_3OH$ powder was analysed using Cu-Kα radiation XRD. Figure 5.1 shows XRD pattern of $Ba_5(PO_4)_3OH$ powder. The diffraction peaks of $Ba_5(PO_4)_3OH$ were well indexed to the pure hexagonal phase, referenced by ICDD Card Number 00-024-0028. The peaks are sharp, indicating that powder is crystalline and no impurities were detected from the XRD pattern. The crystallite size of the powder was determined using the Debye-Scherrer equation. The average crystallite size estimated was 40±2 nm.

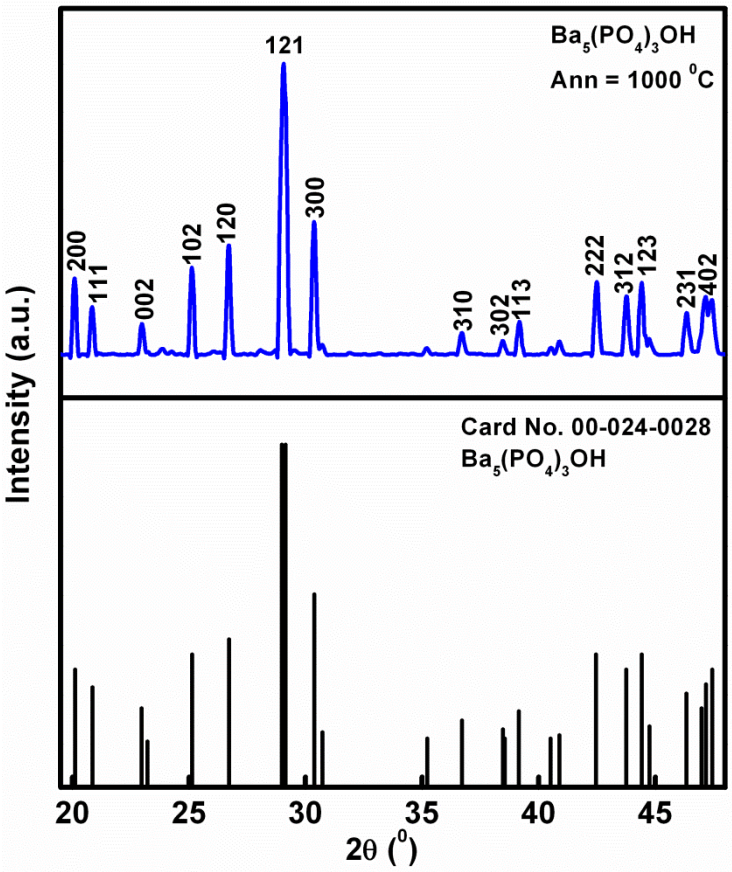

Figure 5.1 XRD pattern and crystal structure of $Ba_5(PO_4)_3OH$ powder

5.3.2 Particle morphology and chemical composition analysis

Figure 5.2 shows the SEM images of (a-e) $Ba_5(PO_4)_3OH$, (b-f) $Ba_5(PO_4)_3OH:Eu^{3+}$, (c-g) $Ba_5(PO_4)_3OH:Yb^{3+}$, (d-h) $Ba_5(PO_4)_3OH:Eu^{3+},Yb^{3+}$ phosphor powders for as-prepared and annealed (at 800 ^{0}C) samples respectively. Figure 5.2 (a) shows the rod-like morphology of $Ba_5(PO_4)_3OH$ forming flowers like structure, and upon doping with Eu^{3+} and Yb^{3+} (Figure 5.2 (b), (c) and (d)) the morphology shows spherical, needle-like, and non-uniform. The images show a change in surface morphology and particle size which is due to addition of dopants and annealing, respectively. The particles possess are highly agglomerated, which is attributed to foaming action from the combustion method [25]. The size of the particles appears to be larger/bigger when comparing between as-prepared and annealed powder phosphors. This could be due to the annealing effect.

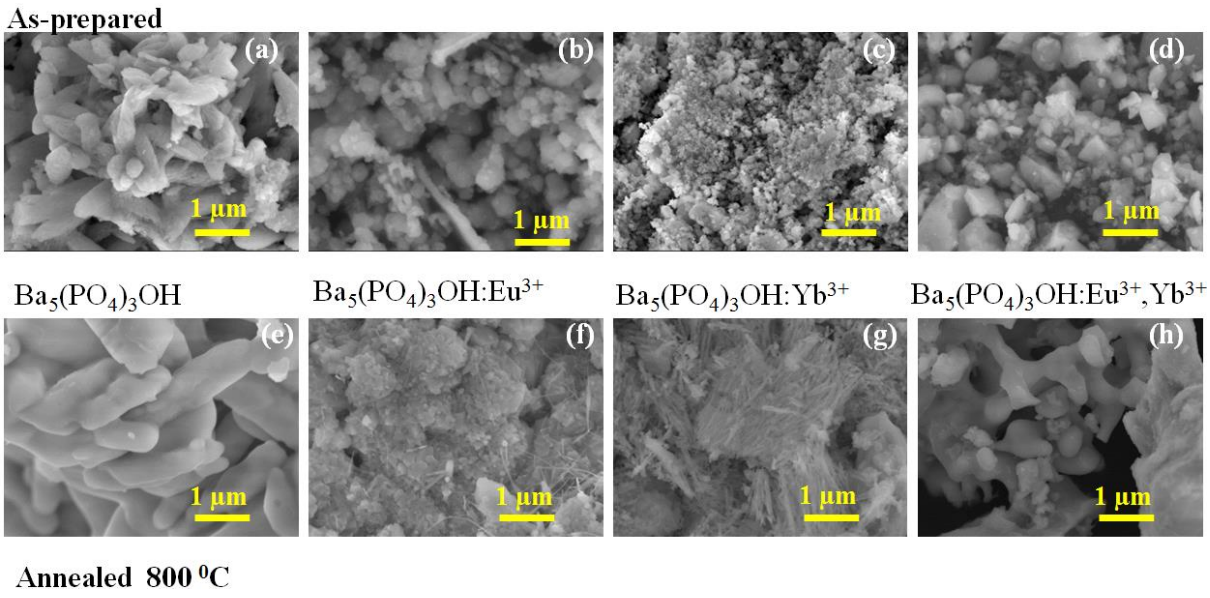

Figure 5.2. shows the SEM images of (a-e) $Ba_5(PO_4)_3OH$, (b-f) $Ba_5(PO_4)_3OH:Eu^{3+}$, (c-g) $Ba_5(PO_4)_3OH:Yb^{3+}$, (d-h) $Ba_5(PO_4)_3OH:Eu^{3+},Yb^{3+}$ phosphor powders for as-prepared and annealed (at 800 ^{0}C) respectively.

The $Ba_5(PO_4)_3OH$ powder phosphor was further analyzed using EDS to obtain the chemical composition as shown in Figure 5.3. The intense peaks of Ba, P, and O were observed confirming the formation of $Ba_5(PO_4)_3OH$. The insert shows the distribution of each element on the surface, which shows that the elements are evenly distributed on the surface. The bar graph shows the weight % of each element at that area with Ba, O and P estimated to be 70, 18 and 12 % respectively.

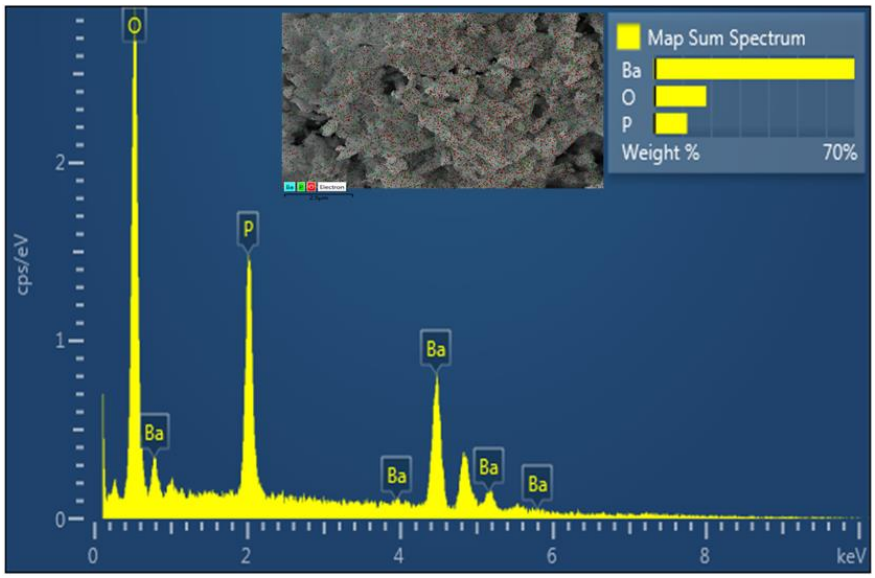

Figure 5.3 shows the EDS spectrum and mapping of $Ba_5(PO_4)_3OH$ powder.

5.3.3 UV-Vis diffuse reflectance spectra and Bandgap analysis

Diffuse reflection spectra of different phosphate phosphors ranging from 200 to 1000 nm are shown in Figure 5.4. Figure 5.4 (a) shows the absorption peaks for ($Ba_5(PO_4)_3OH$) host and different rare earths ions (Eu^{3+} and Yb^{3+}). The absorption peaks in the range of 200-385 nm are attributed to band-to-band transitions of the host lattice and crystal defects [12, 18]. The other peak at 395 nm in the $Ba_5(PO_4)_3OH:Eu^{3+}$ system is due to 4*f*-4*f* transitions of Eu^{3+} ion [26]. An additional peak observed at 977 nm for $Ba_5(PO_4)_3OH:Yb^{3+}$ and $Ba_5(PO_4)_3OH:Eu^{3+},Yb^{3+}$ phosphors is assigned to Yb^{3+} transitions from the ground state $^2F_{7/2}$ to excited state $^2F_{5/2}$ [27, 28]. The hump observed at 930 nm on all the spectrums is due to the system fluctuation. Data plot of absorption versus energy in the absorption edge region is shown in figure 5.4 (b), which is obtained from the corresponding diffuse reflectance spectrum by using Kubelka-Munk function. By extrapolating the K-M function to K/S = 0, the bandgap energies of $Ba_5(PO_4)_3OH$, $Ba_5(PO_4)_3OH:Yb^{3+}$, $Ba_5(PO_4)_3OH:Eu^{3+}$, and $Ba_5(PO_4)_3OH:Eu^{3+},Yb^{3+}$ were estimated to be 3.7, 4.9, 3.9 and 4.7 eV respectively.

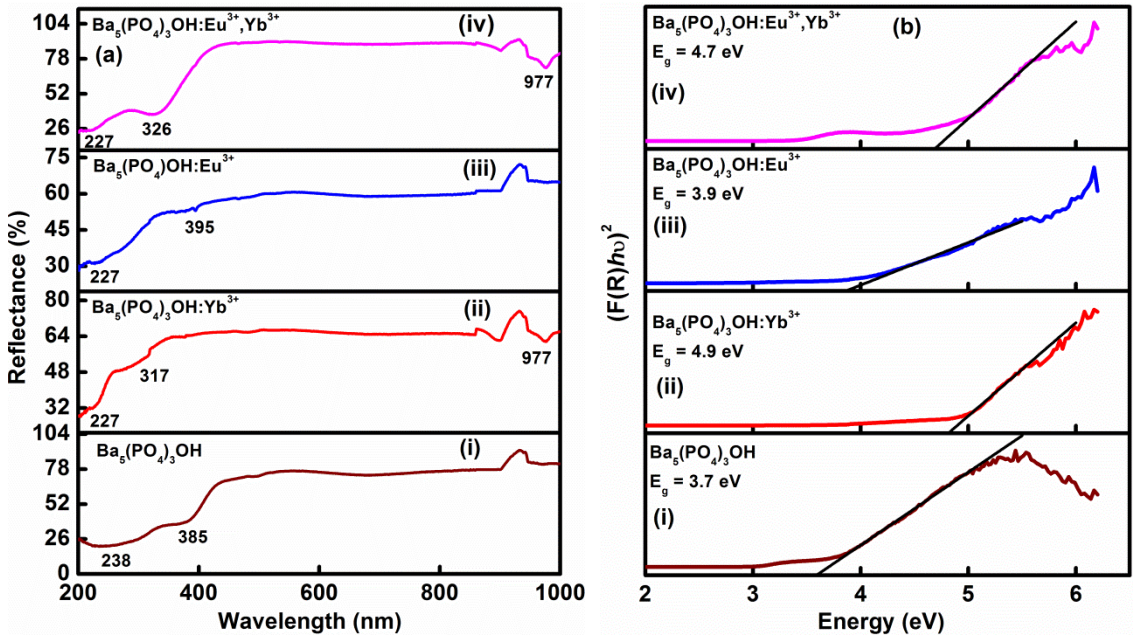

Figure 5.4 (a) Reflectance spectra of $Ba_5(PO_4)_3OH$, and $Ba_5(PO_4)^3OH$ with different rare earths (Yb^{3+}, Eu^{3+} and Eu^{3+}:Yb^{3+}) and (b) bandgap energies of all phosphor powders.

5.3.4 Photoluminescence properties of Eu^{3+}/Yb^{3+} co-doped $Ba_5(PO_4)_3OH$ phosphor powder.

Figure 5.5 (a) show the PL excitation and emission of $Ba_5(PO_4)_3OH:Eu^{3+}$ phosphor. The excitation peaks are observed at different wavelengths ranging from 240-537 nm. The broad intense excitation peak at 240 nm is attributed to O^{2-}-Eu^{3+} charge transfer band [29]. The other excitation peaks located at ~319, 360, 382, 395 and 465-537 nm are assigned to $^7F_0 \rightarrow$ ($^5H_6$, $^5D_4$, $^5L_8$, $^5L_7$, and $^5D_{j\ (j\ =1,2)}$) transitions of Eu^{3+} ion [30]. The emission peaks are observed at ~589, 614, 651 and 699 nm attributed to $^5D_0 \rightarrow {}^7F_1$, $^5D_0 \rightarrow {}^7F_2$, $^5D_0 \rightarrow {}^7F_3$ and $^5D_0 \rightarrow {}^7F_4$ transitions of Eu^{3+} ion respectively [31, 32]. The inset shows that the intensity increases with the concentration of Eu^{3+} from 0.1 mol.% to 3 mol.%, and at higher concentrations of 5 and 7 mol.% the intensity decreases due to concentration quenching of Eu^{3+}.

Figure 5.5 (b) shows the emission spectrum of $Ba_5(PO_4)_3OH:Yb^{3+}$ upon 980 nm laser excitation. The intense blue emission peak at 475 nm and other minor peaks at 648 and 660 nm are observed and attributed to $^2F_{7/2} \rightarrow {}^2F_{5/2}$ transitions of Yb^{3+} ion [10].

Figure 5.5 (c) shows the emission spectrum of $Ba_5(PO_4)_3OH:Eu^{3+},Yb^{3+}$ phosphor upon 980 nm laser excitation. Upconversion emission is not observed in the $Ba_5(PO_4)_3OH:Eu^{3+}$ system, because singly Eu^{3+} doped materials cannot absorb 980 nm photons, due to

unavailability of energy levels in the Eu^{3+} ions [29]. Upon co-doping with Yb^{3+}, the upconversion emission is observed. This indicates that the Eu^{3+} ions are excited due to the presence of o Yb^{3+} ions. The emission peaks observed at ~523, 588, 613, 657 and 704 nm are attributed to $^5D_0 \rightarrow {}^7F_{j\ (j=1,2,3,4)}$ transitions of Eu^{3+} ion in the $Ba_5(PO_4)_3OH:Eu^{3+},Yb^{3+}$ system. The strongest emission peak is observed at 657 nm assigned to $^5D_0 \rightarrow {}^7F_3$ transition of Eu^{3+} ion. This is due to energy transfer upconversion from Yb^{3+} to Eu^{3+}. Yb^{3+} act as a sensitizer for Eu^{3+} via cooperative energy transfer process.

The energy transfer upconversion process involves de-excitation of two Yb^{3+} ions and excitation of Eu^{3+} ion. The energy transfer upconversion excitation mechanism is accomplished through dipole-dipole interaction involving pairs of excited Yb^{3+} ions at the excited state and Eu^{3+} ion at the $^7F_0$ ground state. The Yb^{3+} ion from its $^2F_{7/2}$ ground state gets excited to the $^2F_{5/2}$ state, and then transfers their energy in a way that after the acceptor has gained energy from the donor it occupies the virtual state (V). After that the excited Yb^{3+} ions from its virtual state transfer their excitation energy directly to the $^7F_0$ ground state of Eu^{3+} ions promoting them to the $^5D_1$ and $^5D_0$ level of Eu^{3+} ions and demoting the Yb^{3+} ions to the $^2F_{7/2}$ ground state. Then, relaxation from $^5D_0$ states gives radiative emission at 523, 588, 613, 657 and 704 nm corresponding to $^5D_0 \rightarrow {}^7F_{j\ (j=1,2,3,4)}$ transitions. The energy transfer mechanism is shown by figure 5.6 (d) and well explained by *James R. Silva et al, and Anurag Pandey et al* [29, 33].

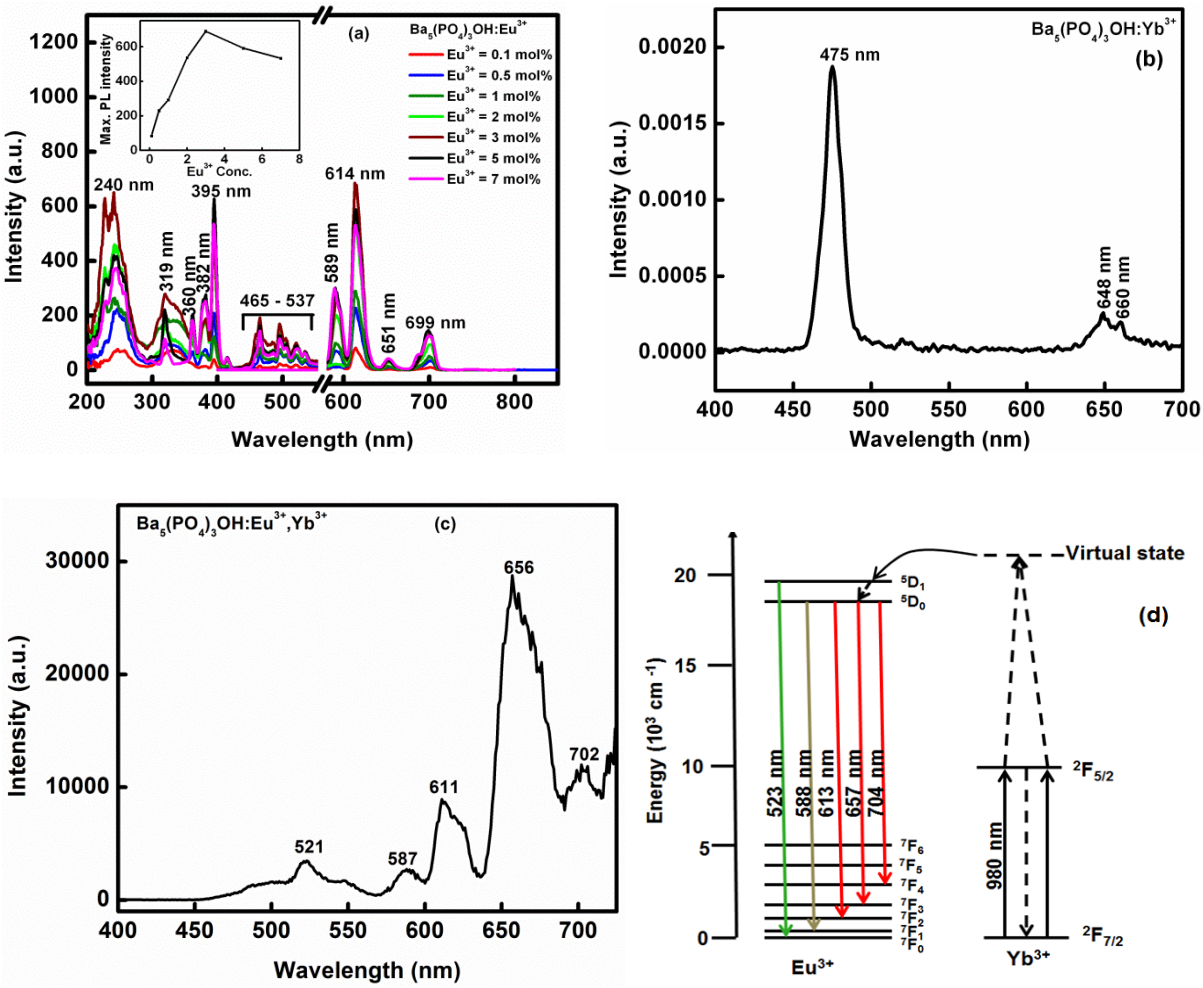

Figure 5.5 Luminescence spectra of (a) $Ba_5(PO_4)_3OH:Eu^{3+}$, (b) $Ba_5(PO_4)_3OH:Yb^{3+}$ and (c) $Ba_5(PO_4)_3OH:Eu^{3+},Yb^{3+}$ phosphor powders and (d) energy transfer mechanism of Yb^{3+} to Eu^{3+}.

5.4. Conclusion

Phosphate powder phosphors were prepared by urea combustion method. The diffraction peaks were well indexed to the pure hexagonal phase referenced by JCPDS Card Number 00-024-0028 matching with $Ba_5(PO_4)_3OH$ system. The SEM images shows a change in surface morphology (from rods to spherical, needle-like, and non-uniform) and particle size which is due to annealing and addition of dopants. The particles were highly agglomerated, due to foaming action from the preparation method. The intense peaks of Ba, P, and O from EDS spectrum were observed confirming the formation of $Ba_5(PO_4)_3OH$ powder. The estimated bandgap energies were 3.7, 4.9, 3.9 and 4.7 eV for $Ba_5(PO_4)_3OH$, $Ba_5(PO_4)_3OH:Yb^{3+}$, $Ba_5(PO_4)_3OH:Eu^{3+}$, and $Ba_5(PO_4)_3OH:Eu^{3+},Yb^{3+}$ respectively. The emission peaks were observed at ~589, 614, 651 and 699 nm corresponding to Eu^{3+} ion transitions. Upon co-doping with Yb^{3+}, 656 nm peak was enhanced due to energy transfer.

References

[1] H. Ji, Z. Huang, Z. Xia, Y. Xie, M. S. Molokeev, V. V. Atuchin, Materials Research Bulletin, 2016, 75, 233-238

[2] A. Boukhris, B. Glorieux, M.B. Amara, Journal of Molecular Structure, 2015, 1083, 319-329

[3] B.A. Sava, M.Elisa, C. Bartha, R. Iordanescu, I. Feraru, C. Plapcianu, R. Patrascu, Ceramics International, 2014, 40, 12387-12395

[4] Y. Tang, R. Mei, S. Yang, H. Tang, W. Yin, Y. Xu, Y. Gao, Superlattices and Microstructures, 2016, 92, 256-263

[5] H. Taghrir, M. Ghashang, M.N. Biregan, Chinese Chemical Letters, 2016, 27, 119-126

[6] H. Wang, S. Ye, S. Li, T. Liu, J. Lin, D. Wang, Journal of Alloys and Compounds, 2015, 648, 13-17

[7] M. Cheng, H. Junhui , Materials Letters, 2012, 70, 101-104

[8] J. Yu, W. Gong, Z. Xiao, G. Ning, Journal of Luminescence, 2012, 132, 2957-2960

[9] S.S. Syamchand, G. Sony, Journal of Luminescence, 2015, 165, 190-215

[10] A. Souamti, I.R. Martin, L. Zayani, M.A. Hernandez-Rodriguez, K. Soler-Carracedo, A.D. Lozano-Gorrin, D.B. Hassen Chehimi, Optical Materials, 2016, 53, 190-194

[11] T. Grzyb, A. Gruszeczka, S. Lis, Journal of Luminescence, 2016, 175, 21-27

[12] S. Hraiech, M. Ferid, Y. Guyot, G. Boulon, Journal of rare earths, 2013, 31, 685-693

[13] S. Sumathi, G. Buvaneswari, Ceramics International, 2012, 38, 3547-3552

[14] Y. Lai, X. Liang, S. Yang, P. Liu, Y. Zeng, C. Hu, Journal of Alloys and Compounds, 2014, 617, 597-601

[15] C. Zhang, et al., Nano-alumina/hydroxyapatite composite powders prepared by in-situ chemical precipitation, Ceramic Internationals (2015), http://dx.doi.org/10.1016/j.ceramint.2015.08.106

[16] S.S. Das, N.P. Singh, P.K. Srivastava, Progress in Crystal Growth and Characterization of Materials, 2009, 55, 47-62

[17] S. Babu, M. Seshadri, V. R. Prasad, Y.C. Ratnakaram, Materials Research Bulletin, 2015, 70, 935-944

[18] K. Meyer, Journal of Non-Crystalline Solids, 1997, 209, 227-239

[19] P.Y. Shih, S.W. Yung, T.S. Chin, Journal of Non-Crystalline Solids, 1999, 244, 211-222

[20] K. Souiwa, M. Hidouri, O. Toulemonde, M. Duttine, M.B. Amara, Journal of Alloys and Compounds, 2015, 627, 153-160

[21] N. Ostrowski, V. Sharma, A. Roy, P.N. Kumta, Journal of Materials Science & Technology, 2015, 31, 437-444

[22] D. Li, C. Liu, L. Jiang, Optical Materials, 2015, 48, 18-24

[23] M. Lu, F. Wang, K. Chen, Y. Dai, Q. Liao, H. Zhu, Spectrochimica Acta Part A: Molecular and Biomolecular Spectroscopy, 2015, 148, 1-6

[24] Y.R. Jiang, F.H. Sun, X.Y. Zhou, W.B. Kong, X.Y. Xie, Chinese Chemical Letters, 2015, 26, 1121-1128

[25] J.Zhao, X. Dong, M. Bian, J. Zhao, Y Zhang, Y. Sun, J. Chen, X. Wang, Applied Surface Science, 2014, 314, 1026-1033

[26] K. Meyer, Journal of Non-Crystalline Solids, 1997, 209, 227-239

[27] P.Y. Shih, S.W. Yung, T.S. Chin, Journal of Non-Crystalline Solids, 1999, 244, 211-222

[28] K. Souiwa, M. Hidouri, O. Toulemonde, M. Duttine, M.B. Amara, Journal of Alloys and Compounds, 2015, 627, 153-160

[29] X. Wei, J. Zhao, W. Zhang, Y. Li, M. Yin, Journal of Rare Earth, 2010, 28, 166-170

[30] A.N. Meza-Rocha, A. Speghini, M. Bettinelli, U. Caldino, Journal of Luminescence, 2015, 167, 305-309

[31] J.R. Silva, L.A. Bueno, A.S. Gouveia-Neto, Journal of Luminescence, 2014, 154, 531-534

[32] R. Yu, J. Wang, Z. Zhao, M. Li, S. Huo, J. Li, J. Wang, Materials Letters, 2015, 160, 294-297

[33] A. Pandey, R. Dey, V.K. Rai, Journal of Physical Chemistry and Biophysics, 3: 129. Doi:10. 4172/2161-0398.1000129

Chapter 6

Energy transfer in Er^{3+}:Yb^{3+} co-doped calcium phosphate phosphor powders.

6.1. Introduction

Calcium phosphate is considered as a promising host for efficient upconversion due to its short distance between positions that can be occupied by the dopants, high solubility of ytterbium ions and it exhibit close ionic size to lanthanides [1]. Alkaline earth ions such as Ca^{2+}, Sr^{2+}, and Ba^{2+} exhibit close ionic size to lanthanide ions. For efficient upconversion (UC) luminescence, the ionic radius of lanthanides needs to match with the host cation ions [2]. Intense visible upconversion luminescence can be obtained from lanthanides such as Yb^{3+}/Er^{3+}, Yb^{3+}/Ho^{3+} and Yb^{3+}/Tm^{3+} by excitation of near infrared (NIR) light [3]. Blue UC emission is observed from in materials doped with Tm^{3+}, red and green emissions are observed in materials doped with Ho^{3+} and Er^{3+}, respectively. Er^{3+} and Yb^{3+} co-doped materials have been known as the most efficient UP materials [4]. Er^{3+} has advantages such as large emission cross-section and long fluorescence lifetime [5]. Among these lanthanides, Yb^{3+} has a high rate and broad absorption band (ranging from 850-1050 nm), which makes it an excellent sensitizer. The energy can be transferred from Yb^{3+} to Er^{3+} ions, which is attributed to the superior energy level overlaps between the $^7F_{7/2} \rightarrow {}^2F_{5/2}$ of Yb^{3+} and $^4I1_{5/2} \rightarrow {}^4I_{11/2}$ of Er^{3+} ions, leading to bright UC emissions. The energy transfer processes and ground state absorption mentioned in the results are discussed in the literature.

$Ca_5(PO_4)_3OH$ co-doped Er^{3+}/Yb^{3+} phosphor powders were prepared by urea combustion method for application in photodynamic therapy. This chapter presents the results on structural and optical properties of Er^{3+} and Yb^{3+} co-doped $Ca_5(PO_4)_3OH$ phosphor powders. The main interest of this study is to check the luminescence behavior of Er^{3+}/Yb^{3+} as well as other characterization on the phosphors. The emission spectra of the phosphors are recorded and the probable mechanism involved in luminescence behavior by the phosphor is discussed.

6.2. Experimental

6.2.1 Preparation

$Ca_5(PO_4)_3OH$ co-doped Er^{3+}/Yb^{3+} phosphor powders were synthesized by combustion method using urea as a fuel. The following starting materials with 99% purity were used for the preparation of materials reported in this paper: strontium nitrate (6M $Ca(NO_3)_2{\cdot}4H_2O$), di-ammonium hydrogen phosphate ((4M $NH_4)_2HPO_4$), erbium nitrate ($Er(NO_3)_3{\cdot}5H_2O$), ytterbium nitrate ($Yb(NO_3)_3{\cdot}6H_2O$) with different concentrations of Er^{3+} (1 - 7 mol %), Yb^{3+} (7 mol %), and Er^{3+}:Yb^{3+} (3:5-15 mol %), and urea ($CO(NH_4)_2$). When a complete reaction is assumed, the theoretical equation for the formation of $Ca_5(PO_4)_3OH$ is given by:

$$15Ca(NO_3)_2{\cdot}4H_2O + 9(NH_4)_2HPO_4 + 16CH_4N_2O = 3Ca_5(PO_4)_3OH + 16CO_2 + 131H_2O + 40N_2 \quad (6.1)$$

All reagents, in stoichiometric amounts, were dissolved in 2 ml of distilled water and the mixture was stirred vigorously for 15 min in room temperature until a thick homogenous solution was formed. The solution was kept in a furnace for 10 minutes maintained at 600 °C. The solution boiled, underwent dehydration and decomposed while generating combustible gases such as CO_2, N_2 and H_2O. The combustion ashes were cooled to room temperature and were ground gently using a pestle and mortar resulting in a fine powder. The materials synthesized were $Ca_5(PO_4)_3OH$, $Ca_5(PO_4)_3OH:Er^{3+}$, $Ca_5(PO_4)_3OH:Yb^{3+}$ and $Ca_5(PO_4)_3OH:Er^{3+},Yb^{3+}$. All the powders were annealed at 800 °C in air for 2 hours.

The materials synthesized were $Ca_5(PO_4)_3OH$, $Ca_5(PO_4)_3OH:Er^{3+}$, $Ca_5(PO_4)_3OH:Yb^{3+}$ and $Ca_5(PO_4)_3OH:Er^{3+},Yb^{3+}$ phosphor powders with different concentrations of Er^{3+} in the range from 1 -7 mol%, Yb^{3+} (7mol %), and Er^{3+}:Yb^{3+} (3:5-15 mol%).

6.2.2 Measurements

The crystalline structure of the phosphors was analyzed using a Bruker AXS D8 X-ray Diffraction (XRD) with Cu Kα1 radiation (λ = 1.5406Å) in the range from 20 to 60° (2θ). The schematic representation of the different sites of Ba with the coordination PO_4^{3-} material was drawn using DIAMOND crystal structure software. Particle morphology was examined using Jeol JSM-7800F thermal field emission scanning electron microscope (FE-SEM) coupled with Oxford Aztec 350 X-Max80 Energy x-ray Dispersive Spectroscopy (EDS) which was used to analyse the chemical composition of the phosphors under typical vacuum of 9.634×10^{-5} Pa. The absorption and bandgap energy were evaluated using Perkin Elmer

Lambda 950 UV-Vis spectrometer. Upconversion luminescence emission was measured by using a photoluminescence system consisting of fibre-coupled 980 nm NIR (near infrared) laser as the excitation source, iHR320 Horiba Yvon imaging spectrometer, R943 -02 Hamamatsu Photonics photomultiplier (PMT) detector and a SR830 Standford Research System lock-in amplifier.

6.3. Results and Discussion

6.3.1. Phase analysis

The XRD patterns of $Ca_5(PO_4)_3OH$ powders for both as-prepared and those annealed at 800 ^{0}C are shown in Figure 6.1. The diffraction peaks in the figure are be attributed to the hexagonal phase of $Ca_5(PO_4)_3OH$ referenced in ICDD file No. 00-073-0293. The XRD pattern of the as-prepared powder exhibit broad peaks, indicating low crystallinity of the structure. The crystallinity of the powder showed great improvement after annealing. The average crystallite sizes of both as-prepared and annealed $Ca_5(PO_4)_3OH$ powders were calculated to be 27 and 44 nm, respectively, using Debye-Scherrer equation . There are impurities observed at 2Θ = 29 and 31 ^{o}, which may be due to $Ca_2P_2O_7$ and CaO. Impurities can be removed by annealing at high temperatures. The powder could not be annealed at temperatures high than 1000 ^{o}C due to its melting point at 1100 ^{o}C.

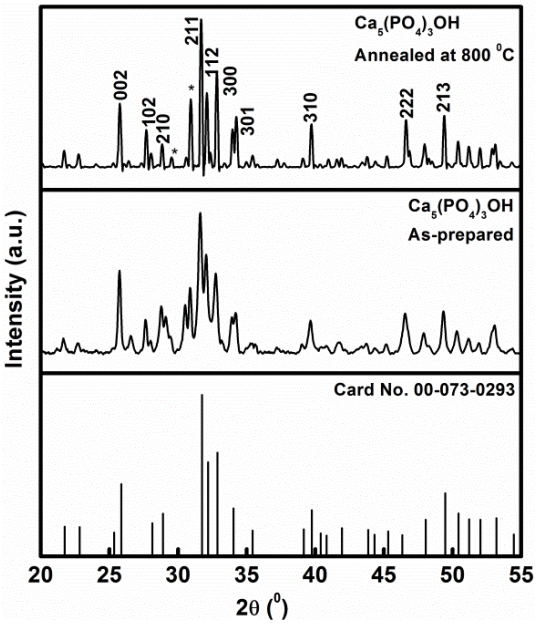

Figure 6. 1 XRD pattern of $Ca_5(PO_4)_3OH$ for both as-prepared and annealed (800 ^{o}C) powders and standard data 00-073-0293.

6.3.2. Particle morphology and chemical composition analysis

Figure 6.2. shows the FESEM micrographs of $Ca_5(PO_4)_3OH$, $Ca_5(PO_4)_3OH:Er^{3+}$, $Ca_5(PO_4)_3OH:Yb^{3+}$ and $Ca_5(PO_4)_3OH:Er^{3+},Yb^{3+}$ and EDS spectrum co-doped $Ca_5(PO_4)_3OH$. Figure 6.2. (a) shows the SEM micrograph of $Ca_5(PO_4)_3OH$. The powder exhibited rod or plate-like morphology forming flowers. For Figure 6.2 (b), (c) and (d) similar morphology were observed for three different phosphors with plate-like structures and small agglomerated particles on top of the plates.

The elemental composition and purity of the phosphor powders were determined by running the EDS analysis over the lager area of the FESEM image. The EDS spectrum in Figure 6.2. (e) shows that the powder is composed of Ca, P, O, Er^{3+}, and Yb^{3+} elements. The carbon peak observed is attributed to the carbon tape on which the powder was mounted. The inset shows quantitative view of the elemental composition on the inspection field in units of weight percentage. The results reveal that all elements are the main elements, with high signals from Yb^{3+}, which is due to high concentration of Yb^{3+} ion (15 mol%) used.

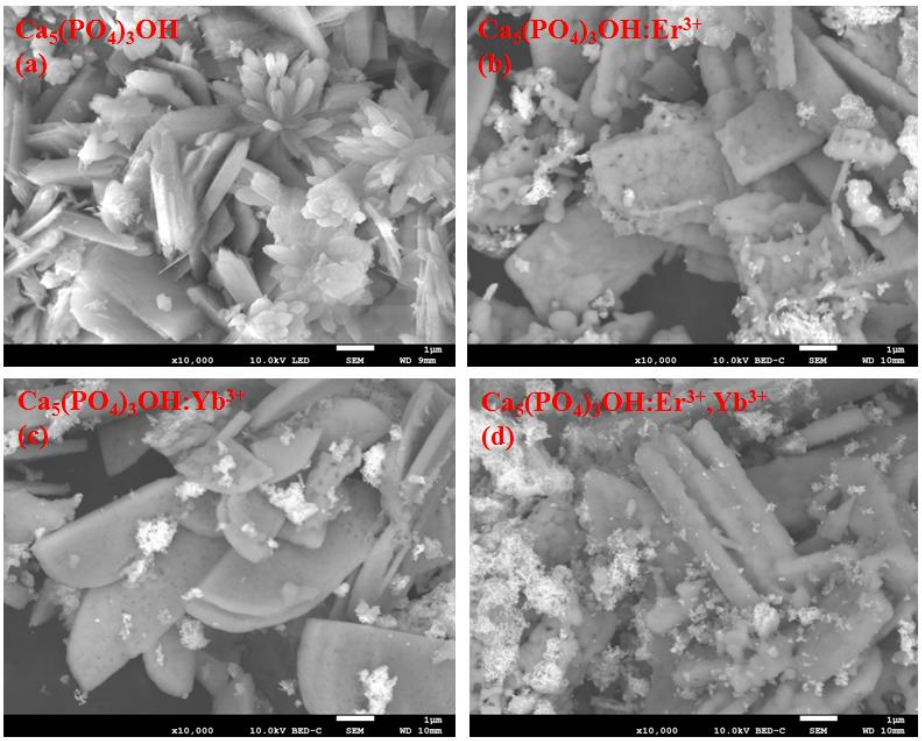

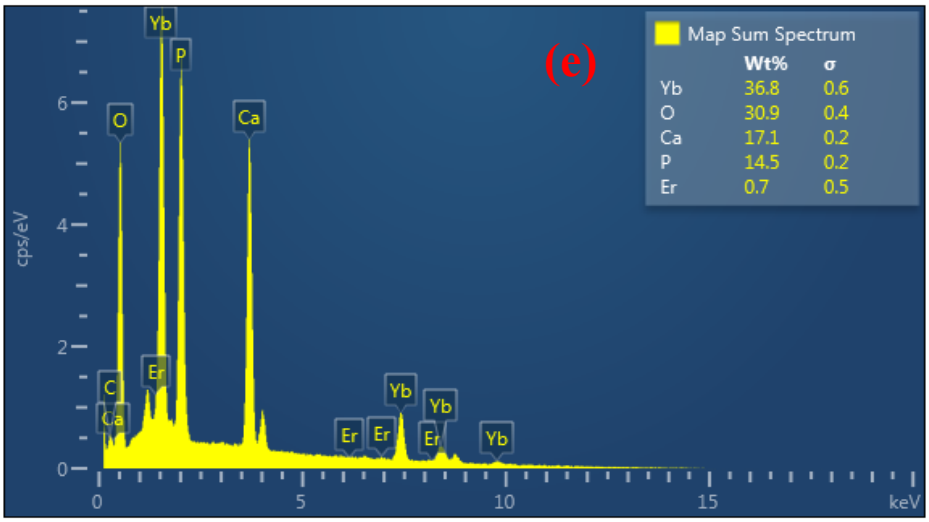

Figure 6.2 (a)–(d) SEM image of $Ca_5(PO_4)_3OH$, $Ca_5(PO_4)_3OH:Er^{3+}$, $Ca_5(PO_4)_3OH:Yb^{3+}$ and $Ca_5(PO_4)_3OH:Er^{3+},Yb^{3+}$ phosphor powders and (e) EDS analysis of $Ca_5(PO_4)_3OH:Er^{3+},Yb^{3+}$ phosphor powders.

6.3.3 UV-Vis diffuse reflectance spectra and Bandgap analysis

Figure 6.3 (a) shows the reflectance spectra of the different phosphor powders recorded in the wavelength range of 200-1000 nm. $Ca_5(PO_4)_3OH$ shows a small absorption band near 200 nm which is attributed to the interband transition of the host [6-8]. $Ca_5(PO_4)_3OH:Yb^{3+}$ system shows the band at 217, 283 and 979 nm attributed to interband transition, defects (oxygen vacancies or impurities) and Yb^{3+} transitions from ground state $^2F_{7/2}$ to the excited state $^2F_{5/2}$, respectively [9]. Er^{3+} doped $Ca_5(PO_4)_3OH$ shows absorption bands at 365,378, 409, 452, 489, 521, 653, 799 and 976 nm related to the transitions of Er^{3+} from the ground states $^4I1_{5/2}$ to $^2G_{7/2}$, $^4G_{11/2}$, $^2H_{9/2}$, $^2H_{11/2}$, $^3S_{3/4}$, $^4F_{9/2}$, $^4I_{9/2}$ and $^4I_{11/2}$ excited states, respectively [10-12]. Data plots of absorption versus energy in the absorption edge region are shown in Figure 6.3 (b). The bandgap energy values were determined by using Kubelka-Munk (K-M) function. By extrapolating the K-M function to K/S=0, the energy bandgaps of $Ca_5(PO_4)_3OH$, $Ca_5(PO_4)_3OH:Yb^{3+}$, $Ca_5(PO_4)_3OH:Er^{3+}$ and $Ca_5(PO_4)_3OH:Er^{3+},Yb^{3+}$ were estimated to be 5.8, 5.2, 5.1and 5.1 eV, respectively [13]. All stable appetites absorb around 260 eV and the energy bandgaps are between4 and 5 eV [14, 15]. Through the incorporation of the dopants, the bandgap was decreased, which may be due to structural changes taking place within the powder after the insertion of dopants [16, 17]. Dopants include the formation of great number of non-bridging oxygens, which accordingly decreases the optical bandgap [11].

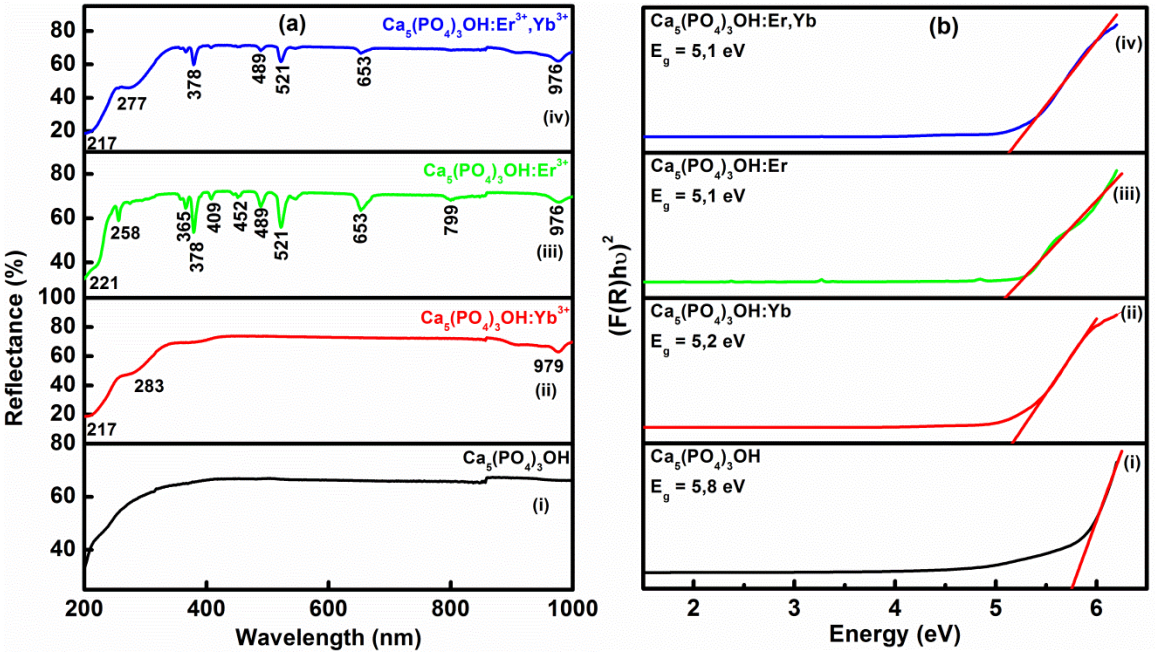

Figure 6.3. Reflectance and bandgap energy spectra of (i) $Ca_5(PO_4)_3OH$, (ii) $Ca_5(PO_4)_3OH:Er^{3+}$ and (iii) $Ca_5(PO_4)_3OH:Yb^{3+}$ and (iv) $Ca_5(PO_4)_3OH:Er^{3+},Yb^{3+}$ phosphor powders.

6.3.4 Photoluminescent properties of Er^{3+}/Yb^{3+} co-doped $Ca_5(PO_4)_3OH$ phosphor powder

Figure 6.4 (a) shows the up-conversion luminescence spectra of $Ca_5(PO_4)_3OH:Er^{3+}$ phosphors pumped at 980 nm. For Er^{3+} singly doped phosphors, emission peaks were observed in the green region ranging from 517 -573 nm and red region in the range of 653-679 nm, which correspond to $^2H_{11/2}+^4S_{3/2}\rightarrow{}^4I_{15/2}$ and $^4F_{9/2}\rightarrow{}^4I_{15/2}$ transitions of Er^{3+}, respectively [18-20]. $Ca_5(PO_4)_3OH:Er^{3+}$ phosphors were prepared in different concentrations of Er^{3+} ranging from 1-7 mol.%, the luminescence intensity increases with increasing concentrations from 1 to 3 mol%, and decrease at high concentrations of 5 and 7 mol% due to concentration quenching.

Figure 6.4 (b) shows the upconversion luminescence spectrum of $Ca_5(PO_4)_3OH:Yb^{3+}$ phosphor pumped at 980 nm. The prominent emission peak is observed at 474 nm with minor emission peaks in the range of 522-648 nm, the peaks are assigned to $^2F_{5/2}\rightarrow{}^2F_{7/2}$ transitions of Yb^{3+} ion.

Figure 6.4. (c) shows the upconversion luminescence spectra of $Ca_5(PO_4)_3OH:Er^{3+},Yb^{3+}$ phosphor powders with Er^{3+} concentrations constant and different Yb^{3+} ions concentrations of 5, 7, 10 and 15 mol%. The green upconversion emissions have multiple peaks at the range from 520-550nm, assigned to $^2H_{11/2}+^4S_{3/2}\rightarrow{}^4I_{15/2}$ transitions of Er^{3+} ion. The red

upconversion emission with the peaks at 661, 656 and 666 nm are assigned to $^4F_{9/2} \rightarrow {}^4I_{15/2}$ transitions of Er^{3+} ions. The emission intensities on both green and red region increase with increasing concentrations of Yb^{3+} ions [21]. Increasing the Yb^{3+} concentration, the green emission is enhanced faster than the red emission. The enhancement of green emission can be due to the increasing of the three-photon energy transfer process probability between Yb^{3+} and Er^{3+} ions.

Figure 6.4 (d) shows the possible upconversion energy mechanism that produces green and red emissions. Using 980 nm wavelength from the laser, $^2F_{5/2} \rightarrow {}^2F_{7/2}$ Yb^{3+} absorption takes place. The energy corresponding to the Yb^{3+} transitions is transferred to the ground state level ($^4I_{15/2}$) of Er^{3+} ion, which absorbs the first photon and reaches the $^4I_{11/2}$ level, this mechanism is known as first energy transfer process (ET1): $^4I_{15/2}$ (Er^{3+}) + $^2F_{5/2}$ (Yb^{3+}) → $^4I_{11/2}$ (Er^{3+}) + $^2F_{7/2}$ (Yb^{3+}).

The Er^{3+} ion can directly absorb the 980 nm incident light from its ground state $^4I_{15/2}$ to the $^4I_{11/2}$ level through ground state absorption (GSA) mechanism. Non-radiative de-excitation is observed in the $^4I_{11/2} \rightarrow {}^4I_{13/2}$ level.

The second photon from Yb^{3+} ion allows Er^{3+} ions to be pumped from $^4I_{13/2}$ to the $^4F_{9/2}$ state according to a second energy transfer process (ET2): $^4I_{13/2}$ (Er^{3+}) + $^2F_{5/2}$ (Yb^{3+}) → $^4F_{9/2}$ (Er^{3+}) + $^2F_{7/2}$ (Yb^{3+}). A red emission is observed corresponding to $^4F_{9/2} \rightarrow {}^4I_{15/2}$ transition of Er^{3+} ion. Non-radiative $^4F_{9/2} \rightarrow {}^4I_{11/2}$ de-excitation is observed.

The third energy transfer (ET3): $^4I_{11/2}$ (Er^{3+}) + $^2F_{5/2}$ (Yb^{3+}) → $^4F_{7/2}$ (Er^{3+}) + $^2F_{7/2}$ (Yb^{3+}) leads to population of the $^4F_{7/2}$ level from which the $^2H_{11/2}$ and $^4S_{3/2}$ levels are populated via non-radiative relaxation. This process gives rise to the green emission of Er^{3+}, which is considered as a three-photon process. The $^4I_{11/2} \rightarrow {}^4F_{7/2}$ excitation is possible via an excited state absorption process (ESA). The consecutive ET1-ET2-ET3 upconversion energy transfer mechanisms are needed to populate the $^2H_{11/2}$ and $^4S_{3/2}$ levels, hence the enhanced green emission [22].

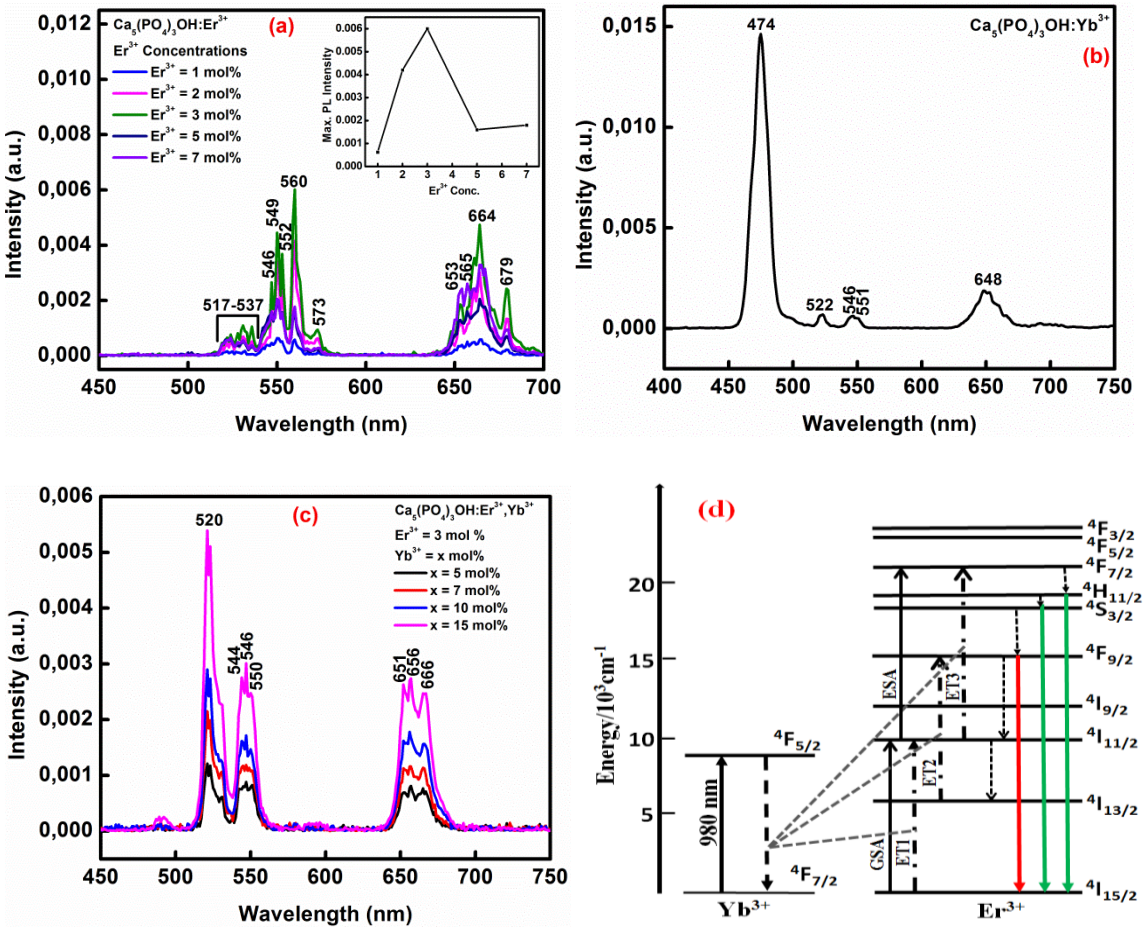

Figure 6.4 Upconversion emission spectra of (a) $Ca_5(PO_4)_3OH:Er^{3+}$, (b) $Ba_5(PO_4)_3OH:Yb^{3+}$, (c) $Ba_5(PO_4)_3OH:Er^{3+},Yb^{3+}$ phosphor powders and energy transfer mechanism of Er^{3+}/Yb^{3+}.

6.4. Conclusion

$Ca_5(PO_4)_3OH:Er^{3+},Yb^{3+}$ phosphor powders were successfully prepared by urea combustion method. The XRD patterns of $Ca_5(PO_4)_3OH$ powders for both as-prepared and annealed at 800 ^oC are shown. The XRD pattern of the as-prepared powder exhibit broad peaks, indicating low crystallinity of the structure. The crystallinity was improved after annealing. The SEM shows porous and rod-like structure formed due to the combustion reaction. The plate-like structures are made up by small spherical particles. The EDS spectrum confirms that the powders were composed of Ca, P, O, Er^{3+}, and Yb^{3+} elements. The reflectance spectra of the different powders ($Ca_5(PO_4)_3OH$, $Ca_5(PO_4)_3OH:Yb^{3+}$, $Ca_5(PO_4)_3OH:Er^{3+}$ and $Ca_5(PO_4)_3OH:Er^{3+},Yb^{3+}$) recorded in the wavelength range 200-1000 nm. The bandgap values were estimated to be 5.8, 5.2, 5.1 and 5.1 eV, respectively. The up-conversion luminescence spectra of $Ca_5(PO_4)_3OH:Er^{3+}$ phosphors were measure measured. Emission peaks were observed in the green region ranging from 517 -573 nm and red region in the

range from 653-679 nm assigned to Er^{3+} transitions. Upon co-doping the emission intensities on both green and red region increased with increasing concentrations of Yb^{3+} ions. The green emission was enhanced faster than the red emission. The enhancement of green emission can be due to the increase of the three-photon energy transfer process probability between Yb^{3+} and Er^{3+} ions. The energy transfer mechanism was discussed in details.

References

[1] A. Stefan, O. Toma, S. Georgescu, Journal of Luminescence, 2016, 180, 376-383

[2] J. Fu, R. Pang, Y. Jia, W. Sun, L. Jiang, S.Zhang, Journal of Luminescence, 2017, 181, 240-245

[3] Z. Liang, S. Zhao, Z. Xu, B. Qiao, Y. Yang, W. Zhu, X. Xu, Optical Materials, 2016, 62, 255-260

[4] C. Wang, X. Cheng, Journal of Alloys and Compounds, 2015, 649, 196-203

[5] C.X. Liu, X.L. Shen, H.T. Guo, W.N.Li, W. Wei, Optik, 2017, 131, 132-137

[6] P.P. Mokoena, I.M. Nagpure, V. Kumar, R.E. kroon, E.J. Olivier, J.H. Neethling, H.C. Swart, O.M. Ntwaeaborwa, Journal of Physics and Chemistry of Solids, 2014, 78, 998-1003

[7] J. Zhang, J. Jia, Z. Hua, Materials and Design, 2015, 87, 124-129

[8] J. Zhang, Z. Hua, S. Wen, Journal of Alloys and Compounds, 2015, 637, 70-76

[9] G. Li, C. Zhang, P. Song, P. Zhu, K. Zhu, J. He, Journal of Alloys and Compounds, 2016, 662, 89-93

[10] Z. Huang, M. Yi, H. Gao, Z. Zhang, Y. Mao, Journal of Alloys and Compounds, 2017, 241-245

[11] C.R. Kesavulu, H.J. Kim, S.W. Lee, J. Kaewkhao, N. Wantana, S. Kothan, Journal of Alloys and Compounds, 2016, 683, 590-598

[12] C. Wang, H. Xia, Z. feng, Z. Zhang, D. Jiang, X. Gu, Y. Zhang, B. Chen, H. Jiang, Journal of Alloys and Compounds, 2016, 686, 816-822

[13] P.P. Mokoena, I.M. Nagpure, V. Kumar, R.E. Kroon, E.J. Olivier, J.H. Neethling, H.C. Swart, O.M. Ntwaeaborwa, Journal of Physics and Chemistry of Solids, 2014, 75, 998-1003

[14] L. Calderin, M. Stott, Physical Review B., 67, 2003, 134106-1-7

[15] T.F. Stoica, C. Morosanu, A. Slav, T. Stoica, P. Osiceanu, C. Anastasescu, M. Gartner, M. Zaharescu, Thin Solid Films, 2008, 516, 8112-8116

[16] S. Selvi, K. Marimuthu, G. Muralidharan, Journal of Luminescene, 2015, 159, 207-218

[17] M. Ferhi, N.B. Hassen, C. Bouzidi, K. Horchani-Naifer, M. Ferid, Journal of Luminescence, 2016, 170, 174-179

[18] A. Pandey, S.Som, V. Kumar, V. Kumar, K. Kumar, V.K. Rai, H.C. Swart, Sensors and Actuators B:Chemical, 2014, 202, 1305-1312

[19] Y.K. Kshetri, B. Joshi, S.W. Lee, Journal of the European Ceramic Society, 2016, 36, 4215-4224

[20] G. Tang, X. Wen, Q. Qian, T. Zhu, W. Liu, M. Sun, X. Chen, Z. Yang, Journal of Alloys and Compounds, 2016, 664, 19-24

[21] Y.W. Seo, B.K. Moon, B.C. Choi, J.H. jeong, H. Choi, J.H. Kim, Ceramic International, 2015, 41, 14332-14339

[22] M.A. Hassairi, M. Dammak, D. Zambon, G. Chadeyron, R. Mahiou, Journal of Luminescence, 2017, 181, 393-399

Chapter 7

Cooperative upconversion luminescence in Eu^{3+}/Yb^{3+} co-doped $Ca_5(PO_4)_3OH$ phosphor powder

7.1. Introduction

Upconversion phosphors have a wide range of applications such as in solid-state visible laser devices, display devices, detectors, biolables, light emitting diodes and optical storage [1-3]. Upconversion luminescence (UCL) has been an attractive field of research in recent years. UC luminescence of rare earth (RE) ions has been observed under irradiation of the near infrared laser. The up-converted RE^{3+} luminescence is generated by two processes. First process, cooperative energy transfer (CET), i.e. transfer of energy from two simultaneous excited Yb^{3+} ions to one nearby RE^{3+} ion with the excited state at 20 000 cm^{-1}, without formation of Yb-pair. Second process, cooperative upconversion, i.e. energy transfer from the excited Yb-pair to the single RE^{3+} state at about 20 000 cm^{-1} [4]. Researchers have found out that Er^{3+}/Tm^{3+} and Yb^{3+} are the most efficient UCL and energy transfer upconversion mechanism plays a dominant role [2, 5]. Eu^{3+} has been rarely considered as an UCL ion, because it cannot be directly excited by near infrared (NIR) due to the absence of energy levels corresponding to 10 2000cm^{-1} energy. However, it can be sensitized by an excited Yb^{3+} ion. The energy can be transferred from pair of interacting Yb^{3+} ions to single Eu^{3+} ion, by cooperative energy transfer [6-7]. The UCL can be partially suppressed by cooperative emission of Yb^{3+} pairs. The literature regarding the upconversion luminescence of Yb^{3+}-Eu^{3+} system is limited comparing to other RE. The structure, optical absorption and visible luminescence under direct excitation of the Eu^{3+} ions, as well as NIR excitation via the $2Yb^{3+}$ to Eu^{3+} cooperative energy-transfer process is presented in this chapter.

7.2. Experimental

7.2.1 Preparations

$Ca_5(PO_4)_3OH$ co-doped Eu^{3+}/Yb^{3+} phosphor powders were synthesized by combustion method using urea as a fuel. The following starting materials with 99% purity were used for the preparation of materials reported in this paper: strontium nitrate (6M $Ca(NO_3)_2{\cdot}4H_2O$), di-ammonium hydrogen phosphate ((4M $NH_4)_2HPO_4$), europium nitrate ($Eu(NO_3)_3{\cdot}5H_2O$), ytterbium nitrate ($Yb(NO_3)_3{\cdot}6H_2O$) with different concentrations of Eu^{3+} (0.1 - 7 mol %), Yb^{3+} (7 mol %), and Er^{3+}:Yb^{3+} (3:1-7 mol %), and urea ($CO(NH_4)_2$). When a complete reaction is assumed, the theoretical equation for the formation of $Ca_5(PO_4)_3OH$ is given by:

$$15Ca(NO_3)_2{\cdot}4H_2O + 9(NH_4)_2HPO_4 + 16CH_4N_2O = 3Ca_5(PO_4)_3OH + 16CO_2 + 131H_2O + 40N_2 \quad (7.1)$$

All reagents, in stoichiometric amounts, were dissolved in 2 ml of distilled water and the mixture was stirred vigorously for 15 min in room temperature until a thick homogenous solution was formed. The solution was kept in a furnace for 10 minutes maintained at 600 °C. The solution boiled, underwent dehydration and decomposed while generating combustible gases such as CO_2, N_2 and H_2O. The combustion ashes were cooled to room temperature and were ground gently using a pestle and mortar resulting in a fine powder. The materials synthesized were $Ca_5(PO_4)_3OH$, $Ca_5(PO_4)_3OH:Eu^{3+}$, $Ca_5(PO_4)_3OH:Yb^{3+}$ and $Ca_5(PO_4)_3OH:Eu^{3+},Yb^{3+}$. All the powders were annealed at 800 °C in air for 2 hours.

7.2.2 Measurements

The crystalline structure of the phosphors was analyzed using a Bruker AXS D8 X-ray Diffraction (XRD) with Cu Kα1 radiation (λ = 1.5406Å) in the range of 20 to 60° (2θ). The schematic representation of the different sites of Ba with the coordination PO_4^{3-} material was drawn using DIAMOND crystal structure software. Particle morphology was examined using JEOL JSM-7800F thermal field emission scanning electron microscope (FE-SEM) coupled with Oxford Aztec 350 X-Max80 Energy x-ray Dispersive Spectroscopy (EDS) which was used to analyse the chemical composition of the phosphors under typical vacuum of 9.634×10^{-5} Pa. The absorption and bandgap energy were evaluated using Perkin Elmer Lambda 950 UV-Vis spectrometer. Upconversion photoluminescence emission was measured by using a photoluminescence system consisting of fiber-coupled 980 nm NIR (near infrared) laser as the excitation source, iHR320 Horiba Yvon imaging spectrometer, R943 -02 Hamamatsu Photonics photomultiplier (PMT) detector and a SR830 Standford

Research System lock-in amplifier for $Ca_5(PO_4)_3OH:Yb^{3+}$ and $Ca_5(PO_4)_3OH:Eu^{3+}:Yb^{3+}$ phosphor powders and Cary eclipse fluorescence with monochromatized xenon lamp for $Ca_5(PO_4)_3OH:Eu^{3+}$ phosphor powders.

7.3. Results and Discussion

7.3.1 Phase analysis

The XRD patterns of $Ca_5(PO_4)_3OH$ powder for both as-prepared and annealed powder at 800 ^{0}C are shown in Figure 7.1. The patterns are in good agreement with the standard data of $Ca_5(PO_4)_3OH$ (ICDD card no. 00-073-0293). The as-prepared powder was less crystalline with broader peaks, which is due to the nature of as-prepared powders that includes relatively smaller particle sizes and incomplete cancelling of incoherent scattering [8]. The lines became more narrow and sharp as the powder was annealed at 800 ^{0}C probably due to increase in particle sizes and crystallinity. The annealed powder is well crystalline and has $Ca_5(PO_4)_3OH$ phase, with hexagonal crystal structure. There are additional peaks observed at $2\theta = 29.50$ and 30.96^0 marked with asterisks (*) which are impurities attributed to unreacted $Ca_2P_2O_7$ and CaO during the reaction [9]. Average crystal sizes for as-prepared and annealed powders were calculated using Scherrer equation:

$$D = \frac{k\lambda}{\beta \cos\theta} \tag{7.2}$$

Where k is the Scherrer's constant (0.98), λ is the wavelength of X-ray (1.54060 Å), β is the full-width at half maxima, θ is the Bragg angle of the XRD peak. The crystal sizes calculated for as-prepared and annealed powders were found to be 27 and 44 nm, respectively.

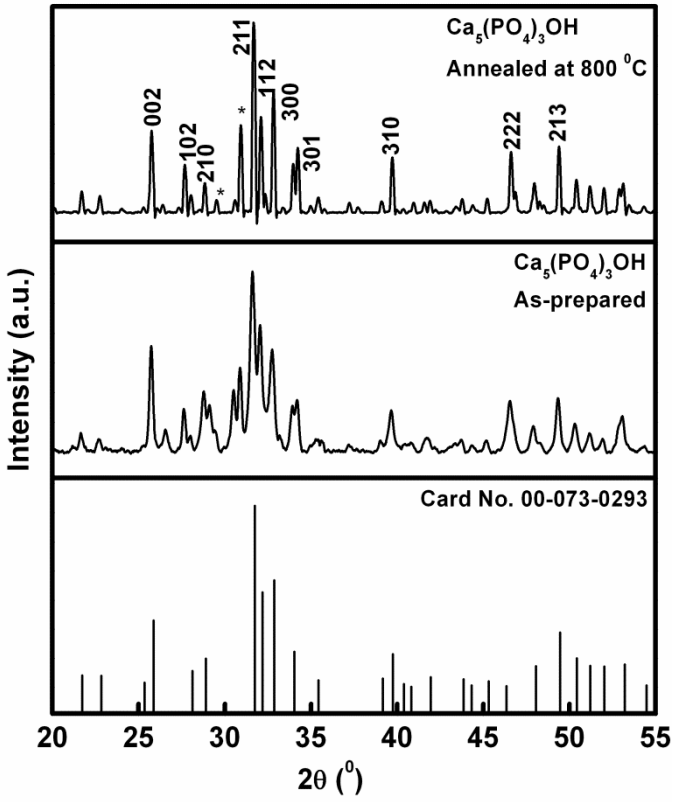

Figure 7.1 XRD patterns of both as-prepared and annealed (800 °C) $Ca_5(PO_4)_3OH$ powders.

7.3.2 Particle morphology and chemical composition analysis

Figure 7.2 (a) - (d) shows the SEM micrograph of $Ca_5(PO_4)_3OH$ and $Ca_5(PO_4)_3OH:Eu^{3+},Yb^{3+}$ phosphor powders for both as-prepared and annealed phosphors, Figure 7.2 (e) and (f) shows the EDS spectrum and mapping of $Ca_5(PO_4)_3OH:Eu^{3+},Yb^{3+}$ phosphor powder, respectively. $Ca_5(PO_4)_3OH$ for both as-prepared and annealed powders exhibited plate-like morphology formed by small agglomerated spherical particles. Agglomeration of spherical particle is more visible on the annealed powder, due to bigger particle size after annealing. $Ca_5(PO_4)_3OH:Eu^{3+},Yb^{3+}$ powders for both as-prepared and annealed exhibited a large rod-like or plate-like morphology and small agglomerated particles encrusted on the surface of bigger particles. The EDS spectrum in figure 7.2 (e) confirm the formation of $Ca_5(PO_4)_3OH:Eu^{3+},Yb^{3+}$ phosphor powder by the presence of Ca, P, O, Eu^{3+} and Yb^{3+} elements with different weight percentages in the inset. Figure 7.2 (f) shows the elemental mapping of $Ca_5(PO_4)_3OH:Eu^{3+},Yb^{3+}$ phosphor powder. The elements Ca, P, and O are evenly distributed on the surface, Eu^{3+} and Yb^{3+} elements are clustered in one position occupying the small agglomerated particles.

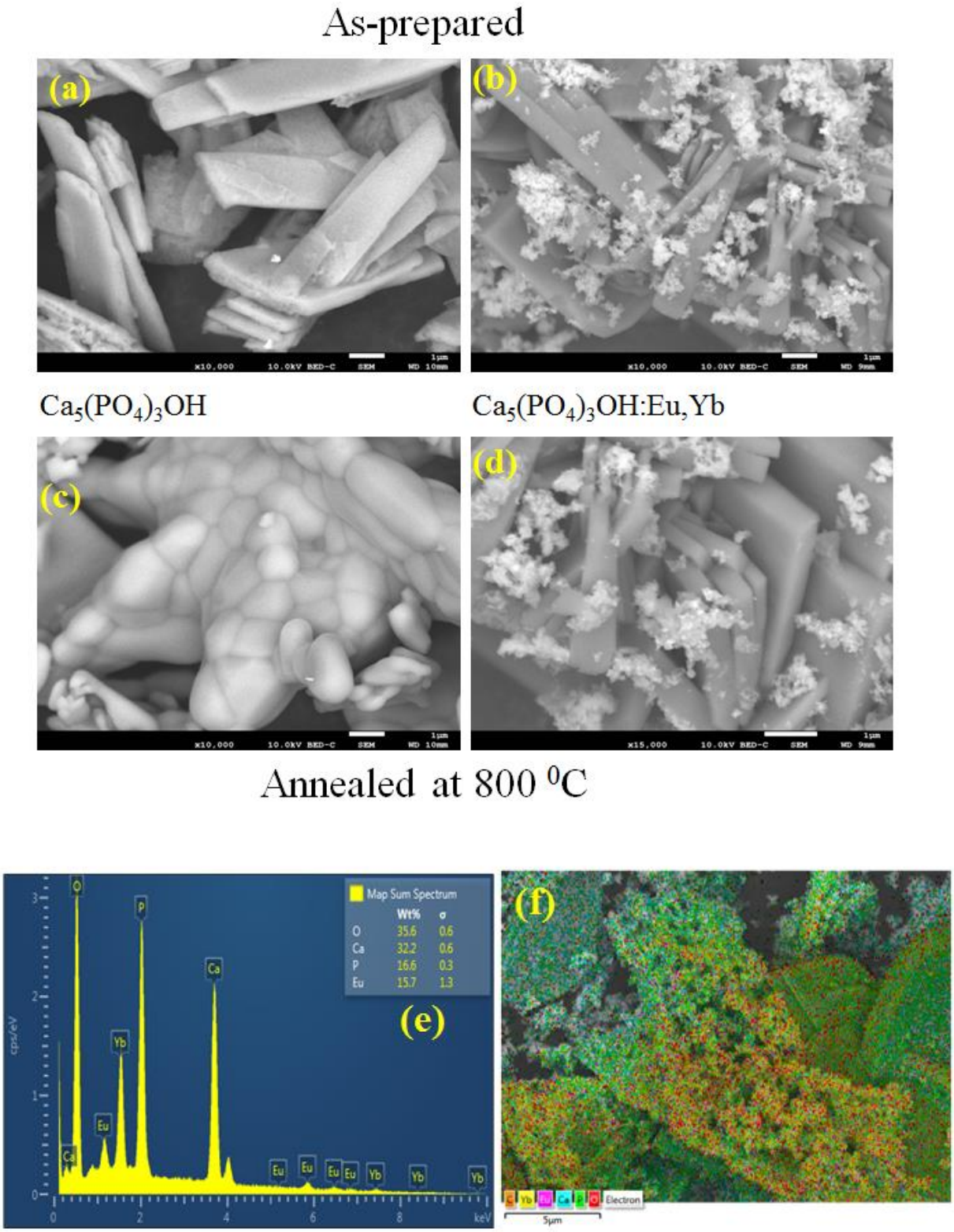

Figure 7.2 SEM micrograph of (a) and (c) $Ca_5(PO_4)_3OH$ and (b) and (d) $Ca_5(PO_4)_3OH:Eu^{3+},Yb^{3+}$ for both as-prepared and annealed phosphors, (e) EDS spectrum and (f) mapping of $Ca_5(PO_4)_3OH:Eu^{3+},Yb^{3+}$ phosphor powder.

7.3.3. UV-Vis diffuse reflectance spectra and Bandgap analysis

Figure 7.3 shows the reflectance spectra of different phosphor powders. From the reflectance spectrum in figure 7.3.a (i), it can be seen that $Ca_5(PO_4)_3OH$ powder shows no absorption in the range from 250-1000 nm [10-11]. The absorption band below 250 nm is generally attributed to the transition of the host from the valence band to conduction band [12]. Figure 7.3.a (ii) shows the two UV absorption bands at 214 and 283nm, attributed to band-to-band or intrinsic transitions of a host and charge transfer state of Yb^{3+} [13-14]. The absorption peak in the near-infrared at 977 nm is attributed to $^2F_{7/2} \rightarrow {}^2F_{5/2}$ transition of Yb^{3+} ions [15]. Figure 7.3.a (iii) shows the absorption peaks at 216 and 314nm attributed to host transitions. There are minor absorption peaks observed at 393, 465, 527, and 573 nm which are attributed to $^7F_0 \rightarrow {}^5L_6$, $^7F_0 \rightarrow {}^5D_2$, $^7F_0 \rightarrow {}^5D_1$ and $^7F_0 \rightarrow {}^5D_0$ transitions of Eu^{3+} ion, respectively [16-17]. The inset shows the absorption peaks in the range of 380-600 nm. $Ca_5(PO_4)_3OH:Eu^{3+},Yb^{3+}$ system shows similar trend of peaks as in $Ca_5(PO_4)_3OH:Eu^{3+}$ system, with extra peak at 974 nm attributed to Yb^{3+} transitions. The data plot of absorption versus energy in the absorption edge is shown in figure 7.3 (b). The bandgap energies were determined by using Kubelka-Munk function. By extrapolating the K-M function to K/S=0, bandgap energies of $Ca_5(PO_4)_3OH$, $Ca_5(PO_4)_3OH:Eu^{3+}$, $Ca_5(PO_4)_3OH:Yb^{3+}$ and $Ca_5(PO_4)_3OH:Eu^{3+},Yb^{3+}$ phosphor powders were 5.6, 5.2, 5.1 and 4.9 eV, respectively. The decrease may be due to structural changes taking place within the powder after the insertion of dopants. Dopants include the formation of great number of non-bridging oxygens, which accordingly decreases the optical bandgap [12]. The bandgap energy of the $Ca_5(PO_4)_3OH$ powder obtained is much comparable with the bandgap energy of $Ba_{10}(PO_4)_6F_2$,$Ca_{10}Li(PO_4)_7$:Sr and $Ca_{3-x-y}Sr_y(PO_4)_2$ [18-21].

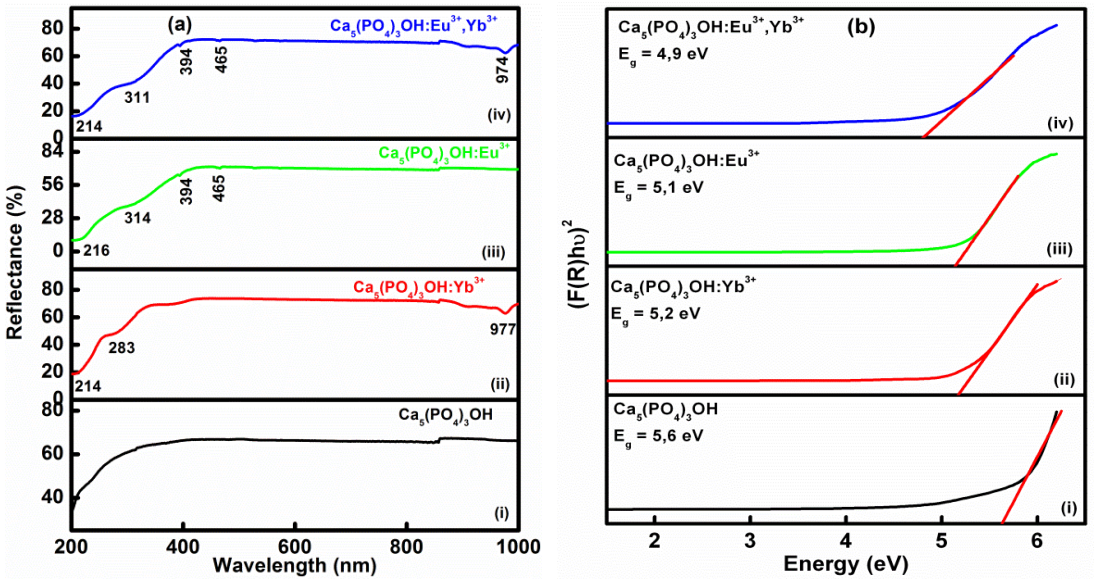

Figure 7.3 (a) Reflectance spectra of $Ca_5(PO_4)_3OH$, $Ca_5(PO_4)_3OH:Eu^{3+}$, $Ca_5(PO_4)_3OH:Yb^{3+}$ and $Ca_5(PO_4)_3OH:Eu^{3+},Yb^{3+}$ phosphor powders, and (b) bandgap energies of all the phosphor powders

7.3.4. Photoluminescence properties of Eu^{3+}/Yb^{3+} co-doped $Ca_5(PO_4)_3OH$ phosphor powder.

Figure 7.4 (a) shows the PL excitation and emission spectra of Eu^{3+} (0.1-7 mol%) doped $Ca_5(PO_4)_3OH$ phosphor powders. The broad excitation band observed at 248 nm is attributed to charge-transfer band (CTB), originating from the transition of a ligand O^{2-} 2p orbital to the empty states at about $4f^6$ configuration of Eu^{3+} (Eu^{3+}-O^{2-} transition) [22-23]. The narrow excitation peaks within the 4f electron configuration of Eu^{3+} ions are assigned to $^7F_0 \rightarrow {}^5D_4$ (361 nm), $^7F_0 \rightarrow {}^5G_2$ (380 nm), $^7F_0 \rightarrow {}^5L_6$ (395 nm), $^7F_0 \rightarrow {}^5D_3$ (412 nm), $^7F_0 \rightarrow {}^5D_2$ (464 nm), $^7F_0 \rightarrow {}^5D_1$ (529 nm), and $^7F_0 \rightarrow {}^5D_0$ (573 nm) transitions [24-25]. The emission spectra upon 248 nm excitation, displays four emission bands centered at 592, 614, 652, and 700 nm, assigned to the $^5D_0$ level to $^7F_1$, $^7F_2$, $^7F_3$, and $^7F_4$, transitions of Eu^{3+} respectively [26-29] .

Figure 7.4 (b) shows the upconversion luminescence spectrum of $Ca_5(PO_4)_3OH:Yb^{3+}$ phosphor pumped at 980 nm. The prominent emission peak is observed at 474 nm with minor emission peaks in the range of 522-648 nm, the peaks are assigned to $^2F_{5/2} \rightarrow {}^2F_{7/2}$ transitions of Yb^{3+} ion and other additional peaks may be due to impurities.

Figure 7.4 (c) shows the UC emission spectrum of $Ca_5(PO_4)_3OH:Eu^{3+},Yb^{3+}$ phosphor powder under 980 nm excitation. The 980 nm photons excites Yb^{3+} ion in the $^2F_{5/2}$ state. Prominent red emission from Eu^{3+} ion is clearly observed at 613 nm together with minor emission peaks at 547, 591, 654 and 697 nm. The emission peaks are assigned to different transitions of Eu^{3+}

ion as described above. The prominent red emission from Eu^{3+} is due to energy transfer from Yb^{3+} ion. The $^2F_{7/2}$ state of Yb^{3+} ion is two times low than the metastable $^5D_0$ state of Eu^{3+}, so the direct energy transfer cannot occur. Yb^{3+} ion can form a pair with a virtual excited state, the energy will be twice $^2F_{7/2}$ that is close to the energy of $^5D_1$ state of Eu^{3+}.

Thus, a cooperative energy transfer from Yb^{3+} ion pair to a single Eu^{3+} ion can occur, by fast non-radiative relaxation to the metastable $^5D_0$ state, and the red Eu^{3+} emission is observed [30]. The energy transfer is through dipole-dipole interaction involving pairs of Yb^{3+} and the state of Eu^{3+} ions. The detailed energy transfer process between Eu^{3+} and Yb^{3+} is explained in chapter 5. The schematic diagram of energy transfer between Eu^{3+} and Yb^{3+} is illustrated by figure 8.4 (d). The calculated experimental volume of $Ca_5(PO_4)_3OH$ powder was found to be 520.96 $Å^3$ which is comparable to the theoretical volume which is 521.26 $Å^3$. Furthermore, the critical distance was calculated by using the following equation:

$$R_c = 2\left(\frac{3V}{4\pi\chi_c N}\right)^{\frac{1}{3}} \tag{7.3}$$

R_c is the critical distance, V is the volume per unit cell, χ_c is the total concentration of Eu^{3+} and Yb^{3+} ions, N is the number of available site of Ca^{2+} occupying per unit cell. The calculated critical distance is 4.99 $Å^3$.

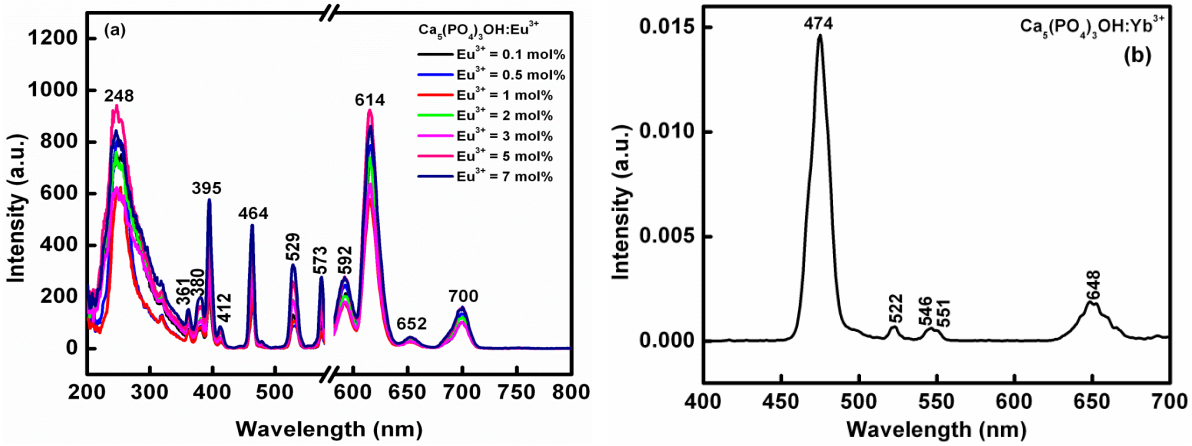

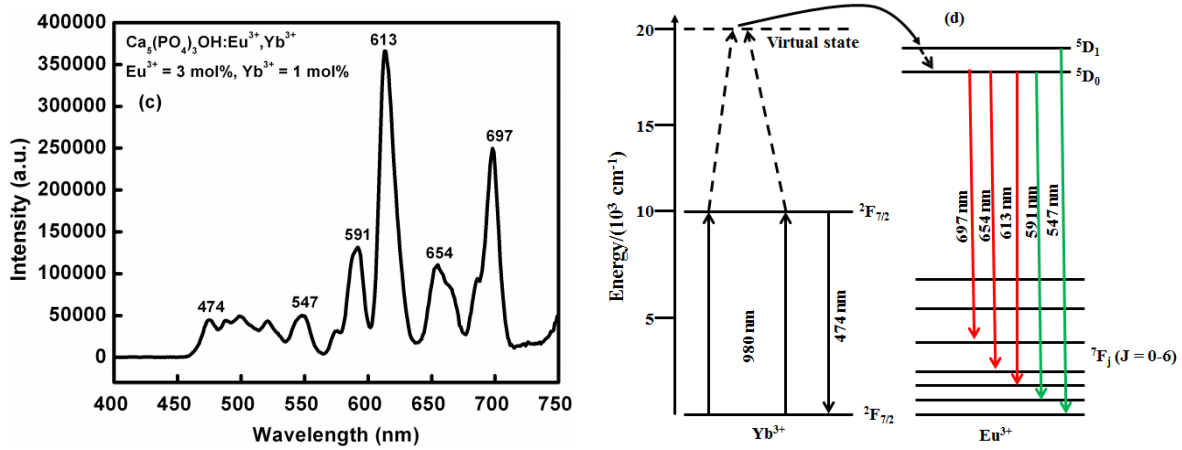

Figure 7.4 (a) PL excitation and emission spectra of $Ca_5(PO_4)_3OH:Eu^{3+}$ phosphor powders at different concentrations of Eu^{3+} ions, (b) and (c) PL emission of $Ca_5(PO_4)_3OH:Yb^{3+}$ and $Ca_5(PO_4)_3OH:Eu^{3+},Yb^{3+}$ phosphor powders pumped by 980 nm laser, and (d) energy transfer between Eu^{3+}/Yb^{3+}.

7.4. Conclusion

In conclusion, $Ca_5(PO_4)_3OH$ co-doped Eu^{3+}/Yb^{3+} phosphor powder were successfully synthesized by urea combustion method. The XRD data is in good agreement with the standard data (card no. 00-073-0293) of $Ca_5(PO_4)_3OH$ powder. $Ca_5(PO_4)_3OH$ powders for both as-prepared and annealed exhibited a large rod-like or plate-like morphologies and small agglomerated particles attached to bigger particles. EDS spectra and mapping confirm the formation of $Ca_5(PO_4)_3OH$ powders. Eu^{3+} and Yb^{3+} elements are clustered in one position occupying the small agglomerated particles. The estimated bandgap energies of $Ca_5(PO_4)_3OH$, $Ca_5(PO_4)_3OH:Eu^{3+}$, $Ca_5(PO_4)_3OH:Yb^{3+}$ and $Ca_5(PO_4)_3OH:Eu^{3+},Yb^{3+}$ phosphor powders were 5.6, 5.2, 5.1 and 4.9 eV, respectively. PL excitation and emission spectra of Eu^{3+}/Yb^{3+} co-doped $Ca_5(PO_4)_3OH$ phosphor powders were recorded. Upon 980 nm excitation, a prominent red emission peak at 613 nm and minor emission peaks at 547, 591, 654 and 697 nm from Eu^{3+} ion were clearly observed. The emission peaks are assigned to different transitions of Eu^{3+} ion

References

[1] X. Wei, J. Zhao, W. Zhang, Y. Li, M. Yin, Journal of Rare Earths, 2010, 28, 166-170

[2] X. Liu, Y. Li, T. Aidilibike, J. Guo, W. Di, W. Qin, Journal of Luminescence, 2017, 185, 247-250

[3] M. Pichalska, E. Zych, M. Sobczyk, A. Watras, P. Deren, Materials Chemistry and Physics, 2014, 147, 304-310

[4] X. Qiao, T. Tsuboi, H.J. Seo, Journal of Alloys and Compounds, 2016, 687, 179-187

[5] A. Tyminski, T. Grzyb, Journal of Luminescence, 2017, 181, 411-420

[6] M. Puchalska, E. Zych, A. Watras, Journal of Luminescence, 2017, 183, 185-192

[7] P.A. Loiko, G.E. Rachkovskaya, G.B. Zakharevich, A.A. kornienko, E.B. Dunina, A.S. Yasukevich, K.V. Yumashev, Journal of Non-Crystalline solids, 2014, 392-392, 39-44

[8] M. Karimi, S. Hesaraki, M. Alizadeh, A. Kazemzadeh, Material Letters, 2016, 175, 89-92

[9] S.C. Wu, H.C. Hsu, S.K. Hsu, Y.C. Chang, W.F. Ho, Ceramics International, 2015, 41, 10718-10724

[10] Y. Liu, C.Y. Liu, J.H. Wei, R. Xiong, C.X. Pan, J. Shi, Applied Surface Science, 2010, 256, 6390-6394

[11] G. M. Neelgund, A. R. Oki, Journal of Colloid and Interface Science, 2016, 484, 135-145

[12] J. Zhang, J. Jia, Z. Hua, Materials and Design, 2015, 87, 124-129

[13] Z.W. Zhang, L. Liu, S.T Song, J.P. Zhang, D. J. Wang, Current Applied Physics, 2015, 15, 248-252

[14] J. Zhou, Y. Teng, G. Lin, J. Qiu, Journal of Non-Crystalline Solids, 2011, 357, 2336-2339

[15] A. Kumari, V.K. Rai, K. Kumar, Spectrochimica Part Acta A: Molecular and Biomolecular Spectroscopy, 2014, 127, 98-101

[16] J. Chen, W. Zhao, J. Wang, N. Wang, Y. Meng, J. He, X. Zhang, Ceramics International, 2015, 41, 11945-11952

[17] S.S. Barbara, N. Pawlik, A.S. Swinarew, W.A. Pisarski, Journal of Luminescence, 2015, 166, 356-360

[12] C.R. Kesavulu, H.J. Kim, S.W. Lee, J. Kaewkhao, N. Wantana, S. Kothan, Journal of Alloys and Compounds, 2016, 683, 590-598

[18] J. Zhang, J. Jia, Z. Hua, Materials and Design, 2015, 87, 124-129

[19] J. Zhang, Z. Hua, S. Wen, Journal of Alloys and Compounds, 2015, 637, 70-76

[20] E Yang, G. Li, C. Fu, J. Zheng, X. Huang, W. Xu, L. Li, Journal of Alloys and Compounds, 2015, 647, 648-699

[21] J.H. Kim, Physica B, 2017, 505, 52-55

[22] C. Shivakumara, R. Saraf, S. Behera, N. Dhananjaya, H. Nagabhushana, Spectrochimica Acta Part A: Molecular and Biomolecular Spectroscopy, 2015, 151, 141-148

[23] B. Han, P. Li, J. Zhang, J. Zhang, Y. Xue, X. Suo, Q. Huang, Y. Feng, H. Shi, Materials Letters, 2015, 158, 208-210

[24] K.N. Kumar, R. Padma, L. Vijayalakshmi, J.S.M. Nithya, M. Kang, Journal of Luminescence, 2017, 182, 208-219

[25] V. Naresh, K. Gupta, C.P. Reddy, B.S. Ham, Spectrochimica Acta Part A: Molecular and Biomolecular Spectroscopy, 2017, 175, 43-50

[26] G. Chen, F. Wang, J. Yu, H. Zhang, X. Zhang, Journal of Molecular Structure, 2017, 1128, 1-4

[27] Y. Zeng, K. Qiu, Z. Yang, Y. Bu, W. Zhang, J. Li, Ceramics International, 2017, 43, 830-834

[28] P.A. Loiko, O.S. Dymshits, I.P. Alekseeva, A.A. Zhilin, M.Ya, Tsenter, E.V. Vilejshikova, K.V. Bogdanov, X. Mateos, K.V. Yumashev, Journal of Luminescence, 2016, 179, 64-73

[29] W.J. Zhang, X.B. Li, L.J. Wu, Y.Y. Yu, X.Z. Wang, S.Q. Liu, Z. Wang, W.C. Wang, Y. Liu, Physica B, 2017, 508, 22-26

[30] H. Xia, J. Feng, Y. Ji, Y. Sun, Y. Wang, Z. Jia, C. Tu, Journal of Quantitative Spectroscopy & Radiative Transfer, 2016, 173, 7-12

Chapter 8

Upconversion luminescence of Er^{3+}/Yb^{3+} doped $Sr_5(PO_4)_3OH$ phosphor powders

8.1. Introduction

Strontium hydroxide phosphate ($Sr_5(PO_4)_3OH$) has attracted great interest in modern material due to its outstanding biocompability and bioactivity properties [1]. It has been extensively used as a bone cement filter, in laser materials and also in the development of industrial phosphors [2]. The ionic radius of the Sr^{2+} ion is 1.12 Å and it is similar to ionic radii of many dopant ions such as lanthanides [3,4] that are used as luminescent centres in many light emitting materials (phosphors). Therefore strontium hydroxide phosphate is a promising host for preparation of phosphors including upconversion phosphors due to, among other things, ease of incorporation of lanthanides, short distance between atomic positions that can be occupied by dopant ions such as erbium (Er^{3+}) and ytterbium (Yb^{3+}), and high solubility of ytterbium [5].

In this study, Er^{3+} and Yb^{3+} co-doped $Sr_5(PO_4)_3OH$ phosphors were prepared by urea combustion method. Yb^{3+} was used as a sensitizer of up-converted red photoluminescence from Er^{3+}. Although a single Er^{3+} ion is sufficient to produce upconversion effect, co-doping is usually necessary to enhance its emission (by a transfer of NIR primary excitation energy) since many lanthanides including Er^{3+} have low absorption cross-section leading to a weak emission [6]. Yb^{3+} is usually used as a sensitizer for upconversion photoluminescence due to its larger absorption cross-section in the near infrared (NIR) region (850 – 1050 nm). Er^{3+} ions emits green and red upconverted photoluminescence associated, respectively, with the $^4S_{3/2} \rightarrow {}^4I_{15/2}$ (at ~ 560 nm) and $^4F_{9/2} \rightarrow {}^4I_{15/2}$ (at ~660 nm) transitions when the ions are excited either directly using the NIR radiation or through the NIR excitation of the Yb^{3+} sensitizer [7]. Light energy in wavelengths in the range of 600 – 900 nm (far red to NIR) can penetrate living tissues to a depth about 8 – 10 nm because they are not blocked by water or blood in the body [8, 9]. Therefore these wavelengths can be used in light therapy for treating surface wounds, cuts, scars and cancerous cells. In this paper, we demonstrate enhancement of red emission from Er^{3+} at ~660 nm through sensitization by NIR excitation of Yb^{3+}. In this

paper, we demonstrate enhancement of red emission from Er^{3+} at ~660 nm through sensitization by NIR excitation of Yb^{3+}. In other words, primary excitation energy was harvested by Yb^{3+} and subsequently transferred non-radiatively to Er^{3+} enhancing its red emission. Our red emitting $Sr_5(PO_4)_3OH:Er^{3+},Yb^{3+}$ material can be used in light therapy to activate photosensitizers for treatment of cancer or photodynamic therapy. We evaluated the structure, particle morphology and upconversion luminescence of $Sr_5(PO_4)_3OH:Er^{3+},Yb^{3+}$ phosphor. A mechanism of energy transfer from Yb^{3+} to Er^{3+} is presented. We will not report on the application of our materials in photodynamic therapy.

8.2. Experimental

8.2.1 Preparations

$Sr_5(PO_4)_3OH$ co-doped Er^{3+}/Yb^{3+} phosphor powders were synthesized by combustion method using urea as a fuel. This synthesis method is quick, simple and uses inexpensive raw materials. Lately it is one of the preferred methods to prepare different nanomaterials. The following starting materials with 99% purity were used for the preparation of materials reported in this paper: strontium nitrate (6M $Sr(NO_3)_2{\cdot}4H_2O$), di-ammonium hydrogen phosphate ((4M $NH_4)_2HPO_4$), erbium nitrate ($Er(NO_3)_3{\cdot}5H_2O$), ytterbium nitrate ($Yb(NO_3)_3{\cdot}6H_2O$) with different concentrations of Er^{3+} (in the range of 0.1 – 7 mol %), Yb^{3+} (7 mol %), and Er^{3+}:Yb^{3+} (3:1-7 mol %), and urea ($CO(NH_4)_2$). When a complete reaction is assumed, the theoretical equation for the formation of $Sr_5(PO_4)_3OH$ is given by:

$$15Sr(NO_3)_2{\cdot}4H_2O + 9(NH_4)_2HPO_4 + 16CH_4N_2O = 3Sr_5(PO_4)_3OH + 16CO_2 + 131H_2O + 40N_2 \quad (8.1)$$

All reagents, in stoichiometric amounts, were dissolved in 2 ml of distilled water and the mixture was stirred vigorously for 15 min until a thick homogenous solution was formed. The solution was kept in a furnace maintained at 600 °C. The solution boiled, underwent dehydration and decomposed while generating combustible gases such as CO_2, N_2 and H_2O. The combustion ashes were cooled to room temperature and were ground gently using a pestle and mortar resulting in a fine powder. The materials synthesized were $Sr_5(PO_4)_3OH$, $Sr_5(PO_4)_3OH:Er^{3+}$, $Sr_5(PO_4)_3OH:Yb^{3+}$ and $Sr_5(PO_4)_3OH:Er^{3+},Yb^{3+}$. All the powders were annealed at 800 °C in air.

8.2.2 Measurements

The crystalline structure of the phosphors was analyzed using a Bruker AXS D8 X-ray Diffraction (XRD) with Cu Kα1 radiation (λ = 1.5406Å) in the range of 20 to 60° (2θ). The vibrational bands/modes were analyzed using Fourier Transform Infrared (FTIR) spectrometer. Particle morphology was examined using a Jeol JSM-7800F thermal field emission scanning electron microscope (FE-SEM) coupled with Oxford Aztec 350 X-Max80 Energy x-ray Dispersive Spectroscopy (EDS) which was used to analyse the chemical composition of the phosphors under a vacuum of 9.634×10^{-5} Pa. The absorption and bandgap energy were evaluated using a Perkin Elmer Lambda 950 UV-Vis spectrometer. Upconversion photoluminescence emission was measured by using a photoluminescence (PL) system consisting of a fiber-coupled 980 nm NIR (near infrared) laser as the excitation source, iHR320 Horiba Yvon imaging spectrometer, R943 -02 Hamamatsu Photonics photomultiplier (PMT) detector and a SR830 Standford Research System lock-in amplifier.

8.3. Results and Discussion

8.3.1 Phase analysis

Figure 8.1 shows the XRD pattern of (a) $Sr_5(PO_4)_3OH$, (b) $Sr_5(PO_4)_3OH:Er^{3+}$, (c) $Sr_5(PO_4)_3OH:Yb^{3+}$ and (d) an indexed $Sr_5(PO_4)_3OH:Er^{3+},Yb^{3+}$ phosphor powders with diffraction peaks corresponding to the standard data referenced in International Center for Diffraction Data (ICDD) Card No. 00-033-1348 [10]. The ionic radii of Er^{3+} (1.14 Å) and Yb^{3+} (1.12 Å) are slightly smaller than that of Sr^{2+} (1.18 Å). Therefore Er^{3+}/Yb^{3+} can be easily substituted into Sr^{2+} sites [11]. The narrow and sharp peaks of $Sr_5(PO_4)_3OH$ powder indicate a highly crystalline structure. The diffraction peaks get broadened by doping with different rare earths, suggesting a systematic decrease in the crystallite size. The crystallite sizes of the powders were calculated by using Scherrer equation:

$$D = \frac{k\lambda}{\beta\cos\theta} \tag{8.2}$$

where k is the Scherrer's constant (0.98), λ is the wavelength of X-ray (1.54060 Å), β is the full-width at half maxima, θ is the Bragg angle of the XRD peak. The diffraction peaks (211, 300, 222, 312, and 213) were used to calculate the crystallite size. The calculated average crystallite sizes of $Sr_5(PO_4)_3OH$, $Sr_5(PO_4)_3OH:Er^{3+}$, $Sr_5(PO_4)_3OH:Yb^{3+}$ and $Sr_5(PO_4)_3OH:Er^{3+},Yb^{3+}$ are 47.1, 44.4, 44.3, and 42.1 respectively. The decrease in crystallite

size of phosphor powders suggest that incorporation of dopants suppresses the growth of $Sr_5(PO_4)_3OH$ powder. The peaks corresponding to the crystal plane (210) and (002) were selected to calculate the lattice parameters of the $Sr_5(PO_4)_3OH$, $Sr_5(PO_4)_3OH:Er^{3+}$, $Sr_5(PO_4)_3OH:Yb^{3+}$ and $Sr_5(PO_4)_3OH:Er^{3+},Yb^{3+}$ phosphor powders. The lattice parameters of undoped and doped powders are slightly different, probably due to lattice distortion of the crystal structure [12] caused by incorporation of the dopants.

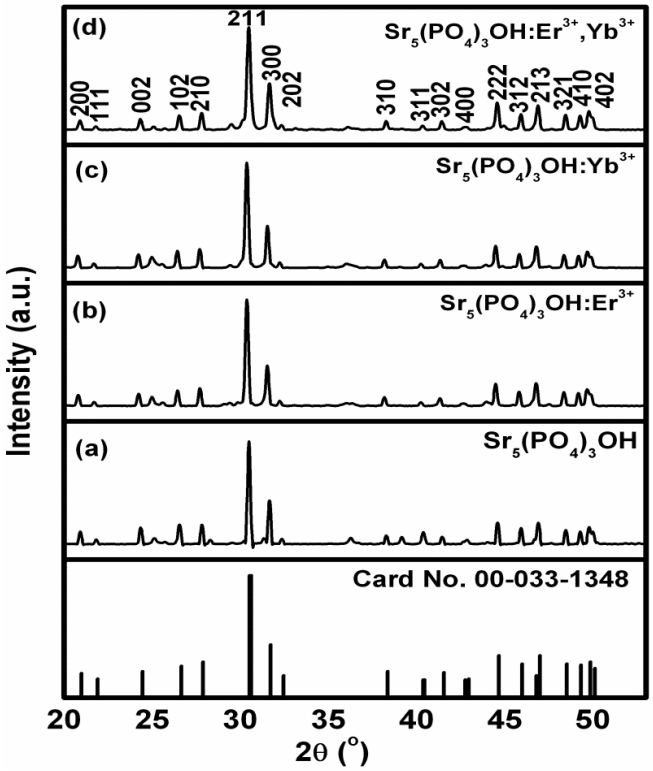

Figure 8.1 XRD results of (a) $Sr_5(PO_4)_3OH$, $Sr_5(PO_4)_3OH:Er^{3+}$ (Er^{3+} = 5 mol%), $Sr_5(PO_4)_3OH:Yb^{3+}$ (Yb^{3+} = 3 mol%) and $Sr_5(PO_4)_3OH:Er^{3+},Yb^{3+}$ (Er^{3+} = 3 mol% and Yb^{3+} = 7 mol%) phosphor powders and ICDD Card 00-033-1348.

Figure 8.2 shows the crystal structure of $Sr_5(PO_4)_3OH$ which was drawn by using the Diamong-Visual Crystal Structure Information System program referenced by Inorganic Crystal Structure Database (ICSD) code number 2855. There are two non-equivalent crystallographic sites of Sr, namely Sr1 anions occupy the 4f Wyckoff position at z = 0.0001 and Sr2 anions occupy 6h Wyckoff positionat z = ¼. The Sr1 and Sr2 atoms are coordinates by six and eight oxygen atoms as the nearest neighbours belonging to the PO_4 group, respectively. P atoms are connected to oxygen atoms in a tetrahedral arrangements. The observed symmetry and reflection condition of $Sr_5(PO_4)_3OH$ is indicative of the P 63/m (176) hexagonal space group with lattice parameters a = 9.745 (1) Å c = 7.265 (1) Å. The

additional crystallographic details are provided in Table 8.1. The atomic coordinates are provided in Table 8.2.

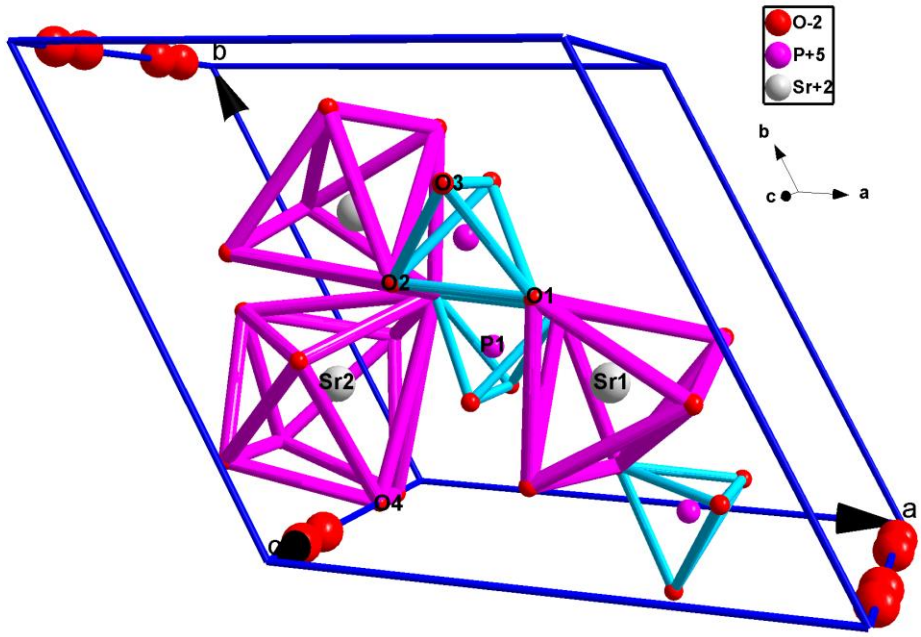

Figure 8.2 Crystal structure of the unit cell of the $Sr_5(PO_4)_3OH$ powder.

Table 8.1. Crystallographic data of $Sr_5(PO_4)_3OH$

Empirical formula	**$Sr_5(PO_4)_3OH$**
Crystal system	Hexagonal
Space-group	P 63/m (176)
Cell parameters	a = 9.745 (1) Å c = 7.265 (1) Å
Cell ratio	a/b = 1.000 b/c = 1.3414 c/a = 0.7455
Cell volume	597.49 (13) $Å^3$
Z	2

Table 8.2. Atomic parameters data of $Sr_5(PO_4)_3OH$.

Atom	Ox.	Wyck.	Site	S.O.F.	x/a	y/b	z/c
O1	-2	6h	m	1.005	0.3329	0.4812	0.25
O2	-2	6h	m	0.999	0.5835	0.4628	0.25
O3	-2	12i	1	1.022	0.3456	0.2611	0.0786
P1	5	6h	m		0.4002	0.3679	0.25
Sr1	2	4f	3	0.9736	0.3333	0.6667	0.0001
Sr2	2	6h	m	0.9824	0.2442	0.9856	0.25
O4	-2	4e	3	0.443	0	0	0.1856

8.3.2 IR analysis

Figure 8.3 shows the FTIR transmission spectra of $Sr_5(PO_4)_3OH$, $Sr_5(PO_4)_3OH:Er^{3+}$ (Er^{3+} = 3 mol%), $Sr_5(PO_4)_3OH:Yb^{3+}$ (Yb^{3+} = 7 mol%) and $Sr_5(PO_4)_3OH:Er^{3+},Yb^{3+}$ (Er^{3+} = 3 mol% and Yb^{3+} = 7 mol%) phosphor powders in the wavenumber range of 400-2000 cm^{-1}. The peak at 592 cm^{-1} revealing two shoulders is assigned to bending vibrations of O-P-O linkage in the HPO_4^{2-} groups indicating the presence of the hydroxyl and phosphate group [13-15]. The little peak at 702 cm^{-1} is assigned to the symmetric stretching mode of the P-O-P group [16-18]. The characteristics band at 858 cm^{-1} is assigned to asymmetric stretching of the P-O-P linked with linear meta-phosphate chain and P-OH group. The band at 1024 cm^{-1} is assigned to the stretching mode of the P-O- group. The band at 1080 cm^{-1} is assigned to the symmetric stretching modes of the P-O-P bonds [16, 17]. The band at 1460 cm^{-1} is assigned to the vibrations of CO_3^{2-} and a carbonate peak was detected because part of PO_4^{3-} groups were replaced by CO_3^{2-} formed by dissolution of CO_2 gas during the synthesis process of the samples [19, 20]. The bending modes of the O-H group at 1704 and 1962 cm^{-1} are assigned to adsorbed H_2O molecules [21]. The splitting of the bands observed may be due to high crystallinity of the powders.

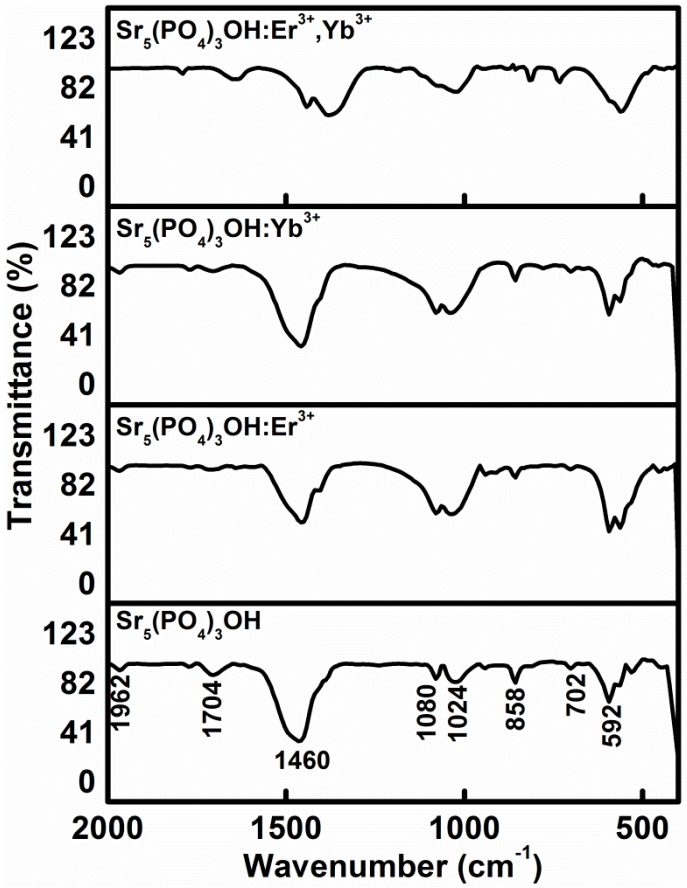

Figure 8.3 FT-IR spectra of $Sr_5(PO_4)_3OH$, $Sr_5(PO_4)_3OH:Er^{3+}$ (Er^{3+} = 3 mol%), $Sr_5(PO_4)_3OH:Yb^{3+}$ (Yb^{3+} = 7 mol%) and $Sr_5(PO_4)_3OH:Er^{3+},Yb^{3+}$ (Er^{3+} = 3 mol% and Yb^{3+} = 7 mol%) phosphor powders.

8.3.3 Particle morphology and chemical composition analysis

Figure 8.4 shows the (a) SEM micrograph and EDS spectrum of the $Sr_5(PO_4)_3OH:Er^{3+},Yb^{3+}$ (Er^{3+} = 3 mol% and Yb^{3+} = 7 mol%) phosphor powder. The SEM micrograph shows that the powder was composed of agglomerated particles with edges forming hexagonal shapes. The agglomeration shows a porous structure resulting from the nature of the combustion reaction associated with the evolution of large volume of gases. The EDS spectrum shown in Figure 8.4 (b) confirms the presence of Sr, P, O, Er and Yb.

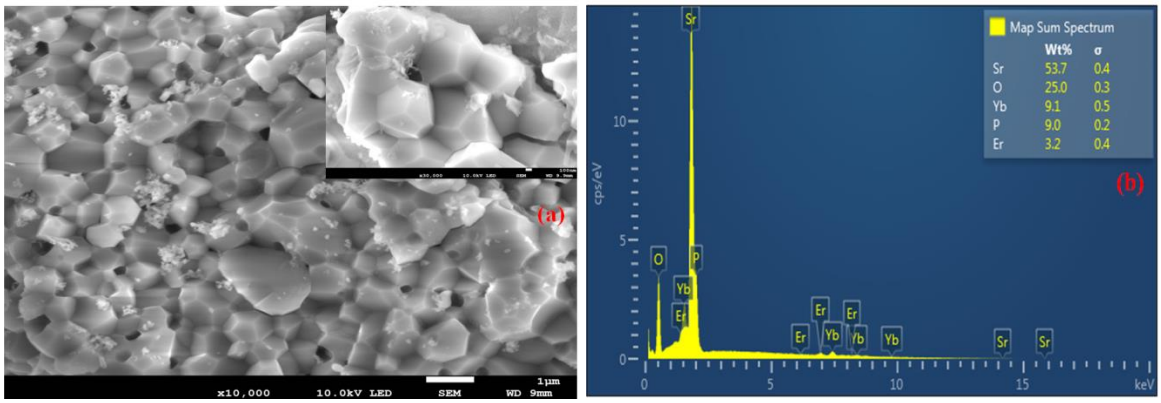

Figure 8.4 (a) SEM image and (b) EDS analysis of $Sr_5(PO_4)_3OH$ co-doped Er^{3+}/Yb^{3+} (Er^{3+} = 3 mol% and Yb^{3+} = 7 mol%) phosphor powder.

8.3.4. UV-Vis diffuse reflectance spectra and Bandgap analysis

Figure 8.5 (a) shows the diffuse reflectance and (b) bandgap energy spectra of (i) $Sr_5(PO_4)_3OH$, (ii) $Sr_5(PO_4)_3OH:Yb^{3+}$ (Yb^{3+} = 7 mol%), $Sr_5(PO_4)_3OH:Er^{3+}$ (Er^{3+} = 3 mol%), and $Sr_5(PO_4)_3OH:Er^{3+},Yb^{3+}$ (Er^{3+} = 3 mol% and Yb^{3+} = 7 mol%) phosphor powders in the wavlength range of 200-1000 nm and energy range of 2-6.3 eV, respectively. The absorption band of $Sr_5(PO_4)_3OH$ at 220 nm is assigned to interband transition of host and other absorption bands at 272 and 379 nm are due to intrinsic defects (e.g vacancies and incidental impurities) in the host [22]. $Sr_5(PO_4)_3OH:Yb^{3+}$ phosphor show the absorption bands at 220 and 978 nm assigned to interband transition of the host and Yb^{3+} ($^2F_{7/2}\rightarrow{}^2F_{5/2}$) transition, respectively [23, 24]. $Sr_5(PO_4)_3OH:Er^{3+}$ phosphor show the absorption bands at various wavelengths, namely 213 nm assigned to interband transition of host, 270 nm assigned to intrinsic defects of the host, and absorption bands at 376, 483, 516, 647 and 978 nm are assigned to $^4I_{15}\rightarrow{}^4G_{11/2}$, $^4I_{15}\rightarrow{}^4F_{7/2}$, $^4I_{15}\rightarrow{}^2H_{11/2}$, $^4I_{15}\rightarrow{}^4F_{9/2}$ and $^4I_{15}\rightarrow{}^4I_{11/2}$ transitions of Er^{3+} ions, respectively [25, 26]. $Sr_5(PO_4)_3OH:Er^{3+},Yb^{3+}$ phosphor shows similar absorption bands with $Sr_5(PO_4)_3OH:Er^{3+}$ assigned to Er^{3+} transitions, the absorption band at 976 nm is associated with the combination of the $^4I_{15}\rightarrow{}^4I_{11/2}$ and $^2F_{7/2}\rightarrow{}^2F_{5/2}$ transitions of Er^{3+} and Yb^{3+} ion, respectively [27]. The optical direct bandgap energy was determined by using Kubelka-Munk function:

$$F(R)=\frac{(1-R)^2}{2R}=\frac{K}{S} \tag{8.3}$$

where *K*, *S*, and *R* are the absorption, scattering and reflection coefficients, respectively [28]. By extrapolating the K-M function to K/S = 0, the bandgap energies of $Sr_5(PO_4)_3OH$, $Sr_5(PO_4)_3OH:Yb^{3+}$, $Sr_5(PO_4)_3OH:Er^{3+}$, and $Sr_5(PO_4)_3OH:Er^{3+},Yb^{3+}$ phosphor powders were

estimated to be 5.1, 5.1, 5.3, and 5.2 eV, respectively. The slight increase in the bandgap (blue shift) was due to electrons filling or moving to a higher energy state. The excess electrons cause an enlargement of the bandgap and the process is known as the Burstein-Moss effect [29].

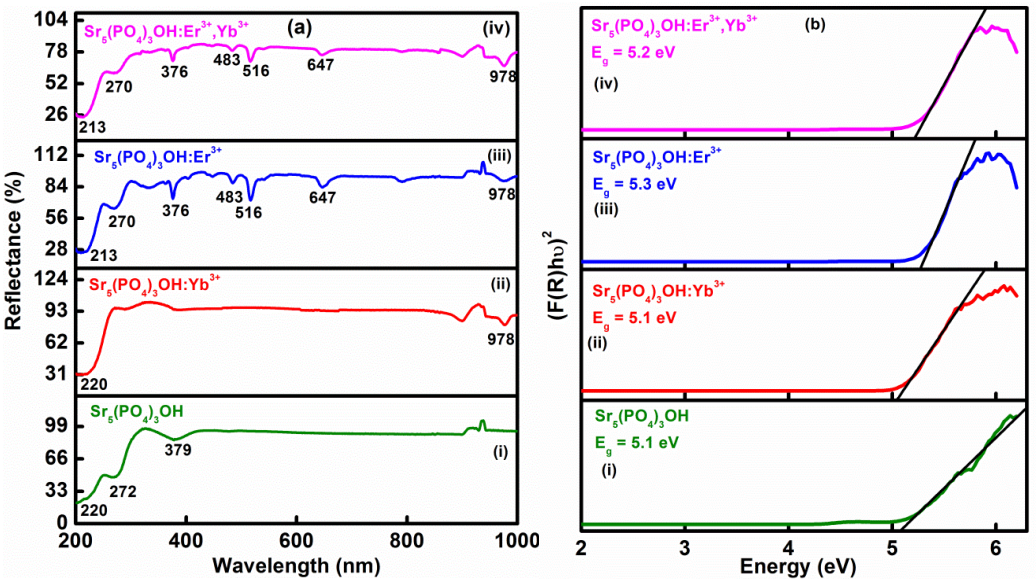

Figure 8.5 (a) Reflectance and (b) bandgap energy spectra of (i) $Sr_5(PO_4)_3OH$, (ii) $Sr_5(PO_4)_3OH:Er^{3+}$ (Er^{3+} = 3 mol%) and (iii) $Sr_5(PO_4)_3OH:Yb^{3+}$ (Yb^{3+} = 7 mol%) and (iv) $Sr_5(PO_4)_3OH:Er^{3+},Yb^{3+}$ (Er^{3+} = 3 mol% and Yb^{3+} = 7 mol%) phosphor powders.

8.3.5. Photoluminescence properties of Er^{3+}/Yb^{3+} co-doped $Sr_5(PO_4)_3OH$ phosphor powder.

Figure 8.6 shows the up-conversion (UC) PL emission spectra of $Sr_5(PO_4)_3OH:Er^{3+}$ (Er^{3+} = 3 mol%), $Sr_5(PO_4)_3OH:Yb^{3+}$ (Yb^{3+} = 7 mol%) and $Sr_5(PO_4)_3OH:Er^{3+},Yb^{3+}$ (Er^{3+} = 3 mol% and Yb^{3+} = 7 mol%) phosphor powders recorded at room when the powders were pumped using the 980 nm laser. Upon the excitation using fiber-coupled 980 nm NIR laser, figure 8.6 (a) exhibit multiple emission bands in the green region and a less intense peak in the red region. The green emission bands are assigned to the 4f→4f electronic transitions from the excited states $^2H_{11/2}$ and $^4S_{3/2}$ to the ground state $^4I_{15/2}$ of Er^{3+} ions [30-32]. The very weak red emission at 668 nm is assigned to $^4F_{9/2}\rightarrow{}^4I_{15/2}$ transition of Er^{3+} ion. The inset labelled (i) shows the maximum photoluminescence intensity versus concentration. The intensity increased with increasing concentrations from 0.1 to 3 mol%, and decreased at higher concentrations due to concentration quenching effects. The inset labelled (ii) shows the

enlarged PL emission in the range of 620-700 nm, showing a similar trend with the peak intensities of the green emission.

Figure 8.6 (b) shows the PL emission spectrum of $Sr_5(PO_4)_3OH:Yb^{3+}$ phosphor powder when excited by 980 nm laser. The strong emission peak is observed at 476 nm and was assigned to the $^2F_{5/2}\rightarrow{}^2F_{7/2}$ transitions of the Yb^{3+} ion [33, 34]. Other minor peaks may be due to impurities from the $Yb(NO_3)_3{\cdot}6H_2O$ precursor used.

Figure 8.6 (c) show the PL emission of $Sr_5(PO_4)_3OH:Er^{3+}Yb^{3+}$ phosphor powders with the Er^{3+} concentration kept constant at (3 mol%) and varying concentrations of Yb^{3+} (1, 3, 5, and 7 mol%). The maximum concentration of Yb^{3+} giving the strongest upconversion emission was 7 mol% in $Sr_5(PO_4)_3OH:Er^{3+}Yb^{3+}$ phosphor powder. The weak green emission peaks were observed at 523, 547 and 550 nm corresponding to $^2H_{11/2} + {}^4S_{3/2}\rightarrow{}^4I_{15/2}$ transition of the Er^{3+} ion. The strong red emission peak with two minor splits was observed at 661 nm, and (651 and 679 nm) correspond to the $^4F_{9/2}\rightarrow{}^4I_{15/2}$ transition of the Er^{3+} ion. The enhancement in the red region was due to energy transfer from the Yb^{3+} to the Er^{3+} ions. The absorption cross-section corresponding to the $^2F_{7/2}\rightarrow{}^2F_{5/2}$ transition of the Yb^{3+} is larger than the absorption cross-section corresponding to the $^4I_{15/2}\rightarrow{}^4I_{11/2}$ transition of Er^{3+}. Er^{3+} and Yb^{3+} ions are excited of $^4I_{11/2}$ and $^2F_{5/2}$ energy states, respectively.

The schematic energy transfer diagram for Er^{3+}/Yb^{3+} is shown in Figure 8.6 (d) due to the effect of multi-phonon vibrations relaxation. Upon co-doping with Yb^{3+}, the 980 nm excitation light is mainly absorbed by Yb^{3+} via $^2F_{7/2}\rightarrow{}^2F_{5/2}$ transitions. The $^2F_{5/2}$ state of Yb^{3+} ion gets highly populated and metastable, thus it decays non-radiatively to the ground state transferring the excited energy to Er^{3+}:$^4I_{11/2}$,$^4I_{13/2}$ states of Er^{3+} ions via a cross relaxation [35, 36]. After the energy transfer (ET1) process the Er^{3+} ions in the ground state are pumped to the $^4I_{11/2}$ state [37]. The energy transfer rate of Yb^{3+}:$^2F_{5/2}\rightarrow Er^{3+}$:$^4I_{11/2}$ (ET1) is demonstrated to be larger than that of Yb^{3+}:$^2F_{5/2}\rightarrow Er^{3+}$:$^4I_{13/2}$ (ET2) because of the energy mismatch of Yb^{3+}:$^2F_{5/2}$ and Er^{3+}:$^4I_{13/2}$ is larger [38]. In the ET1 process, the energy stored in the $^4I_{11/2}$ is excited to the $^4F_{7/2}$ state. The $^4F_{7/2}$ level relaxes non-radiatively to the $^2H_{11/2}$ and $^4S_{3/2}$ states. The $^2H_{11/2}$ + $^4S_{3/2}$ states decay radiatively, giving the emission in the green region. The population of the $^4I_{13/2}$ level is lifted to the $^4F_{9/2}$ state by an energy transfer (ET2) process. The excited $^4F_{9/2}$ state relaxes radiatively to the ground state by emitting in the red region [39]. The red emission becomes dominate and much stronger when the Yb^{3+} ion concentration was above 0.5 mol%, thus resulting in a bright red emission [40].

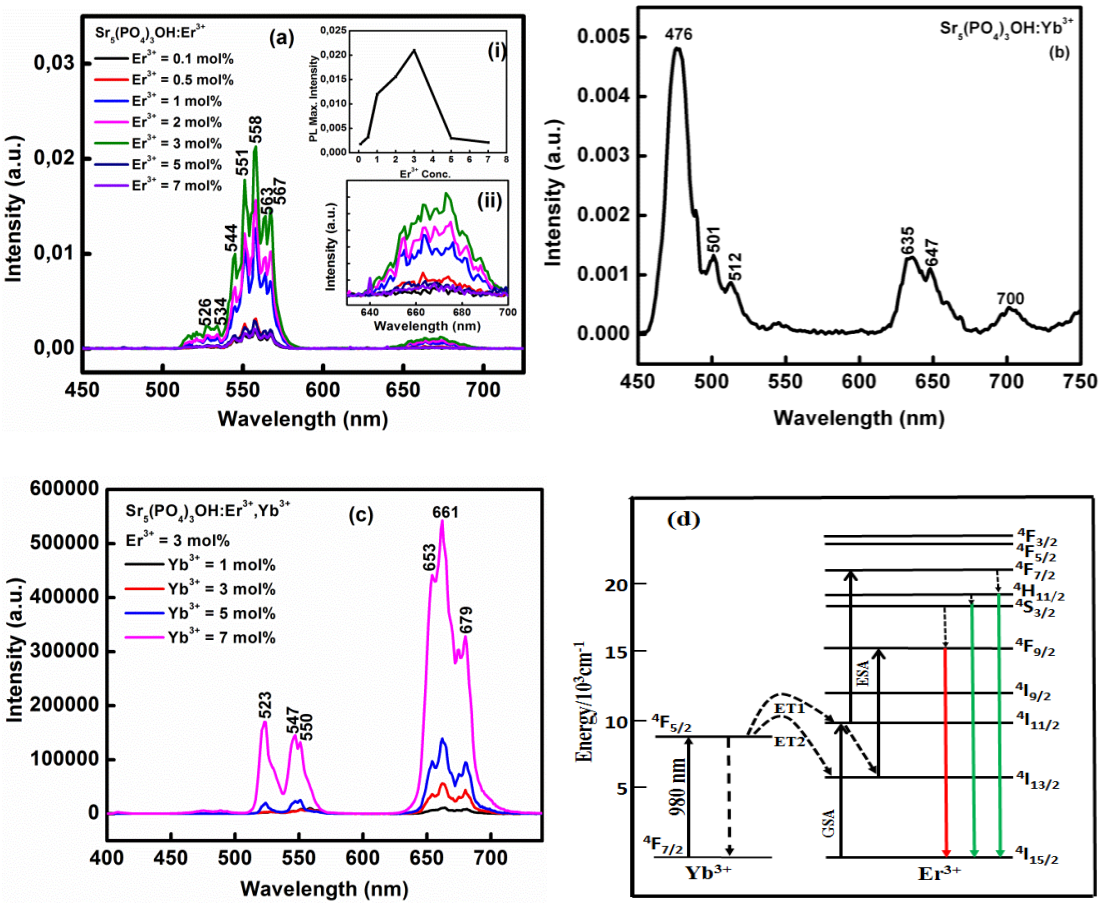

Figure 8.6. Upconversion emission spectra of (a) $Sr_5(PO_4)_3OH:Er^{3+}$ (Er^{3+} = 3 mol%), $Sr_5(PO_4)_3OH:Yb^{3+}$ (Yb^{3+} = 7 mol%) and $Sr_5(PO_4)_3OH:Er^{3+},Yb^{3+}$ (Er^{3+} = 3 mol% and Yb^{3+} = 7 mol%) phosphor powders annealed at 800 ^oC in air.

8.4 Conclusion

$Sr_5(PO_4)_3OH:Er^{3+},Yb^{3+}$ phosphor powders were successfully synthesized by an urea combustion method. The XRD and SEM of $Sr_5(PO_4)_3OH:Er^{3+},Yb^{3+}$ phosphor powders showed a hexagonal structure having agglomerated particles with voids. The absorption bands of $Sr_5(PO_4)_3OH$ at different wavelengths were assigned to interband transition and intrinsic defects of the host. The minor absorption bands were assigned to Er^{3+} and Yb^{3+} transitions. The green and red emission peaks were observed and both were assigned to Er^{3+} ion transition. The enhancement in the red region was due to UC energy transfer from Yb^{3+} to Er^{3+} ions.

References

[1] Z. Ning, Z. Chang, W. Li, C. Sun, J. Zhang, Y. Liu, Chinese Journal of Chemical Engineering, 2012, 20, 89-94

[2] W.M. Lam, C.T. Wong, Z.Y. Li, K.D.K Luk, W.K.Chan, C. Yang, K.Y. Chiu, B. Xu, W.W. Lu, Journal of Crystal Growth, 2007, 306, 129-134

[3] Z. Geng, Z. Cui, Z. Li, S. Zhu, Y. Liang, Y. Liu, X. Li, X. He, X. Yu, R. Wang, X. Yang, Materials and Engineering C, 2016, 58, 467-477

[4] S. Rokidi, P.G. Koutsoukos, Chemical Engineering Science, 2012, 77, 157-164

[5] A. Stefan, O. Toma, S. Georgescu, Journal of Luminescence, 2016, 180, 376

[6] Y.A. Lei, E.L. Meng, C.O. Li, Z. Yong, Nanomedicene, 2011, 6(7), 1273-1288

[7] J. Silver, M.I. Martinez-Rubio, T.G. Ireland, G.R. Fern, R. Witnall, Journal of Physical Chemistry B, 2001, 105, 948-953

[8] C.J.F. Rijcken, J.W. Hofman, F. van Zeeland, W.E. Hennink, C.F. van Nostrum, Journal of Controlled Release, 2007, 124, 144-153

[9] H.M. Ross, J.A. Smelstoys, G.J. Davis, A.S. Kapatkin, F. Del Piero, E. Reineke, H. Wang, T.C. Zhu, T.M. Busch, A.G. Yodh, S.M. Hahn, Journal of Surgical Research, 2006, 135, 323-330

[10] M. Frasnelli, F. Cristofaro, V.M. Sglavo, S. Dire, E. Callone, R. Ceccato, G. Bruni, A.I. Cornaglia, L. Visai, Materials Science and Engineering C, , 2017, 71, 653-662

[11] D.R. Kim, S.W. Park, B.K. Moon, S.H. Park, J.H. Jeong, H. Choi, J.H. Kim, Royal Society of Chemistry, 7, 2017, 1464-1470

[12] J.V. Hernandez, S. Coste, A.G. Murillo, F.C. Romo, A. Kassiba, Journal of Alloys and Compounds, 710, 2017, 355-363

[13] P. Ramakrishnan, S. Nagarajan, V. Thiruvenkatam, T. Palanisami, R. Naidu, M. Mallavarapu, S. Rajendran, Applied Clay Science, 2016, 134, 136-144

[14] O. Kaygili, S. Keser, M. Kom, Y. Eroksuz, S.V. Dorozhkin, T. Ates, I.H. Ozercan, C. Tatar, F. Yakuphanoglu, Material Science and Engineering C, 2015, 55, 538-546

[15] I.Pereiro, C. Rodriguez-Valencia, C. Serra, E.L. Solla, P. Gonazalez, Applied Surface Science, 2012, 258, 9192-9197

[16] S. Babu, M. Seshadri, V.R. Prasad, Y.C. Ratnakaram, Materials Research Bulletin, 2015, 70, 935-944

[17] M.K. Narayana, H.D. Shashikala, M. Manjaiah, Materials Chemistry and Physics, 2015, 152, 127-134

[18] M. Kavitha, R. Surbramanian, R. Narayanan, V. Udhayabanu, Powder Technology, 2014, 253, 129-137

[19] Y. Haung, X. Zhang, H. Zhang, H. Qiao, X. Zhang, T. Jia, S. Han, Y. gao, H. Xiao, H. Yang, Ceramics International, 2017, 43, 992-1007

[20] M.P. Moreira, G.D. de Almeida Soares, J. Dentzer, K. Anselme, L.A. de Sena, A. Kuznetsov, E.A. dos Santos, Materials Science and Engineering C, 2016, 61, 736-743

[21] D. Gopi, S. Ramya, D. Rajeswari, P. Karthikeyan, L. Kavitha, Colloids and Surfaces A: Physicochemical and Engineering Aspects, 2014, 451, 172-180

[22] P.P. Mokoena, I.M. Nagpure, V. Kumar, R.E. Kroon, E.J. Olivier, J.H. Neethling, H.C.Swart, O.M. Ntwaeaborwa, Journal of Physics and Chemistry of Solids, 2014, 75, 998-1003

[23] Z. Huang, M. Yi, H. Gao, Z. Zhang, Y.Mao, Journal of Alloys and Compounds, 2017, 694, 241-245

[24] B. Huang, Y. Zhou, P. Cheng, Z. Zhou, J. Li, W. Jin, Optical Materials, 2016, 60, 341-349

[25] C.R. Kesavulu, H.J. Kim, S.W. Lee, J. Kaewkhao, N. Wantana, S. Kothan, Journal of Alloys and Compounds, 2016, 683, 590-598

[26] C. Wang, H. Xia, Z. Feng, Z. Zhang, D. Jiang, X. Gu, Y. Zhang, B. Chen, H. Jiang, Journal of Alloys and Compounds, 2016, 686, 816-822

[27] Z. Xu, Y. Li, Y. Song, X. Zhang, R. Hu, J. Qiu, Z. Yang, Z. Song, Spectrochimica Acta Part A: Molecular and Biomolecular Spectroscopy, 2017, 177, 111-117

[28] J. Zhang, Z. Hua, S. Wen, Journal of alloys and Compounds, 2015, 637, 70-76

[29] M. Daoudi, F. Hosni, N. Khalifa, I. Dhifallah, K. Farah, A.H. Hamzaoui, Physica B, 2014, 440, 113-117

[30] Y.Y. Ge, Y.J. Zhao, X.Y. Yuan, S.Y. Sun, Y. Z. Zhao, H.P. Zhou, Journal of Alloys and Compounds, 2017, 699, 892-897

[31] K. Upadhyay, R.K. Tamrakar, D.P. Bisen, I.P. Sahu, M. Sahu, Optik, 2016, 127, 3693-3697

[32] C.S. Lim, Infrared Physics & Technology, 2016, 76, 353-359

[33] L. Feng, Y. Wu, Spectrochimica Acta Part A: Molecular and Biomolecular Spectroscopy, 2015, 142, 232-238

[34] A. Kaminska, A. Kozanecki, M.O. Ramirez, L.E. Bausa, G. Boulon, M. Betthinelli, M. Bockowski, A. Suchocki, Journal of Luminscence, 2016, 169, 507-515

[35] D. Hernandez-Pinilla, P. Molina, J.L Plaza, L.E. Bausa, M.O. Ramirez, Optical Materials, 2017, 63, 173-178

[36] X.Q. Guo, Y.Yan, H.C. Zhang, Y. Han, J.J. Song, Ceramics International, 2016, 42, 8738-8743

[37] H. Lu, Y. Gao, H. Hao, G. Shi, D. Li, Y. Song, Y. Wang, X. Zhang, Journal of Luminescence, 2017, 186, 34-39

[38] C. Wang, H. Xia, Z. Feng, Z. Zhang, D. Jiang, X. Gu, Y. Zhang, B. Chen, H. Jiang, Journal of Alloys and Compounds, 2016, 686, 816-822

[39] A.K. Soni, V.K. Rai, M.K. Mahata, Materials Research Bulletin, 2017, 89, 116-124

[40] D. Ramachari, D. Esparza, T. Lopez-Luke, V.H. Romero, L. Perez-Mayen, E. De la Rosa, C.K. Jayasankar, Journal of Alloys and Compounds, 2017, 698, 433-441

Chapter 9

Synthesis and upconversion properties of Eu^{3+}/Yb^{3+} co-doped $Sr_5(PO_4)_3OH$ nanoparticles and their applications in photodynamic therapy

9.1. Introduction

Lanthanide-doped nanocrystals are becoming increasingly important in applications of solar cells, bioimaging, sensors, displays, photocatalysis and photoisomerization [1]. The upconversion luminescence processes of lanthanide ions rely on the abundant f-electron configurations of lanthanide ions at the required intermediate excitation states. They also have the ability to transform two or more sub-bandgap NIR photons into one usable above-bandgap photon. Through the decades of investigations, researchers have found out that most efficient upconversion luminescence (UCL) are from the following lanthanides: Yb^{3+} and $Er^{3+}/Ho^{3+}/Tm^{3+}$ in which energy transfer upconversion mechanism plays a dominant role [2, 3]. Among the lanthanides elements europium (Eu^{3+}) is usually used as a red emitting lanthanide, but it has never been considered an UCL ion in the regime of NIR excitation due to that fact that it cannot be directly excited by NIR. It has been reported that the red UC emission of Eu^{3+} ion under NIR excitation can be obtained by co-doping with infrared sensitizer (energy donor) such as Yb^{3+} ion. Yb^{3+} has a large absorption cross-section of the $^2F_{7/2} \rightarrow {}^2F_{5/2}$ transition, which is almost resonant with the specific excited electronic states of some rare earth ions [4]. The red UCL of Eu^{3+} is due to cooperative energy transfer from the pairs of Yb^{3+} ions to single Eu^{3+} [5].

In this chapter, we report the energy upconversion of Eu^{3+} due to cooperative energy transfer from a pair of Yb^{3+} ions in $Sr_5(PO_4)_3OH$ system synthesized by urea combustion process. We evaluated the structure, particle morphology and upconversion luminescence of Er^{3+}/Yb^{3+} co-doped $Sr_5(PO_4)_3OH$ phosphor. A mechanism of energy transfer from Yb^{3+} to Eu^{3+} is presented.

9.2. Experimental

9.2.1 Preparation

$Sr_5(PO_4)_3OH$ co-doped Eu^{3+}/Yb^{3+} phosphor powders were synthesized by combustion method using urea as a fuel. This synthesis method is quick, simple and uses inexpensive raw materials. Lately it is one of the preferred methods to prepare different nanomaterials. The following starting materials with 99% purity were used for the preparation of materials reported in this paper: strontium nitrate (6M $Sr(NO_3)_2{\cdot}4H_2O$), di-ammonium hydrogen phosphate ((4M $NH_4)_2HPO_4$), europium nitrate ($Eu(NO_3)_3{\cdot}5H_2O$), ytterbium nitrate ($Yb(NO_3)_3{\cdot}6H_2O$) with different concentrations of Eu^{3+} (in the range of 1 – 7 mol %), Yb^{3+} (7 mol %), and Eu^{3+}:Yb^{3+} (3:7 mol %), and urea ($CO(NH_4)_2$). When a complete reaction is assumed, the theoretical equation for the formation of $Sr_5(PO_4)_3OH$ is given by:

$$15Sr(NO_3)_2{\cdot}4H_2O + 9(NH_4)_2HPO_4 + 16CH_4N_2O = 3Sr_5(PO_4)_3OH + 16CO_2 + 131H_2O + 40N_2 \quad (1)$$

All reagents, in stoichiometric amounts, were dissolved in 2 ml of distilled water and the mixture was stirred vigorously for 15 min until a thick homogenous solution was formed. The solution was kept in a furnace maintained at 600 °C. The solution boiled, underwent dehydration and decomposed while generating combustible gases such as CO_2, N_2 and H_2O. The combustion ashes were cooled to room temperature and were ground gently using a pestle and mortar resulting in a fine powder. The materials synthesized were $Sr_5(PO_4)_3OH$, $Sr_5(PO_4)_3OH:Eu^{3+}$, $Sr_5(PO_4)_3OH:Yb^{3+}$ and $Sr_5(PO_4)_3OH:Eu^{3+},Yb^{3+}$. All the powders were annealed at 800 °C in air.

9.2.2 Measurements

The crystalline structure of the phosphors was analyzed using a Bruker AXS D8 X-ray Diffraction (XRD) with Cu Kα1 radiation (λ = 1.5406Å) in the range of 20 to 50° (2θ). The vibrational bands/modes were analyzed using Fourier Transform Infrared (FTIR) spectrometer. Particle morphology was examined using a Jeol JSM-7800F thermal field emission scanning electron microscope (FE-SEM) coupled with Oxford Aztec 350 X-Max80 Energy x-ray Dispersive Spectroscopy (EDS) which was used to analyse the chemical composition of the phosphors under a vacuum of 9.634×10^{-5} Pa. The absorption and bandgap energy were evaluated using a Perkin Elmer Lambda 950 UV-Vis spectrometer. The photoluminescence emission was measured by using and Cary eclipse fluorescence with monochromatized xenon lamp and photoluminescence (PL) system consisting of a fibre-

coupled 980 nm NIR (near infrared) laser as the excitation source, iHR320 Horiba Yvon imaging spectrometer, R943 -02 Hamamatsu Photonics photomultiplier (PMT) detector and a SR830 Standford Research System lock-in amplifier.

9.3. Results and Discussion

9.3.1 Phase analysis

Figure 10.1 show the XRD pattern of $Sr_5(PO_4)_3OH$ powder annealed at 800 ^oC in air. The difraction pattern was taken in th 2θ range of 20-55 degrees. All the diffraction patterns match with the standard data referenced by ICDD Card No. 00-033-1348. The crystallite size was calculated from full width at half maximum (FWHM) value of all indexed peaks using Scherrer equation:

$$D = \frac{k\lambda}{\beta \cos\theta} \tag{9.2}$$

where k is the Scherrer's constant (0.98), λ is the wavelength of X-ray (1.54060 Å), β is the full-width at half maximum, θ is the Bragg angle of the XRD peak. The average crystallite size calculated was 43 ± 2 nm. The sharp and narrow peaks confirm the crystallinity of the powder.

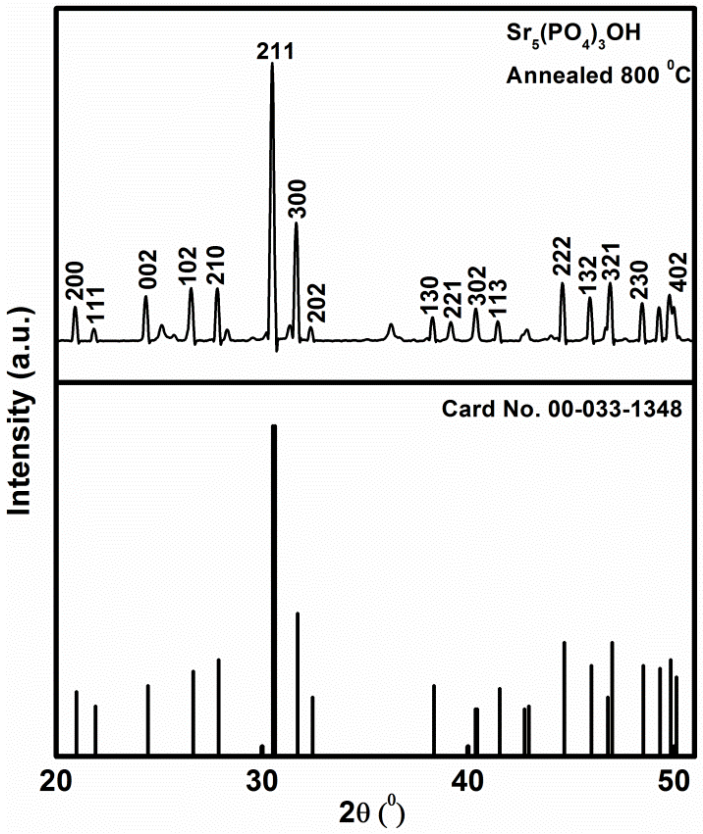

Figure 9.1 XRD results of a pure $Sr_5(PO_4)_3OH$ powder and ICDD Card 00-033-1348.

9.3.2 IR analysis

Figure 9.2 shows the FTIR transmission spectra of $Sr_5(PO_4)_3OH$, $Sr_5(PO_4)_3OH:Eu^{3+}$ (Eu^{3+} = 3 mol%), $Sr_5(PO_4)_3OH:Yb^{3+}$ (Yb^{3+} = 7 mol%) and $Sr_5(PO_4)_3OH:Eu^{3+},Yb^{3+}$ (Eu^{3+} = 3 mol% and Yb^{3+} = 7 mol%) phosphor powders in the wavenumber range of 400-2000 cm^{-1}. The peak at 591 cm^{-1} with two shoulders is assigned to bending modes of O-P-O linkage in the HPO_4^{2-} groups indicating the presence of the hydroxyl and phosphate group [6-8]. The small peak at 702 cm^{-1} is assigned to the symmetric stretching mode of the P-O-P group [9-11]. The characteristics band at 858 cm^{-1} is assigned to asymmetric stretching of the P-O-P linked with linear meta-phosphate chain and P-OH group [12]. The band at 1024 cm^{-1} is assigned to the stretching mode of the P-O- group [13]. The band at 1080 cm^{-1} is assigned to the symmetric stretching modes of the P-O-P bonds [9, 10]. The band at 1460 cm^{-1} is assigned to the vibrations of CO_3^{2-} and a carbonate peak was detected because part of PO_4^{3-} groups were replaced by CO_3^{2-} formed by dissolution of CO_2 gas during the synthesis process of the samples [14-16]. The bending modes of the O-H group at 1704 and 1962 cm^{-1} are assigned to adsorbed H_2O molecules [17]. The splitting of the bands observed may be due to high crystallinity of the powders.

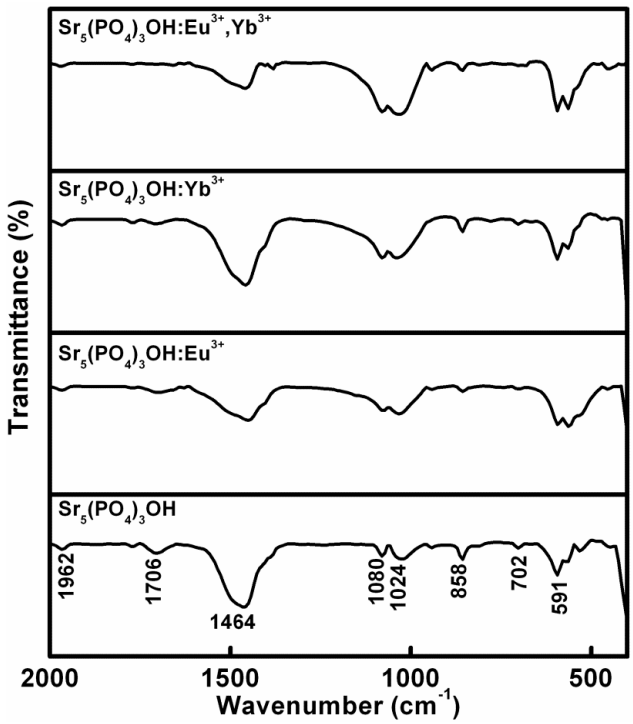

Figure 9.2 FT-IR spectra of $Sr_5(PO_4)_3OH$, $Sr_5(PO_4)_3OH:Eu^{3+}$ (Eu^{3+} = 3 mol%), $Sr_5(PO_4)_3OH:Yb^{3+}$ (Yb^{3+} = 7 mol%) and $Sr_5(PO_4)_3OH:Eu^{3+},Yb^{3+}$ (Eu^{3+} = 3 mol% and Yb^{3+} = 7 mol%) phosphor powders.

9.3.3 Particle morphology and chemical composition analysis

Figure 9.3 show the (a) SEM image, (b) EDS spectrum and (c) EDS mapping of $Sr_5(PO_4)_3OH$ co-doped Eu^{3+}/Yb^{3+} phosphor powder annealed at 800 ^oC in air. The powder has a network of particles with irregular shapes with small bright particles encrusted on the surface of the bigger particles. The small bright particles may be the incorporated rare earths (Eu^{3+} and Yb^{3+}) ions. The SEM image was taken using backscattered electron detector. The particles containing heavy atoms in backscattered electron detector are stronger than light particles and they appear brighter [18]. Figure 9.3 (b) show the EDS spectrum of $Sr_5(PO_4)_3OH:Eu^{3+},Yb^{3+}$phosphor powder confirming all the elements present in the material. The inset in the middle shows the SEM image and the position where the EDS analysis was performed marked with S3 and S4. The bar graph next to it compares the weight % of each element present at the chosen positions. The weight % of rare earths elements (Eu^{3+} and Yb^{3+}) in S3 is 3 and 9%, and in S4 Eu^{3+} and Yb^{3+} is 8 and 16% respectively. Thus, confirm that small bright particles are dominated by Eu^{3+} and Yb^{3+}, while darker particles are dominated by Sr, O, and Ir. The elemental mapping in Figure 9.3 (c) shows that the elements are uniformly dispersed on the surface of the $Sr_5(PO_4)_3OH:Eu^{3+},Yb^{3+}$ phosphor powder. The Ir (Iridium =

1.977 keV) element present in the spectra and mapping is overlapping with the electron energy of P (Phosphorus = 2.013 keV).

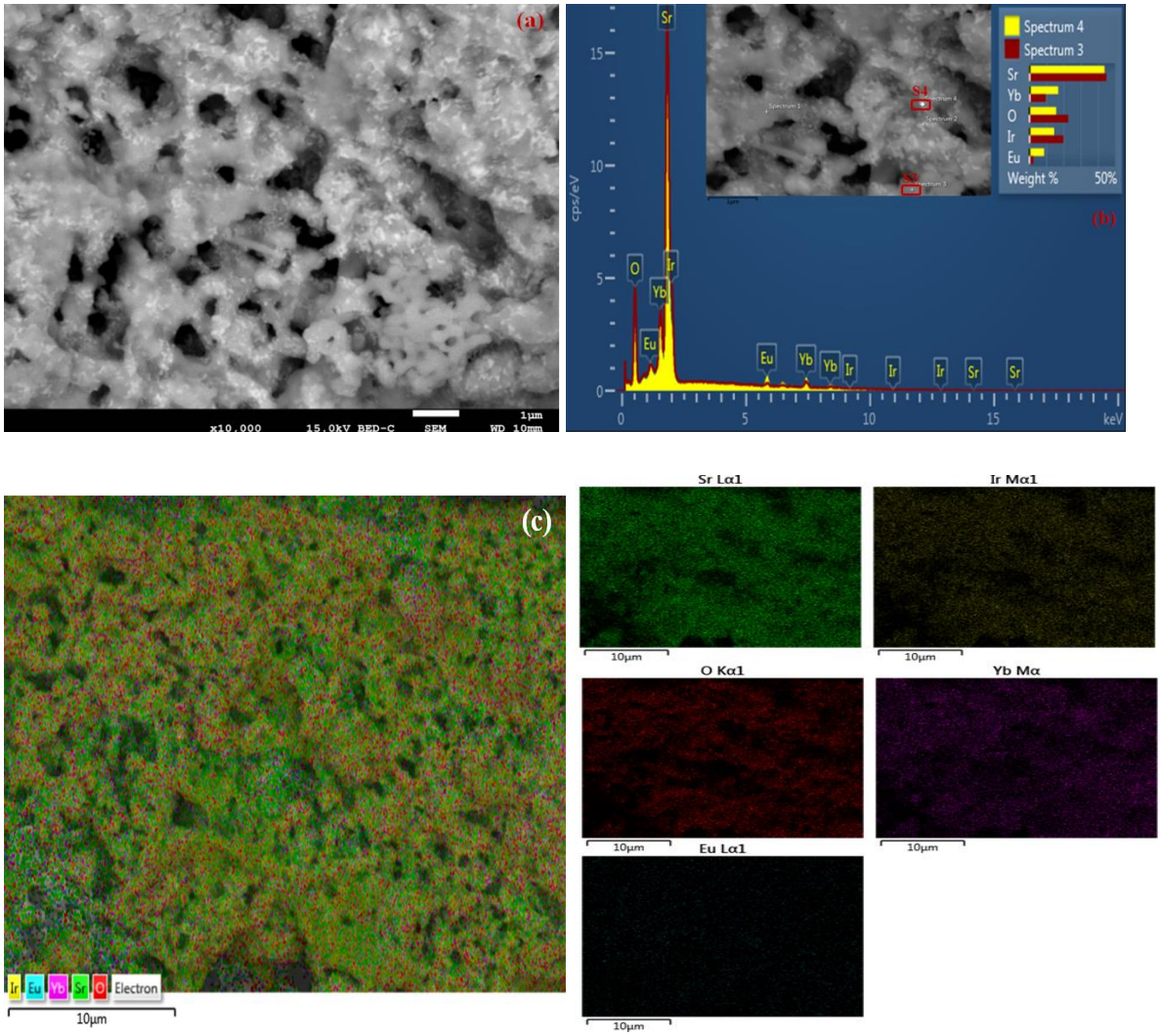

Figure 9.3 (a) SEM image, (b) EDS spectrum and (c) EDS mapping of $Sr_5(PO_4)_3OH$ co-doped Eu^{3+}/Yb^{3+} (Eu^{3+} = 3 mol% and Yb^{3+} = 7 mol%) phosphor powder.

9.3.4. UV-Vis diffuse reflectance spectra and Bandgap analysis

Figure 9.4 (a) shows the diffuse reflectance and (b) bandgap energy spectra of (i) $Sr_5(PO_4)_3OH$, (ii) $Sr_5(PO_4)_3OH:Yb^{3+}$ (Yb^{3+} = 7 mol%), $Sr_5(PO_4)_3OH:Eu^{3+}$ (Eu^{3+} = 3 mol%), and $Sr_5(PO_4)_3OH:Eu^{3+},Yb^{3+}$ (Eu^{3+} = 3 mol% and Yb^{3+} = 7 mol%) powder phosphors in the wavlength range of 200-1000 nm and energy range of 2-6.3 eV, respectively. The absorption band of $Sr_5(PO_4)_3OH$ at 221 nm is assigned to interband transition of host and other absorption bands at 273 and 378 nm are probably due to intrinsic defects (e.g. vacancies and incidental impurities) in the host [19]. $Sr_5(PO_4)_3OH:Yb^{3+}$ phosphor show the absorption bands at 221 and 978 nm assigned to interband transition of the host and Yb^{3+} ($^2F_{7/2}\rightarrow{}^2F_{5/2}$)

transition, respectively [20, 21]. Figure 9.4.a (iii) shows the absorption peaks at 221 and 273 nm attributed to host transitions (interband transition and defects). There are minor absorption peaks observed at 391 and 458 nm which are attributed to $^7F_0 \rightarrow {}^5L_6$, and $^7F_0 \rightarrow {}^5D_2$, transitions of Eu^{3+} ion, respectively [22, 23]. $Sr_5(PO_4)_3OH:Eu^{3+},Yb^{3+}$ system shows similar trend of absorption peaks at 221, 273 and 378 nm attributed host transitions (interband transitions and defects), 459 nm attributed to Eu^{3+} and 978 nm attributed to Yb^{3+} transitions.

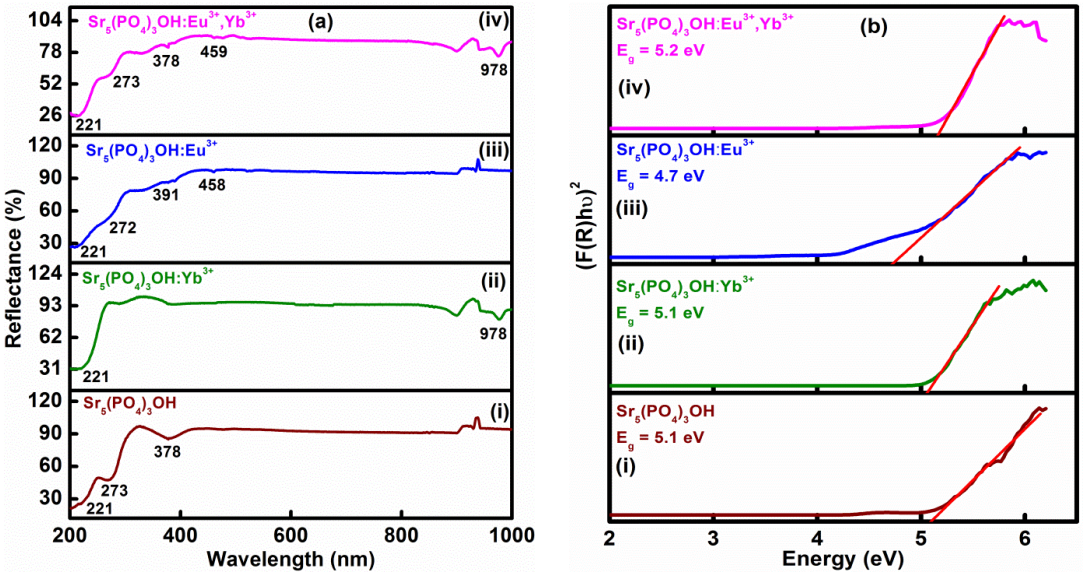

Figure 9.4 (a) Reflectance and (b) bandgap energy spectra of (i) $Sr_5(PO_4)_3OH$, (ii) $Sr_5(PO_4)_3OH:Eu^{3+}$ (Eu^{3+} = 3 mol%) and (iii) $Sr_5(PO_4)_3OH:Yb^{3+}$ (Yb^{3+} = 7 mol%) and (iv) $Sr_5(PO_4)_3OH:Eu^{3+},Yb^{3+}$ (Eu^{3+} = 3 mol% and Yb^{3+} = 7 mol%) phosphor powders.

9.3.5. Photoluminescence properties of Eu^{3+}/Yb^{3+} co-doped $Sr_5(PO_4)_3OH$ phosphor powder.

Figure 9.5 (a) shows the PL excitation and emission spectra of Eu^{3+} (1-7 mol%) doped $Sr_5(PO_4)_3OH$ phosphor powders, measured by Varian cary eclipse. The broad excitation band observed at 245 nm is attributed to charge-transfer band (CTB), originating from the transition of a ligand O^{2-} 2p orbital to the empty states at about $4f^6$ configuration of Eu^{3+} (Eu^{3+}-O^{2-} transition) [24, 25]. The narrow excitation peaks within the 4*f* electron configuration at 361, 380, 395, 412, 464 and 529 nm are assigned to $^7F_0 \rightarrow {}^5D_4$, $^7F_0 \rightarrow {}^5G_2$, $^7F_0 \rightarrow {}^5L_6$, $^7F_0 \rightarrow {}^5D_3$, $^7F_0 \rightarrow {}^5D_2$, and $^7F_0 \rightarrow {}^5D_1$ transitions of Eu^{3+} ions, respectively [26, 27]. The emission spectra upon 248 nm excitation, displays four emission peaks centered at 591, 613, 652, and 699 nm assigned to the $^5D_0$ level to $^7F_1$, $^7F_2$, $^7F_3$, and $^7F_4$, transitions of Eu^{3+} respectively [28-31] .

Figure 9.5 (b) shows the upconversion luminescence spectrum of $Sr_5(PO_4)_3OH:Yb^{3+}$ phosphor pumped at 980 nm. The prominent emission peak is observed at 476 nm with minor emission peaks in the range of 522-700 nm, the peaks are assigned to $^2F_{5/2} \rightarrow {}^2F_{7/2}$ transitions of Yb^{3+} ion and other additional peaks may be due to the precursors.

Figure 9.5 (c) shows the emission spectrum of $Sr_5(PO_4)_3OH:Eu^{3+},Yb^{3+}$ phosphor upon 980 nm laser excitation. Upon co-doping with Yb^{3+}, the upconversion emission is observed. This indicates that the Eu^{3+} ions are excited due to the presence of Yb^{3+} ions. The emission peaks observed at ~521, 547, 588, 614, 658 and 703 nm are attributed to $^5D_0 \rightarrow {}^7F_{j\ (j=1,2,3,4)}$ transitions of Eu^{3+} ion. The strongest emission peak is observed at 658 nm assigned to $^5D_0 \rightarrow {}^7F_3$ transition of Eu^{3+} ion [32, 33]. This is due to energy transfer upconversion from Yb^{3+} to Eu^{3+}. Yb^{3+} act as a sensitizer for Eu^{3+} via cooperative energy transfer process.

Thus, a cooperative energy transfer from Yb^{3+} ion pair to a single Eu^{3+} ion can occur, by fast non-radiative relaxation to the metastable $^5D_0$ state, and the red Eu^{3+} emission is observed [34]. The energy transfer is through dipole-dipole interaction involving pairs of Yb^{3+} and the state of Eu^{3+} ions. Two Yb^{3+} ions are first excited from $^2F_{7/2}$ to $^2F_{5/2}$ and transfer their total energy to $^5D_1$ state of Eu^{3+} ion. Eu^{3+} ion in the $^5D_1$ level relaxes non-radiatively to luminescent level $^5D_0$, followed by radiative transition from between different energy states $^5D_0$ and ground state). The detailed energy transfer process between Eu^{3+} and Yb^{3+} is explained in chapter 5. The schematic diagram of energy transfer between Eu^{3+} and Yb^{3+} is illustrated by figure 9.5 (d).

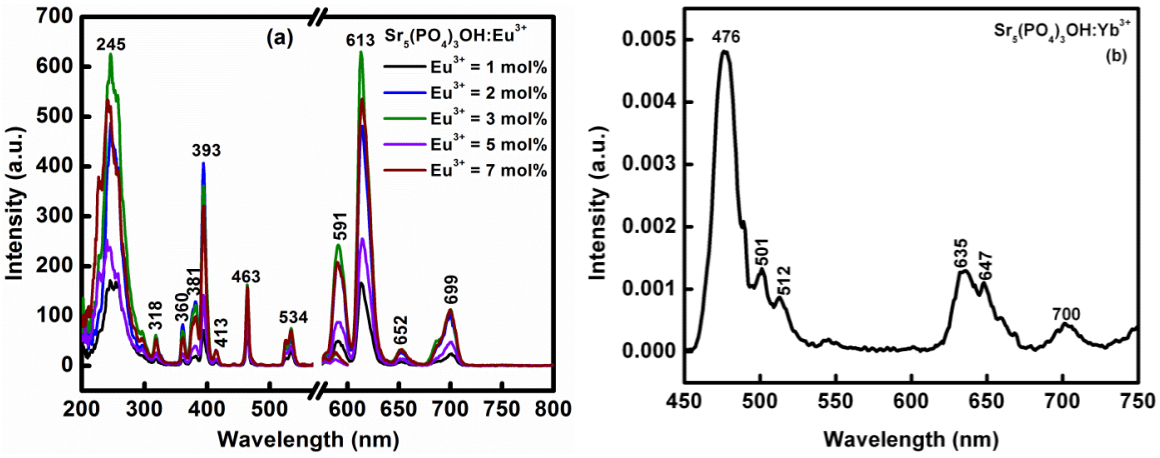

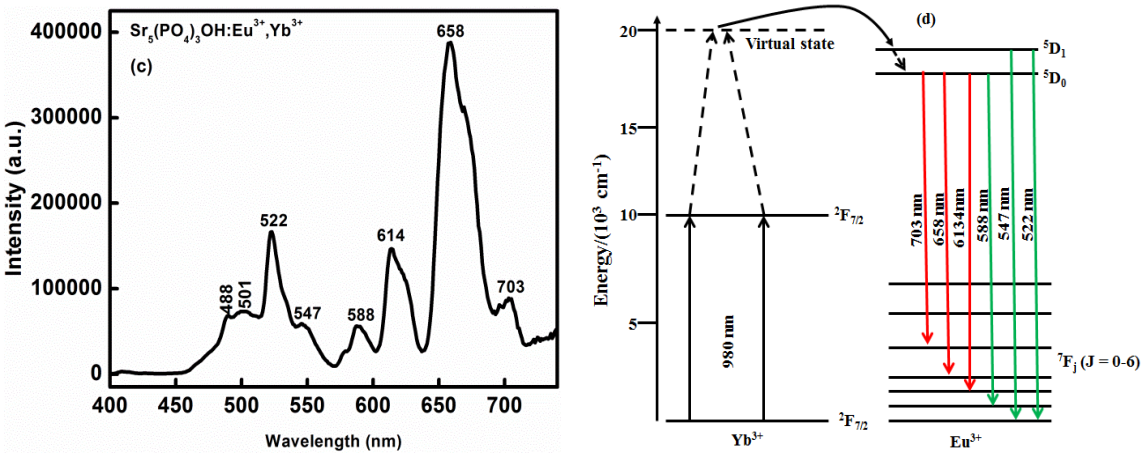

Figure 9.5. PL emission spectra of (a) $Sr_5(PO_4)_3OH:Eu^{3+}$ (Eu^{3+} = 3 mol%), (b) $Sr_5(PO_4)_3OH:Yb^{3+}$ (Yb^{3+} = 7 mol%), (c) $Sr_5(PO_4)_3OH:Eu^{3+},Yb^{3+}$ (Eu^{3+} = 3 mol% and Yb^{3+} = 7 mol%) phosphor powders annealed at 800 ^oC in air and (d) energy transfer mechanism of Eu^{3+}/Yb^{3+}.

9.4 Conclusion

$Sr_5(PO_4)_3OH:Eu^{3+},Yb^{3+}$ phosphor powders were successfully synthesized by urea combustion method. The XRD characterization confirmed the formation of a single phase of $Sr_5(PO_4)_3OH$ by matching with standard data referenced by ICDD Card No. 00-033-1348. Furthermore, The EDS spectrum comfirmed all the elements present in the materials. For $Sr_5(PO_4)_3OH:Eu^{3+}$ system, the emission peaks were observed in the range 591-699 nm and assigned to Eu^{3+} transitions. Upon co-doping with Yb^{3+}, the red emission peak at 658 nm was enhanced due to energy transfer from Yb^{3+} to Eu^{3+}. The enhanced red emission can be used to activate the photosensitizers for treatment of cancerous cells by photodynamic therapy.

References

[1] L. Song, A. Wei, Z. Li, J. Liu, Y. Zhao, Z. Xiao, Materials Research Bulletin, 2017, 88, 1-8

[2] X. Liu, Y. li, T. Aidilibike, J. Guo, W. Di, W. Qin, Journal of Luminescence, 2017, 185, 247-250

[3] A. Tyminski, T. Grzyb, Journal of Luminesence, 2017, 181, 411-420

[4] M. Puchalska, E. Zych, M. Sobczyk, A. Watras, P. Deren, Materials Chemistry and Physics, 2014, 147, 304-310

[5] P.A. Loiko, G.E. Rachkovskaya,G.B. Zakharevich, A.A. Kornienko, E.B. Dunina, A.S. Yasukevich, K.V. Yumashev, Journal of Non-Crystalline Solids, 2014, 392-393, 39-44

[6] P. Ramakrishnan, S. Nagarajan, V. Thiruvenkatam, T. Palanisami, R. Naidu, M. Mallavarapu, S. Rajendran, Applied Clay Science, 2016, 134, 136-144

[7] O. Kaygili, S. Keser, M. Kom, Y. Eroksuz, S.V. Dorozhkin, T. Ates, I.H. Ozercan, C. Tatar, F. Yakuphanoglu, Material Science and Engineering C, 2015, 55, 538-546

[8] I.Pereiro, C. Rodriguez-Valencia, C. Serra, E.L. Solla, P. Gonazalez, Applied Surface Science, 2012, 258, 9192-9197

[9] S. Babu, M. Seshadri, V.R. Prasad, Y.C. Ratnakaram, Materials Research Bulletin, 2015, 70, 935-944

[10] M.K. Narayana, H.D. Shashikala, M. Manjaiah, Materials Chemistry and Physics, 2015, 152, 127-134

[11] M. Kavitha, R. Surbramanian, R. Narayanan, V. Udhayabanu, Powder Technology, 2014, 253, 129-137

[12] L. He, G. Dong, C. Deng, Ceramics International, 2016, 42, 11918-11923

[13] V. Sanyal, C.R. Raja, Journal of Non-Crystalline Solids, 2016, 445-446, 81-87

[14] Y. Haung, X. Zhang, H. Zhang, H. Qiao, X. Zhang, T. Jia, S. Han, Y. gao, H. Xiao, H. Yang, Ceramics International, 2017, 43, 992-1007

[15] M.P. Moreira, G.D. de Almeida Soares, J. Dentzer, K. Anselme, L.A. de Sena, A. Kuznetsov, E.A. dos Santos, Materials Science and Engineering C, 2016, 61, 736-743

[16] M. Bianchi, L.D. Esposti, A. Ballardini, F. Liscio, M. Berni, A. Gambardella, S.C.G. Leeuwenburgh, S. Sprio, A. Tampieri, M. Iafisco, Surface & Coatings Technology, 2017, 319, 191-199

[17] D. Gopi, S. Ramya, D. Rajeswari, P. Karthikeyan, L. Kavitha, Colloids and Surfaces A: Physicochemical and Engineering Aspects, 2014, 451, 172-180

[18] P.P. Mokoena, M. Gohain, B.C.B bezuidenhoudt, H.C. Swart, O.M. Ntwaeaborwa, Journal of Luminescence, 2014, 155, 288-292

[19] P.P. Mokoena, I.M. Nagpure, V. Kumar, R.E. Kroon, E.J. Olivier, J.H. Neethling, H.C.Swart, O.M. Ntwaeaborwa, Journal of Physics and Chemistry of Solids, 2014, 75, 998-1003

[20] Z. Huang, M. Yi, H. Gao, Z. Zhang, Y.Mao, Journal of Alloys and Compounds, 2017, 694, 241-245

[21] B. Huang, Y. Zhou, P. Cheng, Z. Zhou, J. Li, W. Jin, Optical Materials, 2016, 60, 341-349

[22] J. Chen, W. Zhao, J. Wang, N. Wang, Y. Meng, J. He, X. Zhang, Ceramics International, 2015, 41, 11945-11952

[23] S.S. Barbara, N. Pawlik, A.S. Swinarew, W.A. Pisarski, Journal of Luminescence, 2015, 166, 356-360

[24] C. Shivakumara, R. Saraf, S. Behera, N. Dhananjaya, H. Nagabhushana, Spectrochimica Acta Part A: Molecular and Biomolecular Spectroscopy, 2015, 151, 141-148

[25] B. Han, P. Li, J. Zhang, J. Zhang, Y. Xue, X. Suo, Q. Huang, Y. Feng, H. Shi, Materials Letters, 2015, 158, 208-210

[26] K.N. Kumar, R. Padma, L. Vijayalakshmi, J.S.M. Nithya, M. Kang, Journal of Luminescence, 2017, 182, 208-219

[27] V. Naresh, K. Gupta, C.P. Reddy, B.S. Ham, Spectrochimica Acta Part A: Molecular and Biomolecular Spectroscopy, 2017, 175, 43-50

[28] G. Chen, F. Wang, J. Yu, H. Zhang, X. Zhang, Journal of Molecular Structure, 2017, 1128, 1-4

[29] Y. Zeng, K. Qiu, Z. Yang, Y. Bu, W. Zhang, J. Li, Ceramics International, 2017, 43, 830-834

[30] P.A. Loiko, O.S. Dymshits, I.P. Alekseeva, A.A. Zhilin, M.Ya, Tsenter, E.V. Vilejshikova, K.V. Bogdanov, X. Mateos, K.V. Yumashev, Journal of Luminescence, 2016, 179, 64-73

[31] W.J. Zhang, X.B. Li, L.J. Wu, Y.Y. Yu, X.Z. Wang, S.Q. Liu, Z. Wang, W.C. Wang, Y. Liu, Physica B, 2017, 508, 22-26

[32] H. Rahimian, H. Mokhtari, S.P. Shirmardi, Journal of Luminescence, 2017, 187, 535-539

[33] J.G. Mendoza, E.G. Garcia, J.C.G. Olguin, E. Montes, G.T. Jasso, M. Garcia-Hipolito, C. Falcony-Guajardo, Journal of Luminescence, 2017, 188, 394-399

[34] H. Xia, J. Feng, Y. Ji, Y. Sun, Y. Wang, Z. Jia, C. Tu, Journal of Quantitative Spectroscopy & Radiative Transfer, 2016, 173, 7-12

Chapter 10

Evaluation of photodynamic therapy activity of phosphate based upconversion nanoparticles against human breast adenocarcinoma cells

10.1. Introduction

Phosphates (PO_4^{3-}) are generating a significant interest in various technological applications due their exclusive properties such as high thermal expansion coefficient, low viscosity, UV transmission, and electrical conduction. They have been used in multiple applications such as in biotechnology, nuclear waste solidification, and encapsulation, and composite with fillers and reinforcements. They are biocompatible, non-toxic and can easily form bonds with tissues in the human body. With their high biocompatibility and good surface properties, synthetic phosphates materials have promissory application in biomedicine. PO_4^{3-} group has the ability to bond with other structural units. This makes them appropriate as hosts to accommodate rare earth activator ions. Different phosphates powders such as barium, calcium and strontium phosphates co-doped with Er^{3+}/Yb^{3+} and Eu^{3+}/Yb^{3+} were successfully synthesized by urea combustion method. Er^{3+} and Eu^{3+} usually replace the alkaline (Ba^{2+}, Ca^{2+} and Sr^{2+}) in the host. Er^{3+} ions in host lattice emit blue ($^2H_{9/2}\rightarrow{}^4I_{15/20}$), green ($^2H_{11/2}$, $^4S_{3/2}\rightarrow{}^4I_{15/2}$), and red ($^4F_{9/2}\rightarrow{}^4I_{15/2}$) light as an activator under infrared radiation. Eu^{3+} emit in the red ($^5D_0\rightarrow{}^7F_j$) region. Yb^{3+} ion act as a sensitizer to enhance the intensity of the up-converted emission. The enhancement of red emission makes phosphate based phosphors suitable for applications in photodynamic therapy, as the red emission is used to activate most of photosensitizers during the treatment. Photodynamic therapy (PDT) is an emerging alternative cancer treatment to radiation therapy. The advantage of PDT over other treatments

is the selectivity of drug accumulation in cancer cells, the ability to focus the light in the tumour cells which minimizes damage to healthy cells. PDT activity is dependent on photosensitizers and appropriate laser excitation source wavelength in the presence of ground state molecular oxygen.

10.2 Experimental

10.2.1 Cell culture studies

10.2.1.1 In vitro dark viability studies

The human breast adenocarcinoma (MCF-7) cells were cultured using a Dulbecco's modified Eagle's medium (DMEM) containing 4.5 g/L glucose with L-glutamine and phenol red, supplemented with 10% (v/v) heat-inactivated fetal calf serum (FCS), and 100 unit/mL penicillin-100 µg/mL streptomycin-amphotericin B. The cells were grown in 75 cm^2 vented flasks (Porvair) and incubated at 37 ^oC and 5% CO_2 with humidified atmosphere and routinely subcultured by standard trypsinisation.

Once 100% cell confluence was achieved, viable trypsinised cells were counted via trypan blue dye exclusion assay (0.4 % trypan blue solution) using a hemocytometer.

The following formula was used to estimate a total number of cells.

Total number of cells = (Mean Cell Count per grid) (Dilution Factor) (Grid Area) (Dilution Volume)

= (86.75) (4) (10000) (3)

= 10 920 000 cells

The cells were seeded at a cell density of 10000 cells/well in supplemented DMEM containing phenol red in 96-well tissue culture plates. The cells were incubated at 37 ^oC and

5% CO_2 for 24 h to foster cell attachment to the wells. The attached cells were rinsed with 100 µL DPBS once, followed by administration of 100 µL supplemented DMEM containing (5, 10, 20, 30 and 40) µg/mL of phosphate based nanoparticles (NPs). The stock concentrations were prepared by dissolving them in water and making the volume up with supplemented DMEM. Control cells were incubated in supplemented DMEM only.

The 96-well plates containing cells and the powders were incubated at 37 ^{o}C and 5% CO_2 in the dark for 24 h. After 24 h, the wells were rinsed with 100 µL DPBS, supplemented DMEM with phenol red was added and the plates were re-incubated for 24 h. After 24 h re-incubation with supplemented DMEM with phenol red, cell proliferation neutral reagent (WST-1 assay) was used to quantify the surviving cells. The WST-1 assay was used to assess the toxicity.

10.2.1.2. Photodynamic therapy activity

Photodynamic therapy activities were assessed by incubation of attached seeded cells. Different concentration of phosphate phosphors NPs were administered in a 96-well plate containing 10 000 cells/well in a supplemented culture DMEM. Plates were incubated at 37 ^{o}C in 5% CO_2 in the dark or 24 h, and rinsed with 100 µL PBS once and the media was replaced with supplemented DMEM without phenol red. The cells containing the NPs were illuminated with light doses of 260 J/cm^2. Light from 690 nm modulight laser set up was used. After illumination, the media was replaced with supplemented DMEM with phenol red. Cell survival was expressed as percentage of placebo cells. Surviving cells were quantified after re-incubation with cultured DMEM with the use of WST-1 assay after 24 h.

10.3 Results and Discussion

Figure 10.1 shows the microscopic images of the cell morphology in the absence of drug (control) and in the presence of (A)-$Ba_5(PO_4)_3OH:Er^{3+},Yb^{3+}$, (B)-$Ba_5(PO_4)_3OH:Eu_{3+},Yb_{3+}$,

(C)-$Sr_5(PO_4)_3OH:Er^{3+},Yb^{3+}$, (D)-$Ca_5(PO_4)_3OH:Er^{3+},Yb^{3+}$, (E)-$Sr_5(PO_4)_3OH:Eu^{3+},Yb^{3+}$ and (F)-$Ca_5(PO_4)_3OH:Eu^{3+},Yb^{3+}$ at different concentrations (5 and 40 µm/L) of nanoparticles. The NPs showed no cytotoxicity activities against the MCF-7 cell line. Figure 10.2 shows the *In vitro* dark cytotoxicity of $Ba_5(PO_4)_3OH$ and $Ba_5(PO_4)_3OH$:Eu complexes. The percentage of cell viability decreases with increasing concentrations of the complexes as shown in table 10.1.

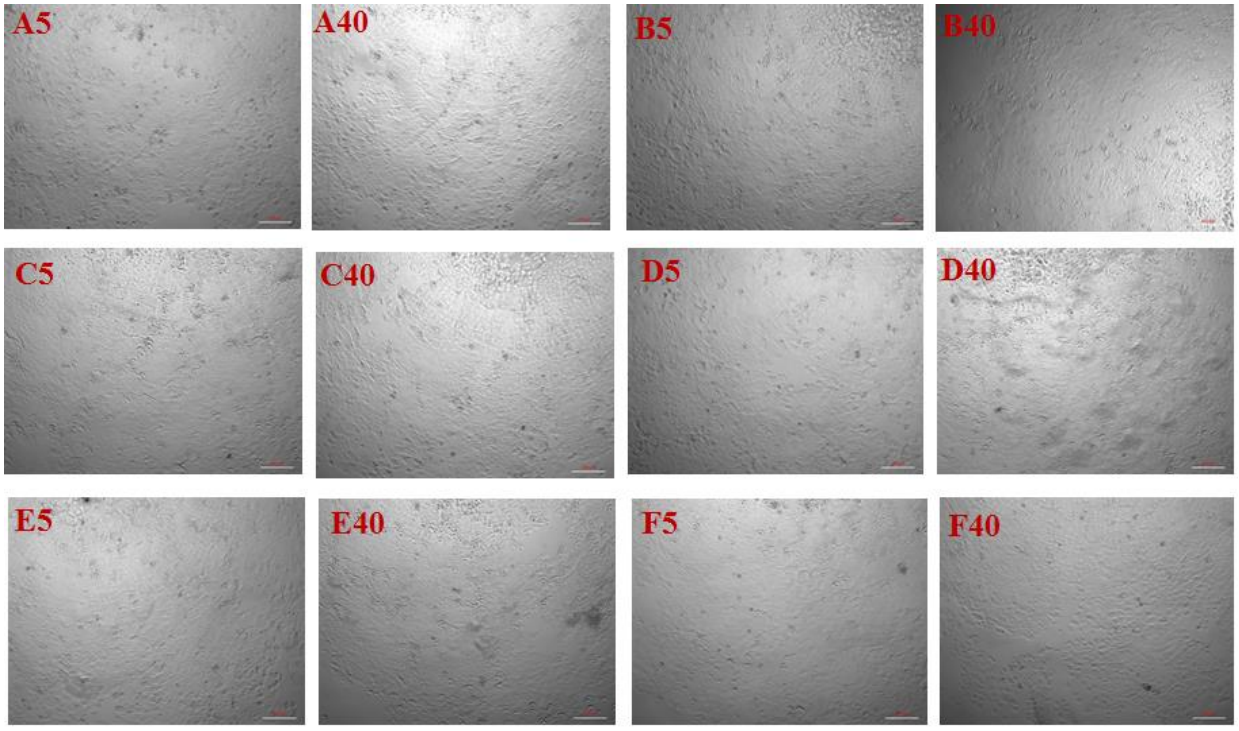

Figure 10.1 Cytotoxicity for MCF-7 cells lines at 200µm magnification: control cells and different concentrations (5 and 40 µg/L) of nanoparticles.

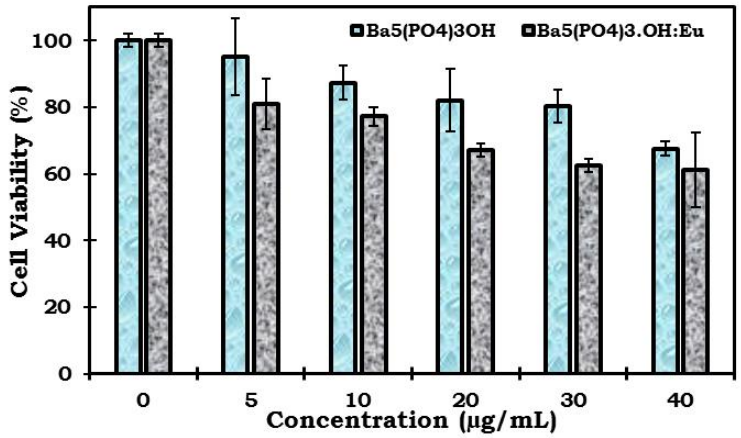

Figure 10.2 In vitro dark cytotoxicity of $Ba_5(PO_4)_3OH$ and $Ba_5(PO_4)_3OH:Eu^{3+}$ complexes against MCF – 7 cells.

Table 10.1. Dark cytotoxicity of $Ba_5(PO_4)_3OH$ and $Ba_5(PO_4)_3OH$:Eu complexes

Complexes	Percent Cell Viability (%)				
	5 (µg/mL)	10 (µg/mL)	20 (µg/mL)	30 (µg/mL)	40 (µg/mL)
$Ba_5(PO_4)_3OH$	95 ± 12	87 ± 5	82 ± 9	80 ± 5	68 ± 2
$Ba_5(PO_4)_3OH$:Eu	81 ± 8	77 ± 3	67 ± 2	63 ± 2	61 ± 11

The percentage cell viability data of the NPs in the absence (Dark Cytotoxicity) and presence of light (PDT) cytotoxicity is shown in Table 10.2. As the concentration of the NPs

increased corresponding decrease in the number of viable cells were observed. This trend was observed in the absence and presence of light. All the NPs showed cell viability greater than 50% but no significant PDT activity was observed. The PDT activity data was found to be relatively different in terms of numbers of viable cells as less % cell viability was observed except in some cases where increase % cell viability in comparison to dark cytotoxicity data.

Table 10.2. Dark cytotoxicity and PDT data.

		5 (µg/L) (%)	10 (µg/L) (%)	20 (µg/L) (%)	30 (µg/L) (%)	40 (µg/L) (%)
$Ba_5(PO_4)_3OH:Er^{3+},Yb^{3+}$ (A)	Dark cytotoxicity	**99±10**	**97±9**	**93±7**	**92±9**	**90±9**
	260 J/cm^2	**94±11**	**89±9**	**85±5**	**82±5**	**78±5**
$Ba_5(PO_4)_3OH:Eu^{3+},Yb^{3+}$ (B)	Dark cytotoxicity	**95±16**	**94±8**	**91±13**	**89±12**	**85±15**
	260 J/cm^2	**84±7**	**78±8**	**75±5**	**71±8**	**67±7**
$Sr_5(PO_4)_3OH:Er^{3+},Yb^{3+}$ (C)	Dark cytotoxicity	**72±19**	**72±13**	**69±12**	**65±11**	**61±7**
	260 J/cm^2	**86±14**	**85±8**	**83±6**	**81±6**	**80±6**
$Ca_5(PO_4)_3OH:Er^{3+},Yb^{3+}$ (D)	Dark cytotoxicity	**66±7**	**64±7**	**61±6**	**59±2**	**59±6**
	260 J/cm^2	**98±5**	**95±6**	**93±3**	**91±3**	**89±4**
$Sr_5(PO_4)_3OH:Eu^{3+},Yb^{3+}$ (E)	Dark cytotoxicity	**61±6**	**62±5**	**62±6**	**64±9**	**64±8**
	260 J/cm^2	**90±0**	**89±2**	**88±4**	**88±3**	**87±4**
$Ca_5(PO_4)_3OH:Eu^{3+},Yb^{3+}$ (F)	Dark cytotoxicity	**66±4**	**63±7**	**60±7**	**59±8**	**57±5**
	260 J/cm^2	**91±7**	**90±4**	**89±4**	**87±4**	**85±2**

The ± values indicates standard error of the mean of each data presented in percentage

10.4 Conclusion

We can conclude that the phosphate based upconversion nanoparticles showed no dark cytotoxicity and significant PDT activity when administered independently. In addition, efforts will be made to re–evaluate the PDT activity of some of the materials as inconsistent results in comparison to the dark cytotoxicity were observed. The absence of dark

cytotoxicity and PDT activity of the materials could serve as good indication when they are concurrently administered with suitable photosensitizers.

Chapter 11

Summary and future work

11.1 Summary

This thesis reported on the preparation of $Ba_5(PO_4)_3OH:Er^{3+},Yb^{3+}$, $Ba_5(PO_4)_3OH:Eu^{3+},Yb^{3+}$, $Ca_5(PO_4)_3OH:Er^{3+},Yb^{3+}$, $Ca_5(PO_4)_3OH:Eu^{3+},Yb^{3+}$, $Sr_5(PO_4)_3OH:Er^{3+},Yb^{3+}$ and $Sr_5(PO_4)_3OH:Eu^{3+},Yb^{3+}$ powder phosphors prepared with different concentrations of Er^{3+}, Eu^{3+} and Yb^{3+} by the urea combustion method. Structure, particle morphology and luminescent properties of all the phosphor powders mentioned above were investigated. The Bruker AXS D8 X-ray Diffraction was used to analyse the structure of the samples. All the powder phosphors exhibited hexagonal phase, the narrow and sharp peaks indicate a highly crystalline structure for the powders. The crystallite sizes of the powders were 27 nm for as-prepared powders and in the range of 39 - 44 nm for annealed powders. There were impurities in XRD spectra of $Ca_5(PO_4)_3OH:Er^{3+},Yb^{3+}$ and $Ca_5(PO_4)_3OH:Eu^{3+},Yb^{3+}$ system, which were assigned to $Ca_2P_2O_7$ and CaO peaks.

Particle morphology was examined using a JEOL JSM-7800F thermal field emission scanning electron microscope coupled with an Oxford Aztec 350 X-Max80 Energy x-ray Dispersive Spectroscopy which was used to analyse the chemical composition of the phosphors under typical vacuum of 9.634×10^{-5} Pa. The particle morphology of the powders varied from ellipsoidal shape formed by small particles, to rods or needle-like, plate-like with small agglomerated particles encrusted on the surface of bigger particles, agglomerated particles forming hexagonal shape, and network of particles with irregular shapes for $Ba_5(PO_4)_3OH:Er^{3+},Yb^{3+}$, $Ba_5(PO_4)_3OH:Eu^{3+},Yb^{3+}$, $Ca_5(PO_4)_3OH:Er^{3+},Yb^{3+}$, $Ca_5(PO_4)_3OH:Eu^{3+},Yb^{3+}$, $Sr_5(PO_4)_3OH:Er^{3+},Yb^{3+}$ and $Sr_5(PO_4)_3OH:Eu^{3+},Yb^{3+}$ powder phosphors, respectively. Almost all the powders had porous structures resulting from the inherent nature of the combustion reaction associated with the evolution of large volume of gases and short reaction period. The EDS spectrums were observed confirming the formation of all phosphor powders.

The absorption and bandgap energies were evaluated using a Perkin Elmer Lambda 950 UV-Vis spectrometer. The photoluminescence data were recorded using Cary eclipse fluorescence with monochromatized xenon lamp and upconversion emissions were measured by using Edinburgh Instruments FLS980 Fluorescence Spectrometer with 980 nm NIR laser as the excitation source and photomultiplier (PMT) detector. Upconversion photoluminescence emission was measured by using a photoluminescence system consisting of a fibre-coupled 980 nm NIR (near infrared) laser as the excitation source, iHR320 Horiba Yvon imaging spectrometer, R943 -02 Hamamatsu Photonics photomultiplier (PMT) detector and a SR830 Standford Research System lock-in amplifier.

The up-conversion (UC) PL emission spectra's of $Ba_5(PO_4)_3OH:Er^{3+}$, $Ca_5(PO_4)_3OH:Er^{3+}$ and $Sr_5(PO_4)_3OH:Er^{3+}$ phosphor powders were recorded at room temperature when the powder was pumped using the 980 nm laser. The samples exhibited multiple emission peaks at in the green region and another peaks in the red region that of Er^{3+} ion. Upon addition of Yb^{3+} in the $Ba_5(PO_4)_3OH:Er^{3+}$ and $Sr_5(PO_4)_3OH:Er^{3+}$ systems, red emission peaks are enhanced due to an energy transfer process between Er^{3+} and Yb^{3+}. Upon addition of Yb^{3+} in the $Ca_5(PO_4)_3OH:Er^{3+}$ system, the green emission is enhanced faster than the red emission. The enhancement of green emission can be due to the increasing of the three-photon energy transfer process probability between Yb^{3+} and Er^{3+} ions.

The PL excitation and emission of $Ba_5(PO_4)_3OH:Eu^{3+}$, $Ca_5(PO_4)_3OH:Eu^{3+}$ and $Sr_5(PO_4)_3OH:Eu^{3+}$ phosphors were measured using Cary eclipse fluorescence with monochromatized xenon lamp. The excitation peaks are observed at different wavelengths ranging from 240-537 nm. The broad intense excitation peak at 240 nm is attributed to O^{2-}-Eu^{3+} charge transfer band. The other excitation peaks located at ~319, 360, 382, 395 and 465-537 nm. The emission peaks are observed at ~589, 614, 651 and 699 nm of Eu^{3+} ion. Upon co-doping with Yb^{3+}, the upconversion emission is observed. This indicates that the Eu^{3+} ions are excited due to the presence of Yb^{3+} ions. The emission peaks observed at ~523, 588, 613, 657 and 704 nm are attributed to Eu^{3+} ion in the $Ba_5(PO_4)_3OH:Eu^{3+},Yb^{3+}$ system. The strongest emission peak is observed at 657 nm assigned to Eu^{3+} ion for $Ba_5(PO_4)_3OH:Eu^{3+}$ and $Sr_5(PO_4)_3OH:Eu^{3+}$ systems. The prominent red emission from Eu^{3+} ion is clearly observed at 613 nm for $Ca_5(PO_4)_3OH:Eu^{3+}$ system. This is due to energy transfer upconversion from Yb^{3+} to Eu^{3+}. Yb^{3+} act as a sensitizer for Eu^{3+} via cooperative energy transfer process.

By comparing the red luminescence for all the prepared phosphors, the PL results shows that all the phosphors emit efficient red luminescence that can be used for PDT activity. It is only $Ca_5(PO_4)_3OH:Er^{3+},Yb^{3+}$ phosphor that give intense green emission, but it can also be used to activate other types of photosensitizers that absorbs green light. From the toxicity measurements, the result shows that the phosphors are non-toxic. The red luminescence can be used to activate a number of photosensitizers in photodynamic therapy treatment.

11.2 Future work

Further research is to test the phosphate phosphors prepared in photodynamic therapy treatment, by using an appropriate laser (excitation of 980 nm). Check the efficiency of the prepared and improve the photoluminescence of the phosphors. There are other rare earth ions showing upconversion luminescence such as Yb^{3+} co-doped with Ho^{3+}, Tm^{3+} and Tb^{3+}. They also exhibit strong luminescence when excited with in the NIR range (975-978 nm). The other phosphate phosphors can also be prepared with the above mentioned rare earth ions to compare the efficiency of the red luminescence.

11.3 International Conferences

- **3rd World Congress and Expo on Nanotechnology, 07-09 November 2016, Singapore**

  Upconversion nanoparticles for photodynamic therapy.

  P.P. Mokoena, O.M. Ntwaeaborwa, H.C. Swart

- **7th South African Conference on Photonic Materials, 27-31 March 2017, Amanzi Private Game Reserve, South Africa**

  Upconversion luminescence of Er^{3+}/Yb^{3+} doped $Sr_5(PO_4)_3OH$ phosphor powders for photodynamic therapy.

  P.P. Mokoena, H.C. Swart, O.M. Ntwaeaborwa

11.5 National Conferences

- **61st Annual Conference of the South African Institute of Physics, 4-8 July 2016, Cape Town, South Africa**

Combustion synthesis and characterization of Eu^{3+} doped $Ba_5(PO_4)_3OH$ phosphors

P.P. Mokoena, H.C. Swart, O.M. Ntwaeaborwa

11.6 Publication

- **P.P. Mokoena, H.C. Swart, O.M. Ntwaeaborwa, Physica B: Condensed Matter, In press, corrected proof, Available online 15 June 2017**

11.7 Biography

Puseletso Pricilla Mokoena was born and raised in small village by the name of Namoha, Qwaqwa in the Eastern Free State. She joined the University of the Free State (Qwaqwa campus) in 2007 and obtained her bachelor B.Sc degree in 2011. In 2011, she enrolled for B.Sc Honours (in Physics) and was also appointed as a student assistant. She joined the University of the Free State (Bloemfontein campus) in 2012 to do Masters and her project title was "*narrowband UVB emission from gadolinium and praseodymium co-activated calcium phosphate phosphors for phototherapy lamps*" and she passed it with Cum Laude. She was appointed as Research Assistant at the Centre for Microscopy in 2014. She started her Ph.D degree in 2014, working on "*upconversion of infrared to visible light in rare earth doped phosphate phosphors for photodynamic therapy applications*". The aim of the project was to enhance the red luminescence of the phosphors used to activate the photosensitizers that kills the cancerous cells. During the period of her study, she was offered the opportunity to attend and give talks at national and international conferences and laboratories. Her first international travel, she went to Dubna, Russia in 2012 for participation in student practice in joint institute for nuclear research (JINR) of research. She also went to Rhodes University for TL measurements at physics department and PDT activity at chemistry department. She attended international conference "3rd World Congress and Expo on Nanotechnology" in 2016 at Singapore. She

also attended national conference "61st Annual Conference of the South African Institute of Physics", held in Cape Town, South Africa, 2016.